The Incorporation of Particles Suspended in the Electrolyte into Plasma Electrolytic Oxidation Coatings

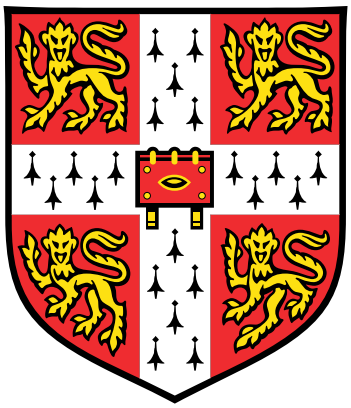

Matthew O'Hara

Department of Materials Science and Metallurgy

University of Cambridge

This thesis is submitted for the degree of

Doctor of Philosophy

Downing College July 2021

I don’t like it, and I’m sorry I ever had anything to do with it.

—Erwin Shrödinger

Declaration

This thesis is submitted for the degree of Doctor of Philosophy at the University of Cambridge. The research described herein was carried out by myself in the period from October 2016 to March 2020, under the supervision of Professor T.W. Clyne, in the Department of Materials Science and Metallurgy at the University of Cambridge.

I hereby declare that, except where specific reference is made to the work of others, the contents of this dissertation are original. No part of this dissertation, or any similar to it, has been, or is currently being submitted for consideration for any other degree or qualification at any other University or similar institution. This dissertation is the result of my own work and includes nothing which is the outcome of work done in collaboration except where specifically indicated in the text and Acknowledgements. It is fewer than 60,000 words in length.

Matthew O'Hara

July 2021

Acknowledgements

I would particularly like to thank my supervisor, Professor Bill Clyne, for his invaluable support, guidance, and advice throughout this project, and, of course, for all the summer BBQs and punt trips. Elsewhere in the department there have been a number of people without whom this project would have been impossible, particularly Kevin Roberts and Sue Gymer in the Process Lab, Bob Stearn in the Gordon Lab, and all the workshop personnel. Additionally, I would like to thank Dr Sam Troughton and Dr Robin Francis of Keronite for many helpful technical discussions.

I really don't know how to even start thanking the countless people that have helped get me through this PhD, but I think Dr. Jimmy Campbell would throw a hissy fit if he wasn't in the first sentence. I have had a great team with me at the Gordon Lab, who have helped me every time I asked for it, and I really am forever grateful. Dr. Burley and Julia for making sure I had my recommended weekly allowance of Spoons, Steed Mal-Brug for being there to fact-check my lunchtime chat, Maxim 'KDB' Vreeswijk (I think is how it's spelt) for trying his best to keep Liverpool from winning the prem, Dr. Meg for keeping Campbell in check, and Dr. Alastair Houston for generally being great.

My family know more than most that the road to where I am now has not been the easiest, and I am indebted permanently to them for their unconditional love and support. I could not

have got this far without them. Ryan and Meghan, you have contributed more than you know to this thesis.

Abstract

This work describes an investigation into the mechanisms responsible for the incorporation of particles and fibres suspended in the electrolyte during plasma electrolytic oxidation, and provides a comparison of the processing and discharge characteristics of aluminium, titanium and magnesium.

Well-established methods such as synchronised small area and high speed video monitoring, which have previously been successfully applied to the study individual discharge characteristics of aluminium, are extended to magnesium and titanium substrates. It was found that while magnesium behaves quite similarly to aluminium, titanium discharges are by contrast much less energetic, due to much lower discharge currents and durations. These observations are attributed to differences in the properties of each metal oxide.

Particle incorporation into coatings on Al and Ti substrates was studied using three types of oxide powder; 30 μm alumina, 7 μm magnesia and 100 nm alumina. It has been established that, where such reactions are chemically favoured, phase changes can occur that must have involved the particulate reaching very high temperatures. From this and other evidence, it is concluded that the main incorporation mechanism involved is that of (fine) particulate being swept into the pores associated with active discharge sites, while they are being refilled with electrolyte immediately after collapse of the plasma. They are then likely

to become entrapped, and in many cases to be strongly heated as the plasma is created during the next discharge cycle.

Alumina (Saffil®) fibres were successfully incorporated into PEO coatings on Ti and Al substrates and it is concluded that incorporation is due to the the trapping (and subsequent partial or full melting) of fibres in and around discharge pores. Fibre incorporation is observed to be more homogeneous, on Ti substrates, in cases where the (fibre-containing) electrolyte is jetted across the face of the sample.

Table of contents

Nomenclature

Roman Symbols

C	Particle Concentration
D	Representative Pore Diameter
d	Particle Diameter
E	Electric Field Strength
F	Resultant Force
H	Coating Thickness
h	Thickness of consumed metal substrate
I	Current
L	Representative Pore Depth
M	Atomic mass
m	Sample mass
p	Porosity Level
q	Net Particle Charge

R Charge Ratio

u Velocity

V Volume of Electrolyte

Greek Symbols

Δ Change

η Dynamic Viscosity

ρ Density

ζ Zeta Potential

Subscripts

dis Discharge

met Metal

ox Oxide

p Particle

ter Terminal

Acronyms / Abbreviations

AC Alternating Current

BSE Back-Scattered Electron

CP Commercially Pure

DC Direct Current

EDX Energy Dispersive X-Ray Spectroscopy

HA Hydroxyapatite

MAO Micro Arc Oxidation

PEO Plasma Electrolytic Oxidation

PMT Photomultiplier Tube

$PTFE$ Polytetrafluoroethylene

RMS Root Mean Square

SEM Scanning Electron Microscopy

TEM Transmission Electron Microscopy

XRD X-Ray Diffraction

Chapter 1

Introduction

Plasma Electrolytic Oxidation (PEO) is a surface treatment applied to a range of metals including aluminium, magnesium and titanium. It results in thick, strongly adherent oxide coatings which drastically improve the wear and corrosion resistance of these structural metals. This makes it possible to manufacture lighter componentry, as heavier materials such as steel can be replaced with PEO coated light metals. The process is similar to anodising, but the applied potentials and current densities are used, causing visible sparking across the metal surface; a defining characteristic of PEO. These sparks are the result of local dielectric breakdown of the native oxide layer and growth of a plasma discharge incorporating ions from the substrate and electrolyte, which ultimately collapses to form new coating material. PEO is sometimes referred to as Micro Arc Oxidation (MAO), spark anodising, anodic spark deposition or microplasma oxidation, but the term plasma electrolytic oxidation has become the norm and will be used in this thesis.

PEO is now a well-established industrial process, with multiple companies specialising in the process across the globe. Despite this industrial interest, the underlying mechanisms of PEO are still poorly understood, and the development of new coatings are typically based on

empirical evidence and first-hand observations. Recent academic work describing the events surrounding an individual discharge has, however, provided an insight into how coating formation progresses, and why certain metals are more suited to PEO processing than others. This knowledge can potentially lead to greater control of the process and, by extension, coating properties.

The incorporation of particles suspended in the electrolyte into PEO coatings has been described in the literature as a novel method of controlling coating microstructure, although again the majority of these studies have been empirical or 'trial and error' in nature. As of yet, there is little in the way of a mechanistic understanding of how particle incorporation fits in with well-established coating formation models.

1.1 Applications

The PEO process has been used increasingly in recent years to coat parts used in a wide range of industries, in part due to the large volume of research performed into the properties of the coating. In the automotive and aerospace industries, PEO has been used to produce higher performing, lighter components by replacing heavier metals such as steel with PEO coated light metals (mainly, but not exclusively Al, Mg and Ti - see §2.4.1). This is possible in part due to the high hardness and compliance, resulting in excellent wear resistance [1–5]. The wear performance of such coatings has led to their use in high-end bicycle rim braking surfaces, as well as in the consumer electronics market for use as protective treatment for outer casings. Others, such as the oil and gas industry, exploit the excellent corrosion-resistant properties of such coatings [6–8] for applications in highly corrosive environments. As the coating is highly porous, this corrosion resistance can be improved further with the application of a sealant, which can freely penetrate through the interconnected porosity.

Titanium and to an extent magnesium have found use in the medical industry, as joint replacements and cardiovascular stents among others, due to their inherent biocompatibility, and the porous nature of the coating has been shown to promote cellular ingrowth, promoting more successful integration of the implant into the body [9–11]. Recently, it has been shown that TiO_2 can be used as a photocatalyst [12] for the treatment of contaminated water, and PEO processing has been suggested as a method for producing the oxide, as the interconnected porosity [13] can drastically increase the surface area for reaction.

Particle incorporation into PEO coatings shows promise of improving these properties even further, even if the work done is mostly empirical in nature. For example, PTFE has been successfully incorporated into a PEO coating, leading to a reduced friction coefficient (from ≈ 0.8 with respect to itself to ≈ 0.3) [4, 14]. Particle incorporation into PEO coatings has been applied to medical alloys, for example hydroxyapatite (HA) has been incorporated into Ti and Mg based coatings to improve biocompatibilty, and reduce leaching of metal ions into the body [15–18]. There is scope for particle incorporation in photocatalytic applications; doping the coating with cerium was shown to increase the absorption of light and thus increase rates of reaction [19, 20]. The specific surface area available for reaction could in theory be increased via surface modification with the incorporation of high aspect ratio fibres.

Despite these advances, there is still work to be done in elucidating the underlying mechanisms of particle and fibre incorporation, and how these will fit with the well-established models of coating formation.

1.2 Thesis Structure

The PEO process is quite complex, and concerns aspects of electrochemistry, plasma physics, fluid dynamics and thermodynamics. Because of this complexity, for many years most

research into the process was rather crude and empirical, however in recent years there has been much high-quality work aimed at elucidating the underlying mechanisms by which a PEO coating is generated. These recent developments, along with a brief historical context, will be discussed in **Chapter 2**.

Chapter 3 reviews the latest research conducted on PEO processing with particle additions. This is mostly empirical work, describing the effects of adding various particles and discusses inert and active incorporation. The weaknesses of some currently proposed mechanisms of incorporation are discussed.

Chapter 4 describes the experimental procedures used in the current work. This includes the PEO processing equipment itself, the small area current monitoring method, Scanning Electron Microscopy (SEM) use, X-Ray Diffraction (XRD) use, and the methods used to characterise particle size.

Chapter 5 provides a systematic comparison of the most commonly processed substrates; aluminium magnesium and titanium. The electrical response, growth rate, energy consumption and discharge characteristics are investigated for the three main substrates and their behaviour is attributed to known properties of the respective substrates and oxides.

Chapter 6 proposes a mechanism of incorporation of particles suspended in the electrolyte, based on measured mass changes with and without particle inclusion, EDX and XRD study and microscopy. It is shown that a major proportion of particle uptake is due to particles being swept into pores as it refills with electrolyte after a discharge, and a calculation provided which appears to refute the theory that particle incorporation is mainly due to electrophoresis.

Chapter 7 discusses the incorporation mechanism of relatively high aspect ratio (≈ 10) alumina fibres into PEO coatings.

Chapter 8 is the concluding chapter, and draws together the findings of this work.

Chapter 2

The Plasma Electrolytic Oxidation Process

There has been a considerable amount of progress towards reaching a more complete understanding of the PEO process in recent years. This chapter will discuss the historical context of the process, characteristic coating properties, and finally the recent work on individual discharge characteristics, which has significantly progressed the understanding why certain metals are so suitable for PEO, and the underlying mechanisms of coating formation.

2.1 Historical Development

PEO was developed from anodising, which is an electrochemical process where an oxide film is grown on a metallic substrate (most notably Al, Mg and Ti) by passing a DC current through a workpiece immersed in conductive (typically acidic) electrolyte. The resultant coating is relatively thin, characterised by columnar growth and nano-scale pores, usually

with an amorphous atomic structure [21]. The voltage required by various solutions may range from 1 to 300 V DC, although most fall in the range of 15 to 21 V. The anodising current varies with the area of substrate being anodised and typically ranges from 0.3 to 3 A dm^{-2}. PEO processing differs in that higher (typically AC) voltages in the range $\approx$ 250 - 750 V are employed such that the dielectric breakdown potential of the substrate oxide is exceeded. This results in the characteristic sparks which appear across the surface of the workpiece known as discharges. The resultant oxide is not formed due to an electrochemical process, but is formed as oxygen and substrate ions combine in these short-lived plasma events and cool to form thick (up to $\approx$ 500 μm), crystalline coatings, with superior wear resistant properties to their anodised counterparts.

2.2 Practical PEO Processing

A major benefit of PEO processing is the ability to easily vary certain parameters including but not limited to power supply and electrolyte composition to tailor coating properties for targeted applications. Variable properties include morphology, phase constitution, and even aesthetic properties such as colour and texture. This flexibility and the widening range of possible applications outlined in §1.1 has meant that industrial usage of the PEO process continues to increase. due to the widening range of possible applications outlined in §1.1. At the time of writing, a number of major companies produce PEO coatings: Keronite (United Kingdom/USA), Surface Modification Systems (USA) Tagnite (USA) Henkel (Germany) AHC Oberflächentechnik (Germany). The equipment needed is not particularly complex, and a range of current waveforms can easily be generated by a simple variable capacitor or rectifier network. The electrolytes used are typically alkaline (Potassium Hydroxide is commonly used as a source of OH^- ions) and non-toxic, in contrast to the chromic acid-containing solutions used in anodising.

2.2.1 Power Supplies

The three main power modes used in commercial processing are potentiostatic, galvanostatic and constant capacitance (this refers to a processing mode whereby a fixed charge is supplied during each half of the processing cycle). Within these modes, a range of electrical waveforms have been used. Early systems used DC waveforms and tended to run in galvanostatic mode, but this led to difficulties in controlling discharge characteristics; in particular, discharges tended to become long-lived and destructive. Purely DC sources are, therefore, limited to small components with a thin coating requirement. This was rectified with the application of a pulsed DC source, which naturally limits discharge lifetime to the source time period. In the past few decades, however, the benefits of including a cathodic component in the waveform have been researched [22–25]. There is a consensus in the literature that a cathodic component tends to result in a more compact coating with lower surface roughness. The role of the cathodic component will be explored further in §2.5.3, in the context of the 'soft sparking' regime. In practice, the cathodic component is incorporated with an AC sine wave at mains frequency or a bipolar square wave. Figure 2.1 is a schematic of a typical variable square wave supply, which is able to operate in galvanostatic or potentiostatic modes.

2.2.2 Electrolyte Compositions

The composition of the electrolyte used in PEO processing can be tailored somewhat for use on different substrates, and for different applications. In most cases, the electrolyte is alkaline, with the most common additions being silicates, phosphates and aluminates. This is in contrast to the acidic electrolytes most commonly used in anodising. It is not yet understood why such a high pH is preferable for PEO processing; although it has been common for Mg alloys to be processed in an acidic fluorozirconate electrolyte under supposed

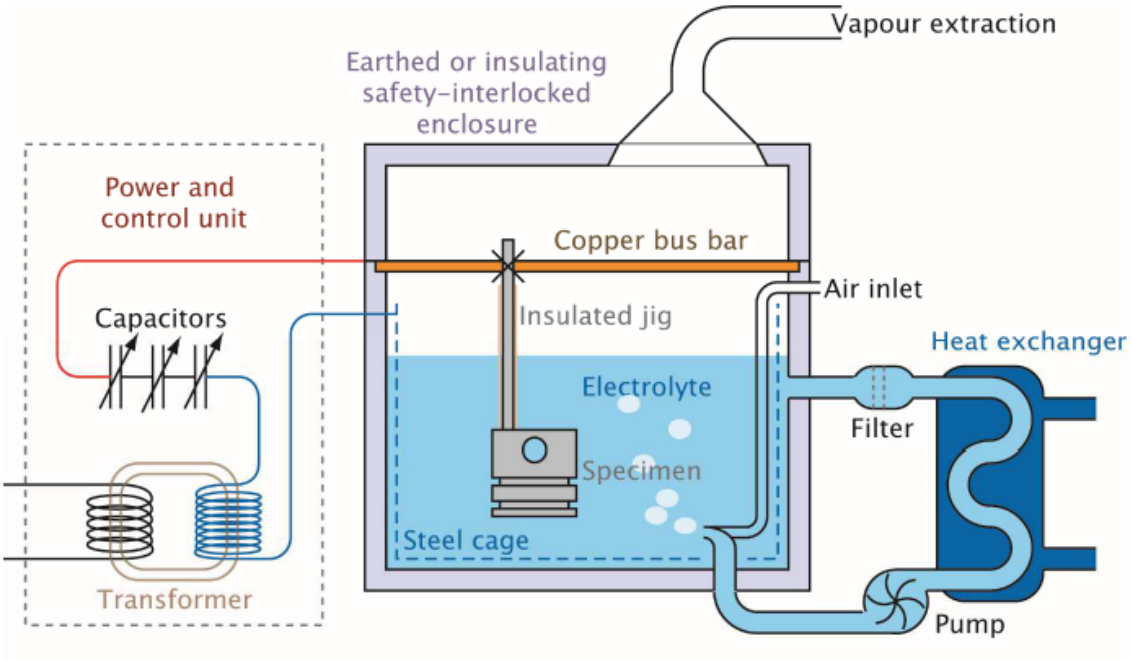

Fig. 2.1 A typical modern PEO processing rig utilising a variable capacitor network, from [26]

PEO conditions [27–30], but there is little in the way of a mechanistic understanding of the influence of pH in the process. In any case, the coatings in these cases were composed of predominantly ZrO_2, suggesting that deposition from the electrolyte was the main mechanism of coating formation rather than oxidation of the substrate via plasma discharges.

Electrolyte conductivity is usually in the range 5-100 mS cm^{-1}, and is controlled by altering the quantity of hydroxide additives; most commonly in the form of KOH or NaOH. These chemical species also increase the pH; stabilising the silicate/phosphate/aluminate additives which passivate the substrate surface against dissolution in the alkaline electrolyte [31, 32].

There has been considerable research into altering coating properties such as colour [33–38], surface roughness and texture (amongst others) by adding various chemicals to the electrolyte, however this has been particularly empirical in nature. In fact, little is known

about the influence of chemical additions dissolved in the electrolyte, other than it is common for chemical species present in the electrolyte to become incorporated into the coating. There is also evidence that substrate ions can be ejected into the electrolyte, changing the electrolyte processing characteristics [39]. There have been considerably more attempts at understanding the influence of suspending particles in the electrolyte, and indeed a review was prepared by Lu et al in 2016 [40]. This aspect of electrolyte addition will be discussed in greater detail in Chapter 3.

2.3 Coating Microstructure

2.3.1 Free Surface Morphology

The free surface of PEO coatings on Al substrates have been well characterised, and possesses features that give insight into conditions during processing. In general, Al coatings contain relatively coarse pores or discharge channels, surrounded by smooth circular "pancake" structures, which is attributed to molten oxide flow immediately after a discharge. An example of such a coating is shown in Figure 2.2. The diameter of these pancake structures have been shown to increase with processing time, reflecting the growing intensity of the discharges as the process proceeds [41].

There is less agreement as to the formation of the surface morphology of Mg and Ti coatings, in part due to the huge range of processing conditions used by different authors. Mg coatings have a broadly similar structure to those produced on Al in that the surface is covered with pores, which are the result of discharge channels [18, 42–46]. The structure of Ti coatings is quite distinct and has been described as having a semi-regular open pore structure with 'pinholes' of 100 nm diameter [47]. More detailed work by Matykina and

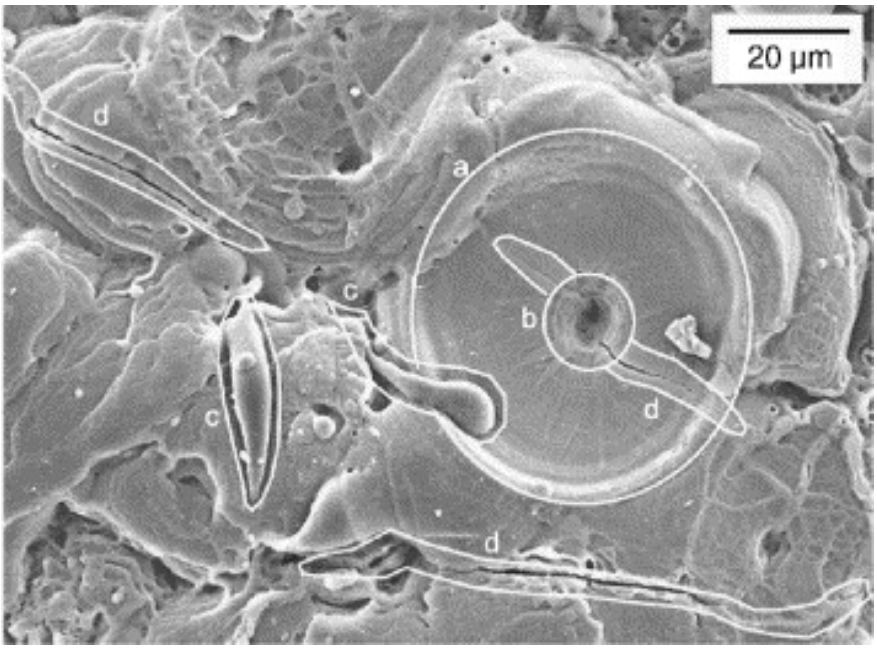

Fig. 2.2 SEM micrograph of the free surface of a 40 μm thick coating, showing typical features of a PEO coating surface. These include (a) a re-solidified pool or crater, (b) the central sink-hole ("pipe") in such a pool, (c) material ejected from such pools and (d) localised microcracking. Reproduced from [1]

co-workers [48] however, revealed that the regular pore diameter increased with processing power up to 1-2 μm. An example of a typical Ti free surface is shown in Figure 2.3. The microstructure has not been rigourously characterised, in that it is unclear whether these pores are discharge channels or the result of gas generation [49, 50]. This will be explored further in Chapter 5.

2.3.2 Internal Microstructure and Porosity

The internal microstructure of PEO coatings is generally studied using SEM and Transmission Electron Microscopy ("TEM") methods, in the form of a polished cross-section [51–53], but this method can be very subjective, due to the damage dealt to the coating during grinding and polishing procedures. It is generally accepted, however, that a two-layer structure exists; the

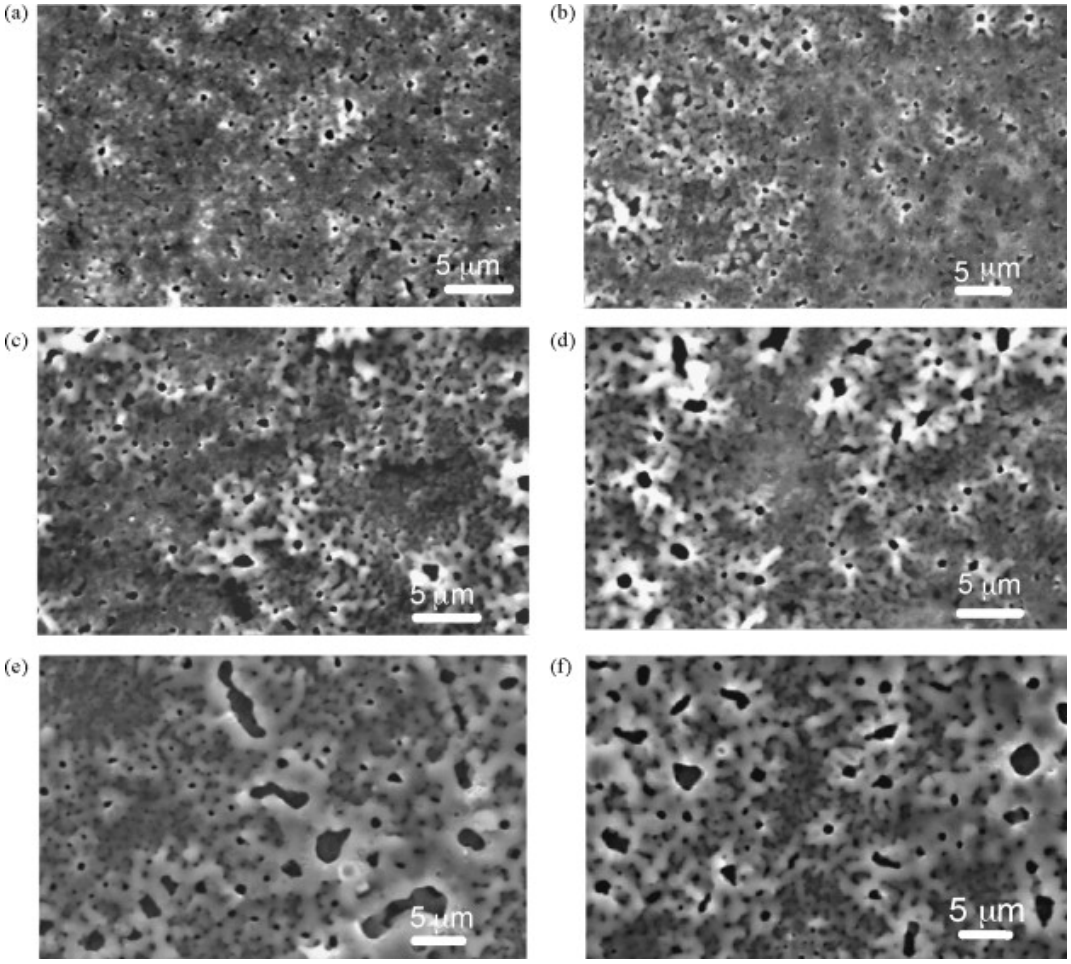

Fig. 2.3 High magnification scanning electron micrographs of Ti following PEO treatment in 0.026 M Na_3PO_4 at 20 mA cm^{-2} to (a) 300 V; (b) 330 V; (c) 350 V; (d) 370 V; (e) 400 V and (f) 430 V. Reproduced from [48].

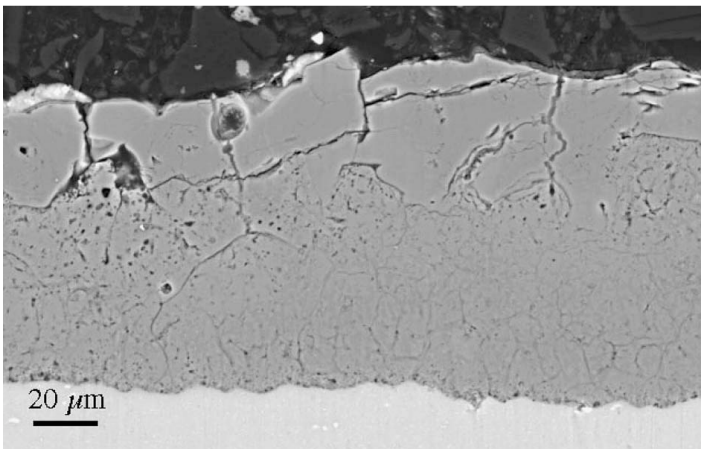

Fig. 2.4 SEM image (back-scattered electron mode) of a polished section from a PEO coating on an aluminium alloy substrate, showing the fine network of channels created by individual discharge events, apparently representing a porosity level of the order of a few per cent. Reproduced from [2]

outer described as "porous" (although porosity is often poorly reported) and the inner layer as "dense". However, using back-scattered electron (BSE) microscopy, the cross-section can be seen to be a relatively coarse network of pores and cracks (see Figure 2.4). It should be noted that PEO processing involves constant restructuring of the through-thickness coating by discharges, so the observed structure is the result of the most recent set of discharges at that area (i.e. the structure is not built up over time).

Some researchers have observed a thin ($\approx$ 100 nm) amorphous barrier layer between the substrate and coating [54, 55]. Just above this barrier, the coating material was found to be nanocrystalline, and porous on a fine, nanometre scale. This porosity was attributed to production of gases via electrochemical reactions.

The overall coating porosity is sometimes quoted as a result of using image processing of a polished cross-section, which as discussed above, is misleading due to the potential for deformation of the coating, and the possibility of filling in small pores with sheared-off coating material or even polishing media. More rigourous methods have been adopted for determining porosity including mercury intrusion porosimetry, isothermal nitrogen adsorption,

hydrostatic weighing, helium pycnometry and X-Ray Tomography [2, 53, 56]. Reported skeletal densities are very close to theoretical densities which implies that the majority of porosity is surface-connected. This means that electrolyte is present throughout the coating and can reach the interface between coating and substrate. Therefore dielectric breakdown only need happen across that thin (nm-scale) boundary layer. Mercury intrusion porosimetry performed by Curran and Clyne [2] indicate that a significant fraction of the total porosity is nm scale, with the overall porosity value ranging between 10 and 20%. This level of porosity is actually beneficial in most cases, for example, In medical applications, the high surface area certainly helps with osseo-integration, and the strain tolerance of the coatings is greatly enhanced.

2.3.3 Grain Structure and Phase Constitution

PEO coatings are constantly melted and re-solidified during processing by plasma discharges, so it is perhaps no surprise that their microstructure is so complex. Some regions will have undergone very rapid solidification, while others show evidence of effectively being 'heat-treated'(i.e. they have been allowed to cool more slowly). In general, however, most features observed in the coating are associated with faster cooling, for example a fine (sometimes amorphous) grain size and the presence of metastable phases. As is common in PEO processing, the phase (and indeed elemental) composition varies widely according to processing parameters such as electrical power regime and waveform, electrolyte composition and substrate alloying elements. On Al substrates, the most common phases are α and γ alumina, but η and ε can also be present, as well as mullite, when electrolyte with a high silicate content is used [57]. Ti coatings are usually rich in both anatase and rutile [58], but will readily form the mixed oxide Al_2TiO_5 if Al is present in either the electrolyte (in the form of aluminates) or the substrate (e.g. the most common Ti alloy, Ti-6Al-4V). Mg

coatings also commonly contain different compounds depending on the elements present in the electrolyte. For example Mg_2SiO_4 and Mg_2SiO_3 can be formed in silicate electrolytes and Mg_3PO_4 in phosphate electrolytes, in addition to its own oxide, periclase (MgO). For all substrates, at least some amorphous material is present, and the proportion of the various phases will vary according to coating depth due to differing thermal conditions.

2.4 Factors Affecting Discharge Formation

2.4.1 'Valve' Metals and Charge Transfer

The vast majority of research, and virtually all industrial interest in PEO is based on Al, Mg and Ti substrates. These metals are prime candidates for surface treatment in general as they are lightweight and lack the corrosion or wear resistance of structural steels. The reasons they are so suitable for PEO processing, however, are less clear. It has been common in the literature to describe these three main substrates as part of a group known as 'valve' metals. This group is generally accepted to be Al, Mg, Ti, Ta, Nb, Zr and Be. Apart from Al, Mg and Ti (known as the 'main' substrates for PEO processing), tantalum has shown the most promise as a candidate for PEO processing, particularly for medical implants [59–64], but there have also been accounts of coatings formed on niobium [65, 66], zirconium [28, 67, 68] and beryllium [69]. A PEO coating, composed of crystalline Fe_3O_4 and $FeAl_2O_4$ was actually obtained using a steel substrate, by Li et al [70]. The terminology around so-called 'valve' metals, however, is quite ill-defined. It is generally taken to mean the metals that form an oxide which only carries charge in one direction [71–73], in the case of PEO this means that the metal would need to be the cathode, only then could electrons easily flow from metal to oxide to electrolyte. With this rather crude definition, there seems to be a level of correlation between 'valve' metals and those most suitable for PEO. It is doubtful, however, that this set

of metals was arrived at due to in-depth knowledge of their respective oxide/metal junction behaviours.

Many metal oxides can be considered as semi-conductors (depending on their band gap, discussed further in §2.4.2) and this rectification (known as a Schottky barrier) has been exploited in various electronic devices. The sense of rectification (i.e. whether charge transfer is easier from cathode to anode or vice-versa) is dictated by the relative Fermi levels in the oxide and metal and, therefore, by the doping level in the semiconductor. The metals most successfully processed by PEO actually have quite large band gaps, above that which would typically be considered a semiconductor, so to rationalise the set of metals suitable for PEO based on any rectifying behaviour is clearly flawed, but is still cited in the literature.

The rectifying properties of the 'valve' metals has been used to account for the well-established observation that discharges (i.e. dielectric breakdown) usually (but not always - see §2.5.2) occur while the metal workpiece is the anode. A more convincing argument is based on the kinetics of ions present in the electrolyte. Figure 2.5 is a depiction of ion transport at key steps in anodising and PEO. In anodising, oxidation takes place when the workpiece is the anode, as OH^- ions are attracted through the electrolyte to the oxide-metal interface to provide a source of oxygen. During PEO, oxidation occurs not by transport of oxygen-rich ions to the surface, but by collapse and combination of substrate and oxygen ions present within a plasma discharge. PEO should, therefore, not be treated as a conventional electrochemical process as the transport of oxygen-rich species to the interface is not really relevant. Instead, the critical point is that while the metal is the anode, it is difficult for electrons from the electrolyte to travel through the oxide layer to ground. Consequently, the buildup of charge locally exceeds the dielectric breakdown strength of the oxide and a discharge occurs. In the cathodic period, electrons easily flow through the oxide to combine

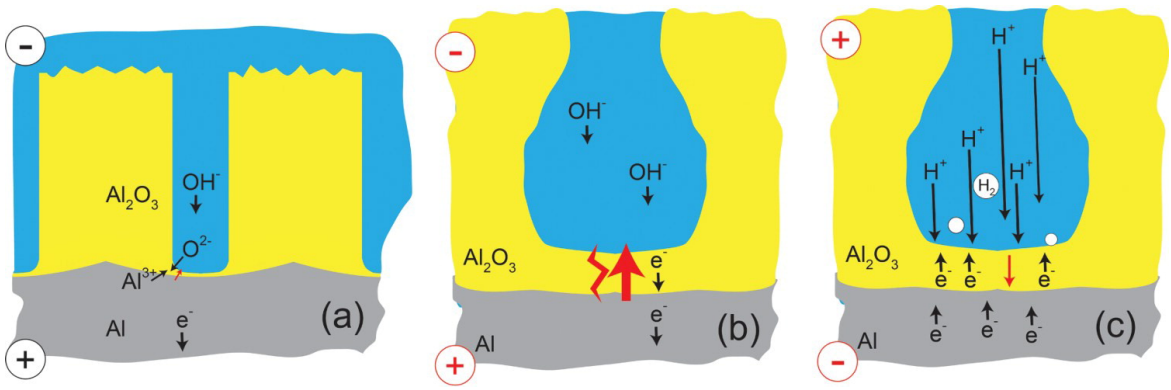

Fig. 2.5 Schematic depictions of the transport phenomena taking place during (a) anodising, (b) PEO with anodic polarity and (c) PEO with cathodic polarity. Reproduced from [74]

with H^+ ions, which, being smaller and more mobile than the OH^- ions, are transported to the interface under the applied field.

2.4.2 Oxide Band Gap

The band gap of a material refers to the energy gap between the valence and conduction bands of an electron, and by extension the energy cost associated with jumping to the conduction band. It can be said in a very broad sense, therefore, that materials with a large band gap will be less conducting than those with a small one. This quality is clearly a factor in determining whether or not a metal (or more specifically its oxide) is suitable for PEO processing. If the oxide is relatively conductive (as some oxides are), then during the anodic cycle, charge carriers in the form of OH^- ions can easily pass from the electrolyte, through the oxide and donate their electrons to the substrate. In this case, depending on the dielectric strength of the oxide (see §2.4.3), an insufficient amount of charge will have accumulated at the interface for the critical value of electric field to be exceeded for a discharge to occur.

The oxides of most ‘valve metals’ have large band gaps [75]. These were plotted against oxide stability by Clyne and Troughton [74] and is reproduced in Figure 2.6. It was found that

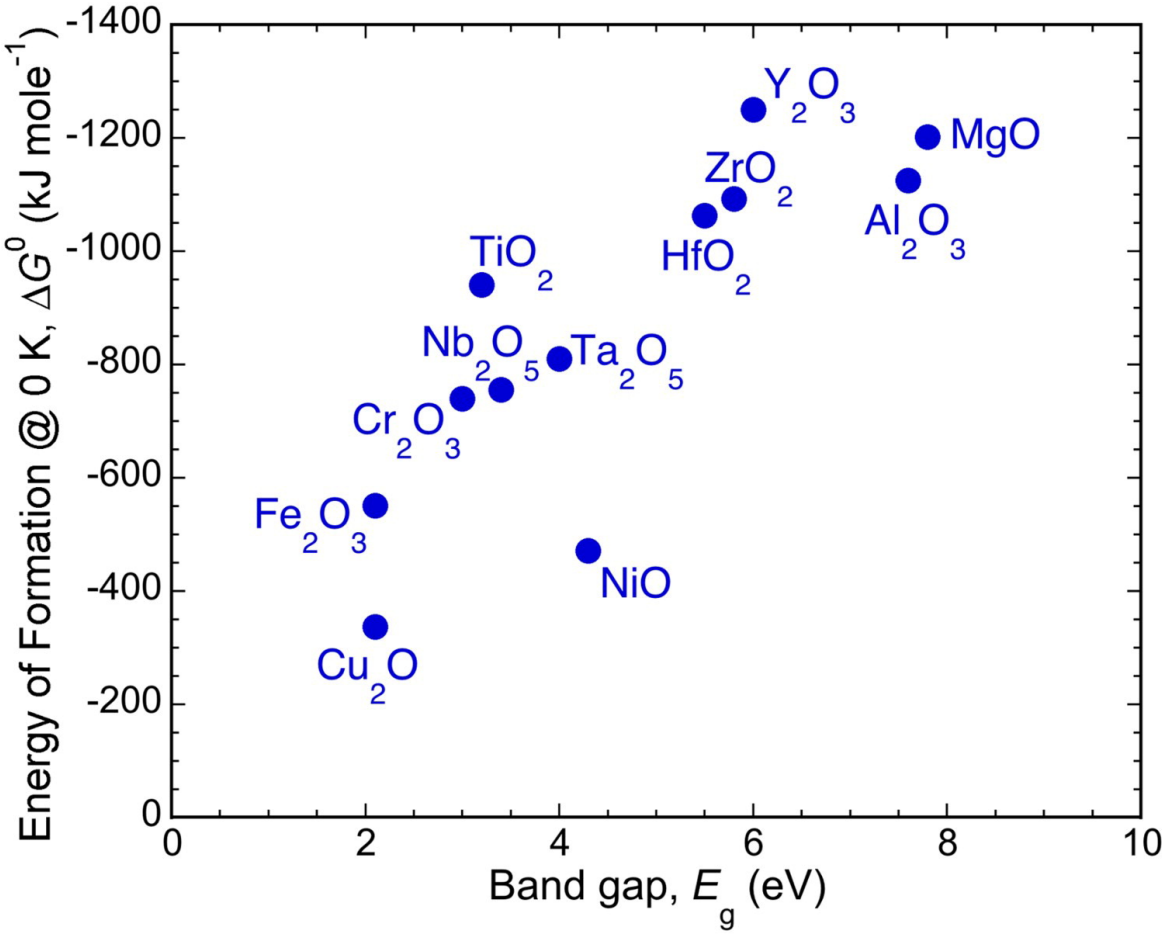

Fig. 2.6 Free energy values for the formation of various oxides from the metal, and of water from hydrogen, at 0 K. These energies are all expressed per mole of oxygen. For metals that can form more than one oxide, the data refer to the one for which the largest amount of energy is released. Reproduced from [74]

there is a correlation, albeit not a close or well-defined one. For example, the thermodynamic driving force for oxidation of Ti is similar to those of Al and Mg, but its oxide has a band gap with less than half the magnitude of those oxides.

It is important, therefore, to consider the mechanism of electron movement through the oxide and how this relates to discharge formation in PEO candidate metals. In nm-scale layers, electron tunnelling is a possibility [76]. This phenomenon allows electrical contact between two 'bare' wires that have thin oxide layers (in the majority of cases). It is fairly well established that during PEO, dielectric breakdown occurs at the base of a pore, through

an oxide thickness of the order of 1 μm [77], which is nominally too thick for electron tunnelling. This is not to say that electrons cannot move through the oxide. It is established that many oxides such as titania can have highly variable stoichiometry and various defects and, as a result, allows relatively high electron mobility [78–80].

In terms of a band gap, these defects and vacancies could provide energy levels within the band gap, and assist motion of electrons through the material. Even so, a link is expected between a large band gap and low electrical conductivity. In this regard, it is expected that metals that are suitable for PEO processing should have large band gaps.

2.4.3 Dielectric Strength

The band gap, to an extent, determines the difficulty with which electrons can move through the oxide and by extension the rate that an electric field is built up across it. The dielectric strength is generally defined as the maximum electric field that can be sustained by the material before dielectric breakdown, usually given in V m^{-1}. In this regard, the dielectric strength is clearly a relevant property for PEO processing. Experimental values for relevant oxides such as alumina and magnesia are typically in the range 10 - 30 MV m^{-1}. It is difficult, however, to gauge the level of accuracy of these measurements, so it is probably better to use more well-established band gap values as an indication of dielectric strength.

2.4.4 Energetics of Oxide Formation

As discussed in §2.1, coating formation during PEO differs from anodising in that it is not strictly an electrochemical process. Oxide formation occurs when constituent ions combine upon termination and cooling of a plasma discharge. This plasma will contain a number

of species other than the substrate metal and oxygen (possibly electrolyte constituents but mainly hydrogen). The free energy change as the metal is oxidised will, therefore, dictate whether this process is more favourable than the recombination of hydrogen and oxygen into water as the plasma collapses. The free energies of oxidation at 0 K for various relevant metals and hydrogen were plotted by Clyne and Troughton. Their plot is reproduced in Figure 2.7. This only shows free energy of oxidation at 0 K, but it is expected that each value will increase more or less linearly as temperature increases, so it is still useful for ranking purposes. It is anticipated, therefore, then that all reactions with a less negative enthalpy than the formation of H_2O will have no thermodynamic driving force upon plasma collapse. These metals (Cu, Ni in Figure 2.7) will therefore be unsuitable for PEO processing, especially as it is expected that hydrogen is abundant in discharge plasma. This is a crude classification, especially since the oxidising agent is unlikely to be molecular oxygen, but it is certainly relevant that the oxidation of popular substrate metals (Ti, Mg and Al) is considerably more thermodynamically favourable than the recombination of H and O to form water.

2.5 Discharge Characteristics

2.5.1 Effect of Discharges on Microstructure

The study of discrete discharges is crucial to the elucidation of the basic processes of PEO. This understanding has been greatly advanced by use of the small area monitoring technique, first used in aqueous electrolytes by Klein [83, 84], and developed further by Dunleavy [41, 85, 86]. The principle behind the small area technique is that if the area to be processed is decreased sufficiently, only one discharge can occur at any one point in time. If a bulk sample is then processed in parallel with this sample, the voltage across both bulk and small

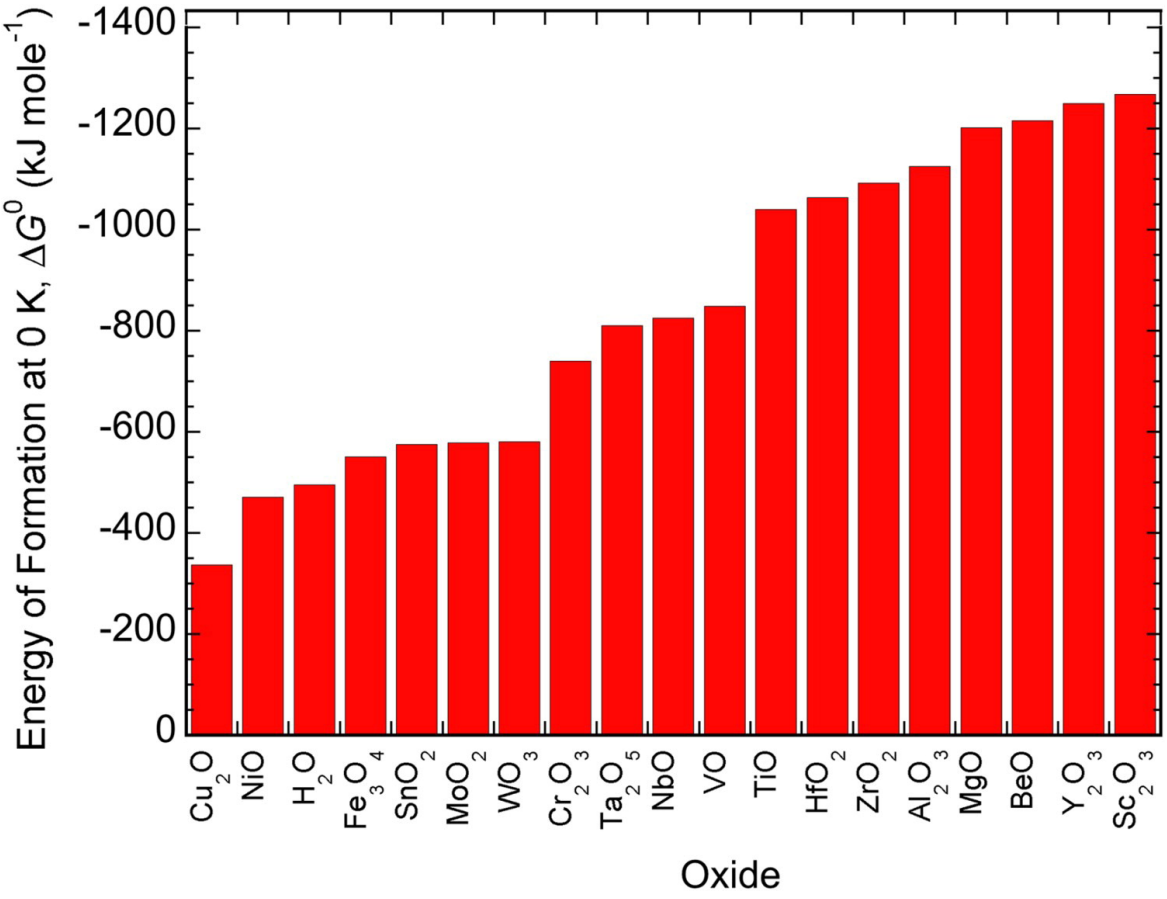

Fig. 2.7 Free energy values [81, 82] for the formation of various oxides from the metal, and of water from hydrogen, at 0 K. These energies are all expressed per mole of oxygen. For metals that can form more than one oxide, the data refer to the one for which the largest amount of energy is released. Reproduced from [74].

should be identical and discharge properties (e.g. light emission and current) can be measured whilst the PEO process as a whole proceeds as normal.

Early work using this set-up [41] found that the appearance of light emissions (discharges) coincided closely with current pulses of 30–40 mA. Figure 2.8 is a train of pulses recorded using the small area current method coupled with a photomultiplier tube (PMT) [41]. Dunleavy noted that this behaviour was common (i.e. that, temporally, discharges tended to occur in clusters with a relatively constant 'incubation' time between them). This phenomenon was termed a 'cascade'. Nominé and coworkers [77, 87] provided further evidence for this behaviour, by synchronising current monitoring of the small area sample with high-speed video recording. The key evidence from Nominé's paper is presented in Figure 2.9. This shows that during the period concerned, a series of discharges occurred at one unique location (on the small area sample), and only while the anodic potential was sufficiently high (about 400 V in this case). Typical discharge durations of 100 – 200 μs were recorded, with a typical incubation time of around 0.5 - 1 ms. There was a tendency for these characteristics to vary according to coating thickness; 'cascades' occuring later in the process (i.e. higher coating thickness) tended to be spaced further apart and their discharges tended to be more optically intense. Dunleavy [86] showed, however, that regardless of whether a discharge was weak or strong, it is highly probable that the mechanism producing them is the same, based on self-similar voltage curves of a range of discharge currents.

Troughton et al [77] took this work on 'cascades' further, by applying short ($\approx$ 1 s) treatments to a small area sample (of diameter 0.9 mm) on which a PEO coating of $\approx$ 100 μm had already been created. The small area was imaged in the SEM before and after treatment, and a small area current monitoring system was used in parallel with a high-speed imaging system, running at a temporal resolution of 5.12 μs. Figure 2.10 shows the small area sample before and after a 1 second treatment, and a stacked set of 200,000 images (similar to Figure

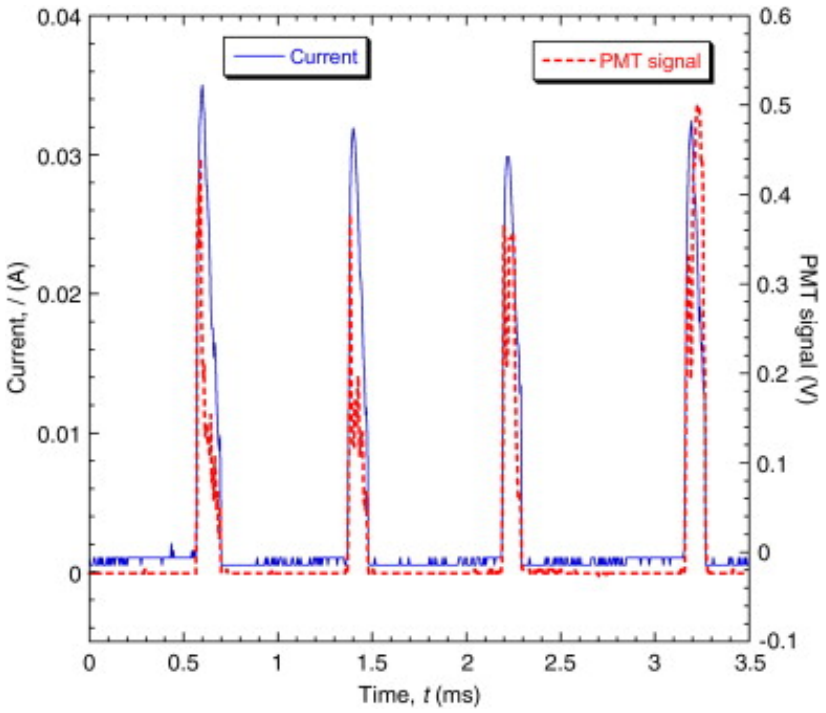

Fig. 2.8 A sequence of current pulses and associated light emissions captured by a PMT during DC processing of Al [41])

2.9) showing that all discharges during the treatment occurred at the same pore, and they all occurred as a ‘cascade’.

Computed tomographic reconstruction of the pore site in question revealed that the pore extends from the coating surface down to the substrate (as shown in Figure 2.11). It was found that cascades tended to continue in the same local area even if the process was stopped, the coating rinsed and dried, and the process restarted again. This suggests that microstructural features such as the pores in question here, are the reason ‘cascades’ form in these locations. The incubation time between discharges in a cascade may well represent the time required for the pore to refill with electrolyte, although this has not yet been modelled in detail or verified experimentally.

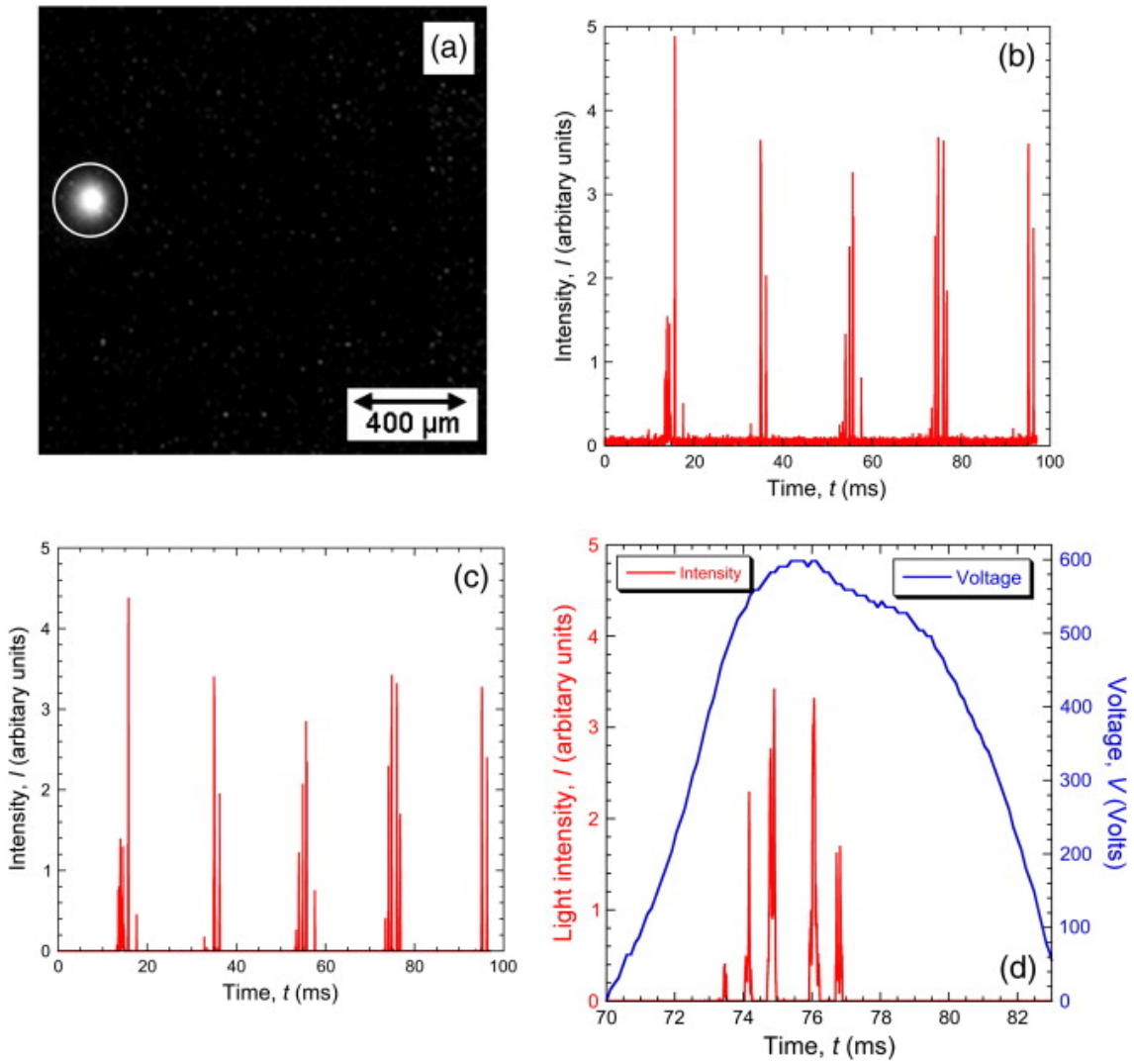

Fig. 2.9 Information from a sequence of 17,500 images, spanning a period of about 0.1 s, showing a) the entire sequence superimposed, b) total summed light intensity for each frame as a function of time, c) as for b) but only showing data from inside the circled region in a), d) a higher resolution plot of C), covering an anodic half-cycle, together with a typical measured voltage profile during that period [87].

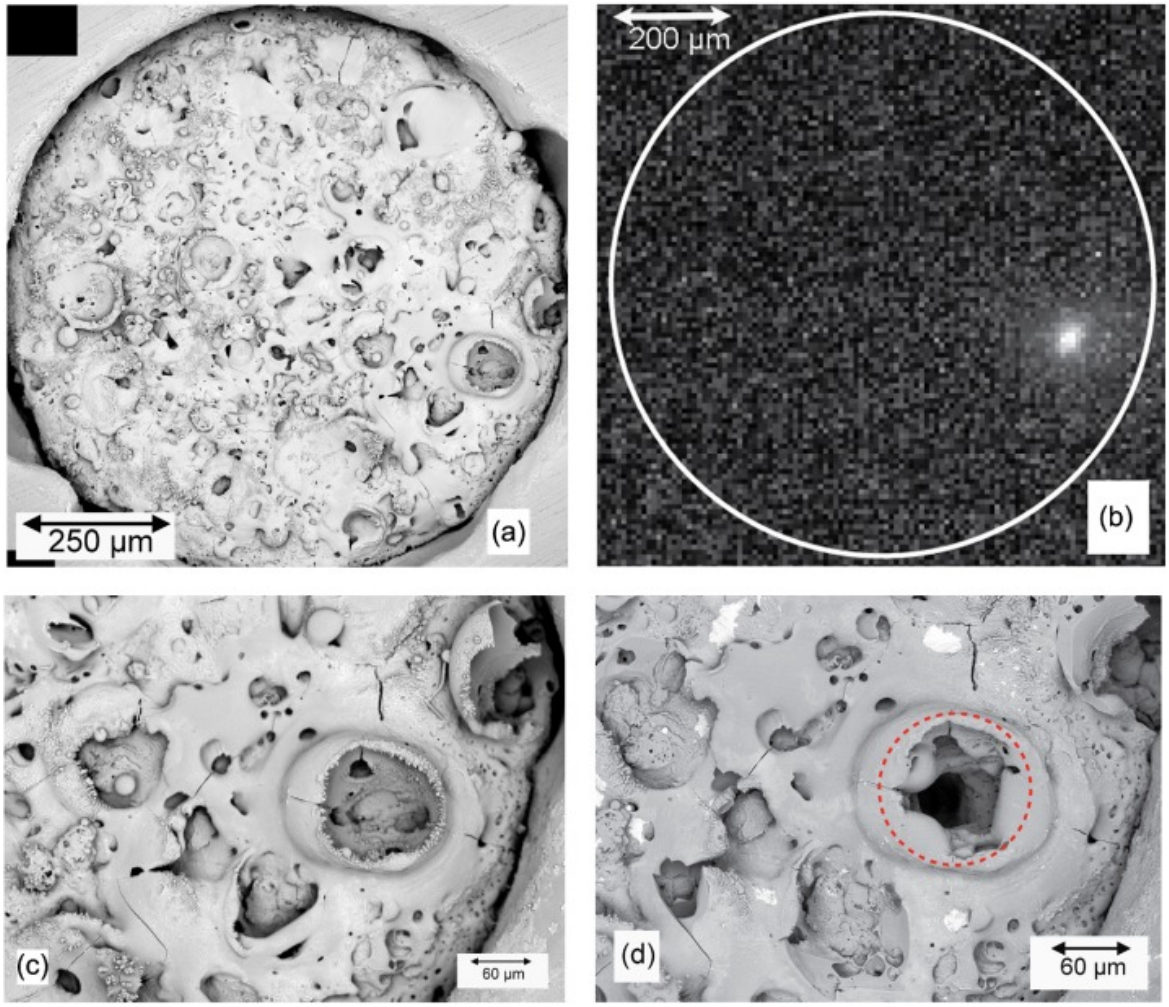

Fig. 2.10 Microstructural effects of a discharge cascade on a small area sample (with a 100 µm thick PEO coating) during processing at 2500 Hz for 1 s, showing (a) an SEM micrograph of the surface in the initial state, (b) a superimposed set of ($\approx$ 200,000) video images taken during the process, (c) a magnified SEM micrograph of the region indicated in (b) as the cascade location and (d) the same area after PEO processing (with the region in which the discharge was localised indicated by a dashed red circle) [77].

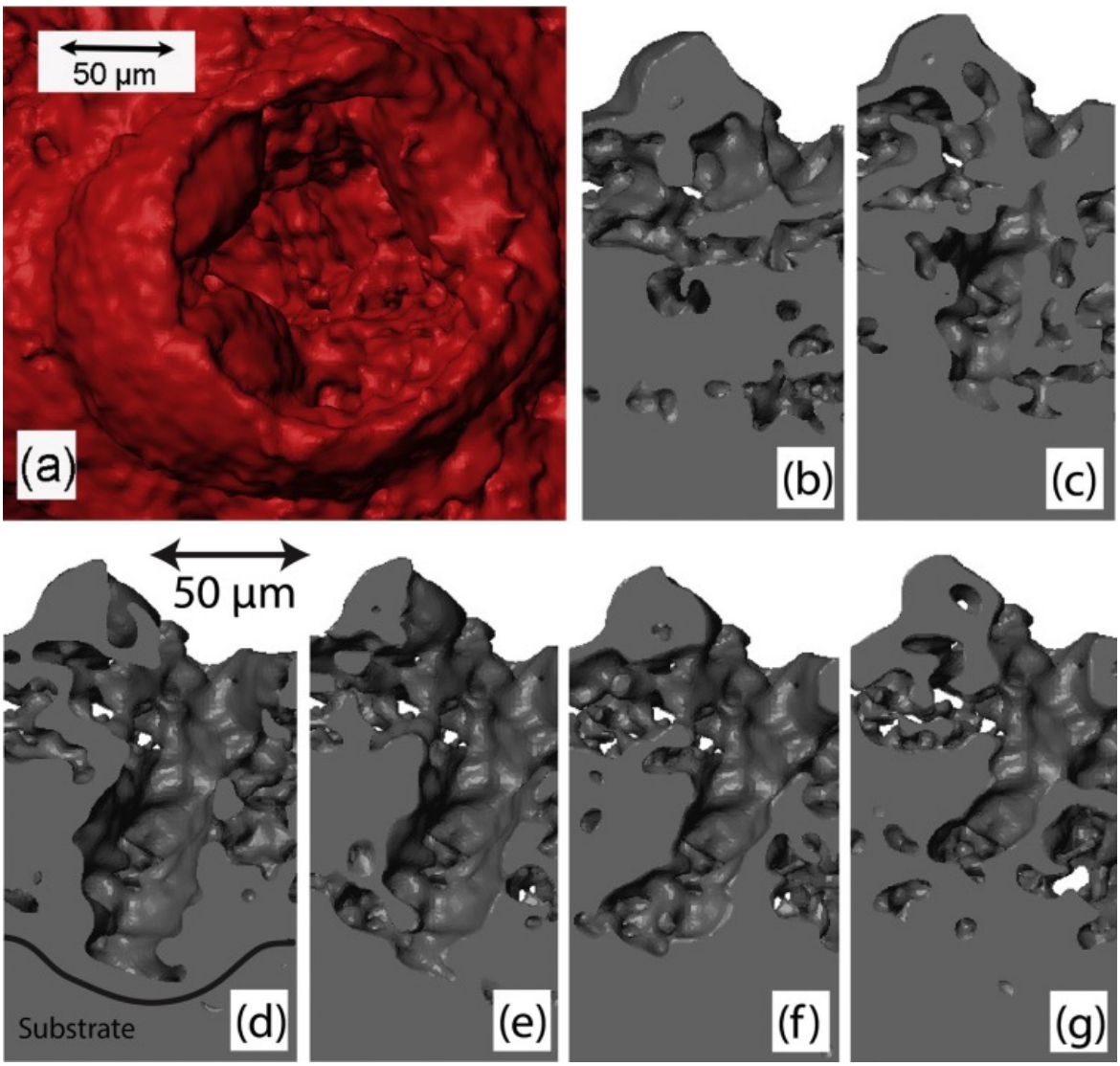

Fig. 2.11 Tomographic data from the circled region of the small area sample in Figure 2.10 (d), showing (a) a perspective view into the pore channel and (b–g) progressive parallel sections (11 µm apart), containing the through-thickness direction, with sections (d) and (e) located near to the approximate axis of the pore.

2.5.2 Cathodic Discharges

Some attention has been paid in recent years to the effect of cathodic polarisation during PEO processing [23–25, 88–95]. It has been established [24, 96] that the inclusion of a cathodic period was beneficial in terms of an increase in growth rate and wear resistance, although understanding of how this comes about is still unclear. It is likely, however, that the inclusion of a cathodic period allows hydrogen ions to combine with electrons, leading to evolution of hydrogen gas. This is unproductive in terms of coating growth, although it is possible that the associated charge redistribution could help promote the anodic discharges in some way. In any case, under the majority of conditions, in industry and research, discharges appear only when the substrate is under anodic polarisation.

Cathodic discharges have, however, been observed under certain conditions, such as when the electrolyte is highly alkaline, and when the coating is already relatively thick [88–90, 92]. This may relate to inhibition of hydrogen gas formation (respectively via a shortage of protons and a greater difficulty in moving them through the coating). The mechanism behind cathodic discharging is not completely clear, but it is helpful to first consider the mechanism of charge transfer during cathodic polarisation in the absence of discharges. In conventional AC processing, the applied frequency is typically that of mains (50/60 Hz). This gives a total cathodic polarisation time of around 20 ms, during which positively charged hydrogen ions can travel through the coating to combine with electrons from the substrate to form hydrogren gas. It follows that if H^+ ions were inhibited from combining with electrons, the electric field across the coating would climb as hydrogen ions (protons) were attracted to the surface. This inhibition could take the form of a shortage of H^+ ions (i.e. a high alkalinity), an increased distance of travel (as is the case for thicker coatings) or a shorter cathodic period in which the ions can travel (i.e. a higher process frequency). This electric field could in theory rise enough to cause dielectric breakdown of the oxide.

Nominé [88] explored this possibility by considering the kinetics of the movement of ions in the electrolyte. In this study, cathodic discharges were observed when the supply frequency was raised above a threshold value (around 2 kHz) and it was proposed that this was linked to a build-up of H^+ ions. This occurred because the shortened cathodic time period was too brief for the ions to travel through the coating. Troughton et al [89] explored this in more detail and concluded that cathodic discharges occurred during high (2.5 kHz) frequency processing only while the coating was sufficiently thick ($\approx$ 30 - 40 μm). Small area electrical data from this study showing cathodic discharges is presented in Figure 2.12. These cathodic discharges began to occur as the cathodic voltage rose past a threshold value, in this case around 250 V. The electrical set-up in this study was such that the anodic and cathodic voltage were free to vary in order to hold a pre-set current; so the rise in cathodic voltage is associated with a rise in the difficulty with which charge could pass through the oxide during cathodic polarisation. It was proposed that during high-frequency processing, an insufficient amount of protons were travelling through the oxide to carry the imposed current, leading to cathodic discharges.

It was intially thought that cathodic discharges could be beneficial, as in theory, they could cause oxidation of the substrate in much the same fashion as conventional anodic discharges. In practice, it was found that the onset of cathodic discharges coincided with a decrease in the rate of mass gain, most likely due to the cathodic discharges observed being stronger and more intense than typical anodic ones (i.e. carrying a higher current and having a high optical intensity). More work is required in the area of cathodic polarisation if the ability to control the intensity of cathodic discharges is to be gained.

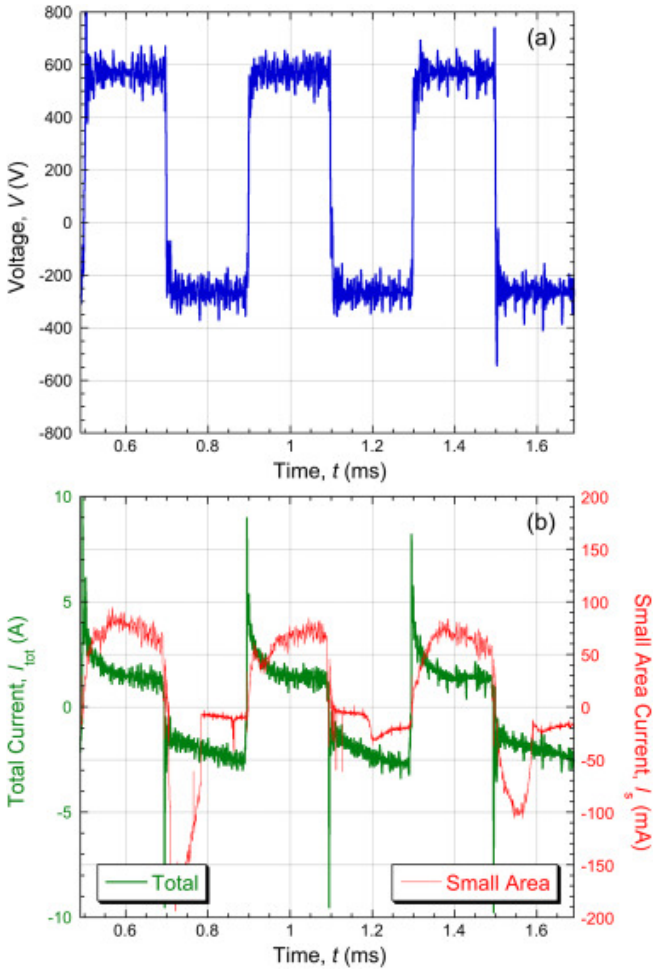

Fig. 2.12 Experimental data obtained during a single cycle of PEO processing at 2.5 kHz, with a coating thickness of about 40 μm, showing: (a) voltage and (b) current (both total and that flowing through the small area sample) [89].

2.5.3 "Soft" Regime

In recent years, there has been considerable interest in the so-called 'soft' regime [39, 51, 97–106], in fact a review of the topic was published in 2018 [107].Typically, under prolonged PEO processing, through-thickness discharges become more energetic and longer-lived. The 'soft' regime is a reported phenomenon characterised with a drop in both discharge optical intensity and anodic voltage. It also appears to improve the final free surface microstructure, by eliminating the large pores left by violent discharges. The regime was first studied in detail by Jaspard-Mécuson et al [105], and it was found that provided the ratio of anodic to cathodic charge (termed charge ratio, R) applied must be less than unity for the transition to occur. The transition appears to occur after a certain processing time, or once a certain coating thickness is reached, after which the anodic voltage begins to decline (under pre-set current conditions [104] - see Figure 2.13) and the discharge optical intensity reduces dramatically (see Figure 2.14). The transition appears to occur sooner for higher current ratios [51] and for older electrolyte (i.e. electrolyte used for 8 hours or more of conventional processing [39].) Matykina et al [108] found that the characteristic anodic voltage drop occurred sooner when an anodised layer was first formed on an Al substrate. This does suggest some kind of thickness-dependence.

Polished cross-sections of these coatings do not appear to exhibit large through-thickness pore channels, although examination of these microstructures on such sections can be misleading, due to the effects of the polishing. More convincing is the observation that the diameters of 'melt-pools' formed around discharge channels remain approximately constant [105] after the soft regime has been established (whereas, under standard conditions, these diameters tend to increase linearly with processing time). In a tracer study [109], it was found that all new coating growth occurred at the substrate-coating interface after the transition to lower applied potential occurred, which would explain why the 'melt-pool' diameters on

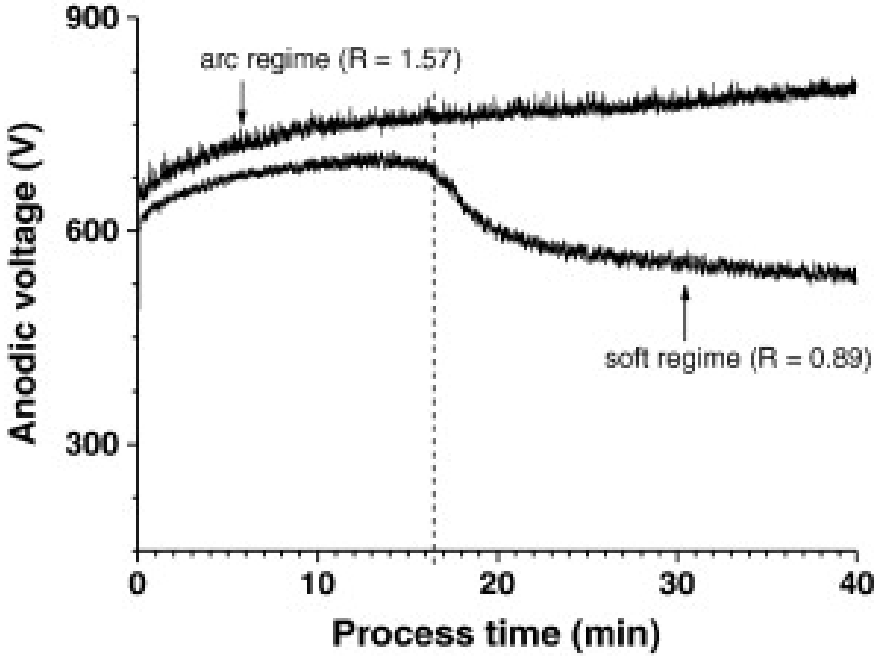

Fig. 2.13 Evolution of the anodic voltage over the process duration under standard conditions (termed arc regime) and soft regime conditions, with the transition to soft regime indicated by the dashed line [104].

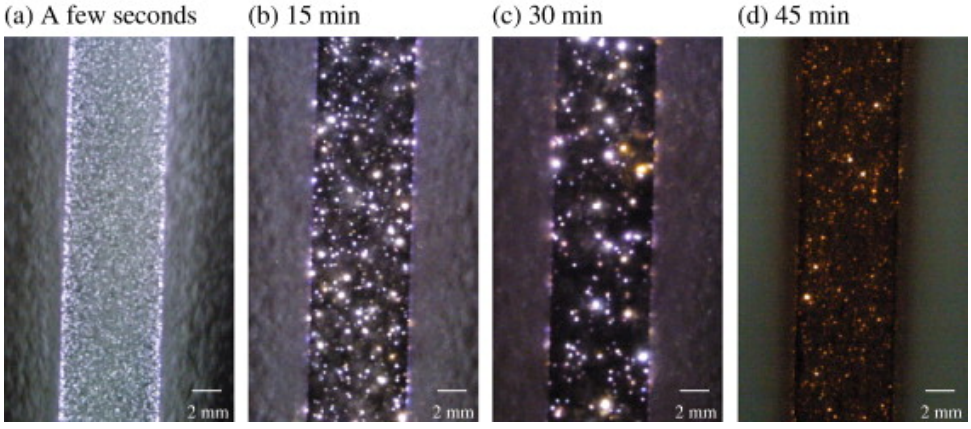

Fig. 2.14 Side-view photos of Al alloy samples at a different time during PEO processing (R = 0.89). The integration time was between 8 and 10 ms for photos (a–c), but 2000 ms for photo (d) [105].

the coating-free surface remain constant. The reduction in the applied potential during the transition to the soft regime suggests that the power consumed during processing in the soft regime should fall. Interestingly, the growth rate of the coating actually appears to increase after the transition [105]. There is no doubt, however, that more work is needed to confirm such effects. This, in part, is because the techniques used to measure coating thickness are often rather inaccurate. In general, the 'soft' regime is not well characterised, and although the effect of reducing power consumption while increasing the rate of mass gain is very desirable, it is unlikely that the regime can be reliably used until it is much better understood.

2.5.4 Energetics of Individual Discharges

PEO is a very energy-intensive process, and some efforts have been made to reduce the energy consumption, and some recent work has specifically aimed at improving it [110–113]. As with a lot of PEO studies however, there is rarely an underlying mechanism discussed in terms of energy consumption of the PEO process as a whole. In order to fully explore how the overall energy consumption may be reduced, it is useful to consider the energetics of the sequence of events occuring before, during and after a plasma discharge. It has been estimated [87, 114] that a typical discharge energy is $\approx$ 1 mJ, producing $\approx 10^{-16}$ m^3 of coating material. Clyne and Troughton [74] related this to a 1 s snapshot of a PEO process on a small area sample, where $\approx$ 300 discharges occured, leading to 0.3 J of energy being absorbed and 3 x 10^4 μm^3 of oxide being created.

Troughton et al [114] studied the energies associated with various phenomena taking place during PEO: initiation of a discharge, vaporisation of water and associated bubble growth, melting of existing oxide and substrate, heating of electrolyte and conversion of metal to oxide (which will release energy). Figure 2.15 gives a semi-quantitave presentation of the energies involved, and it can be seen that most of the injected electrical energy eventually

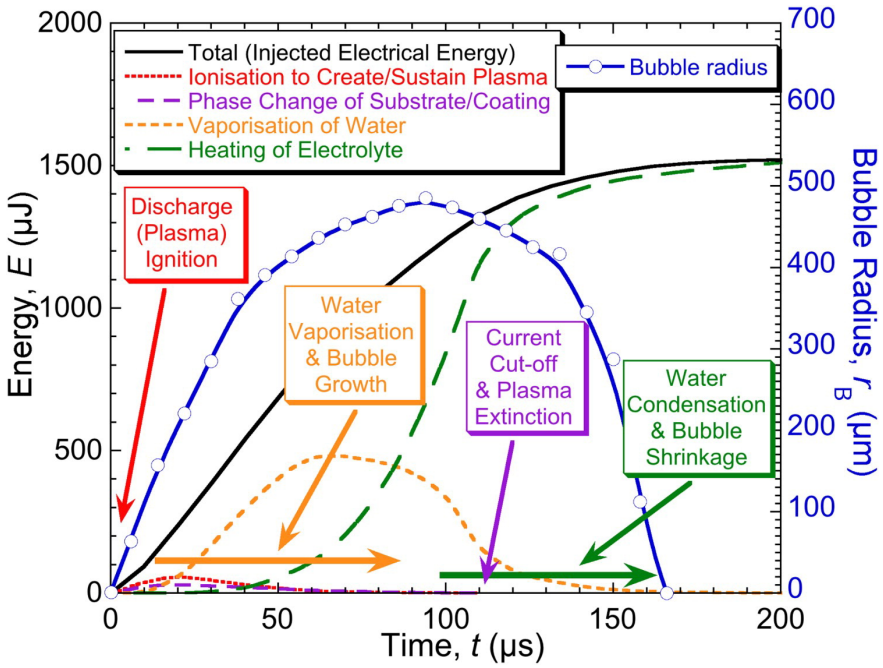

Fig. 2.15 A semi-quantitave representation of the energies involved in various phenomena associated with a discharge [114]

ends up as low grade heat transferred to the electrolyte, with little to no scope for recovery. There does not, at present seem to be an obvious way of reducing this energy wastage, although if one exists, it will need to ultimately increase the amount of coating produced per unit energy associated with a discharge. One area that shows promise in that regard is the incorporation of particles suspended in the electrolyte into the coating.

Chapter 3

PEO Processing with Electrolyte Additions

The incorporation of foreign particulate into PEO coatings shows great potential in terms of both reducing the energy consumption associated with producing a given thickness of coating and improving the functionality of the coating by improving properties such as corrosion and wear resistance. This chapter will explore and discuss the current literature regarding what is a relatively novel area in PEO research, namely:

1) Common particles used as electrolyte additions
2) Methods of particle dispersal in the electrolyte
3) Electrical response to electrolyte addition
4) Effect on coating properties; and
5) Theories regarding how the particulate is incorporated.

3.1 Particles Used in Electrolyte Additions

3.1.1 Oxide Particles

The majority of particles added to the electrolyte with the goal of incorporation into the coating are metal oxides. They are typically added as powder or sol and sometimes with the addition of a dispersal agent to reduce agglomeration (see §3.2). Incorporation of the particles is generally described as either ‘inert’, ‘reactive’ or a mixture of the two. The literature tends to describe an incorporation as "inert" when the added particles are detected either by SE microscopy / Energy Dispersive X-Ray Spectroscopy (EDX) to remain as discrete particles, as well as XRD data showing the existence of the phase of the added particle. Reactive incorporation refers to the case where there is an apparent absence of discrete particles in the coating (either on the free surface or in the cross-section) and XRD data reveals the presence of compounds including the substrate and added particle metal ions (e.g. the formation of $MgAl_2O_4$ on a magnesium alloy, processed in an electrolyte containing alumina particles [115]). Table 3.1 shows information from particle incorporation experiments in the literature.

Clearly, a relevant factor in predicting whether an oxide particle will incorporate inertly or reactively is the oxide melting point. Dunleavy et al [41] estimated the temperature of the plasma core of a discharge to be 16,000 $\pm$ 3500 K, with peripheral plasma regions still reaching between 3000-4000 K. In any case, the temperatures involved are at least sufficient to allow the PEO processing of Mg (MgO having a higher melting point than both Al_2O_3 and TiO_2). This gives a lower bound for local temperature of $\approx$ 3500 K, although it should be noted that the temperature locally can be much higher than this. Figure 3.1 gives the melting temperatures and particle sizes used in various studies in literature. An interesting case here is the study by Rudnev et al[120], which inertly incorporated manganese oxide into a Ti coating. This is initially surprising, given the relatively low melting temperature of this oxide

Oxide Added	Particle Size	Substrate	Incorporation Type	Reference
Al_2O_3	300 nm	Mg AM50	Inert	[115]
Al_2O_3	80 nm	CP (Commercially Pure) Ti	Reactive & Inert	[116]
Al_2O_3	200 nm	Al 7075	Unstated	[117]
CeO_2	560 nm	Mg AM50	Inert	[115]
CeO_2	5 μm	Mg AM50	Inert	[118]
Fe_2O_3	"nano" (can assume sub-micron)	Ti-6Al-4V	Inert	[119]
MnO_2	5 μm	CP Ti	Inert	[120]
SiO_2	"nano" (can assume sub-micron)	Mg AM50	Reactive	[121]
SiO_2	"micro" (can assume sub 10 micron)	Mg AM50	Inert	[121]
SiO_2	100 nm	Mg AM50	Reactive	[122]
SnO_2	Not Specified	CP Ti	Inert	[123]
TiO_2	200 nm	Mg AM50	Inert	[124]
ZrO_2	300-700 nm	Mg AM50	Inert	[115]
ZrO_2	150-300 nm	Pure Al	Reactive	[125]

Table 3.1 A range of oxide powders and sizes used in literature, and the reported incorporation type

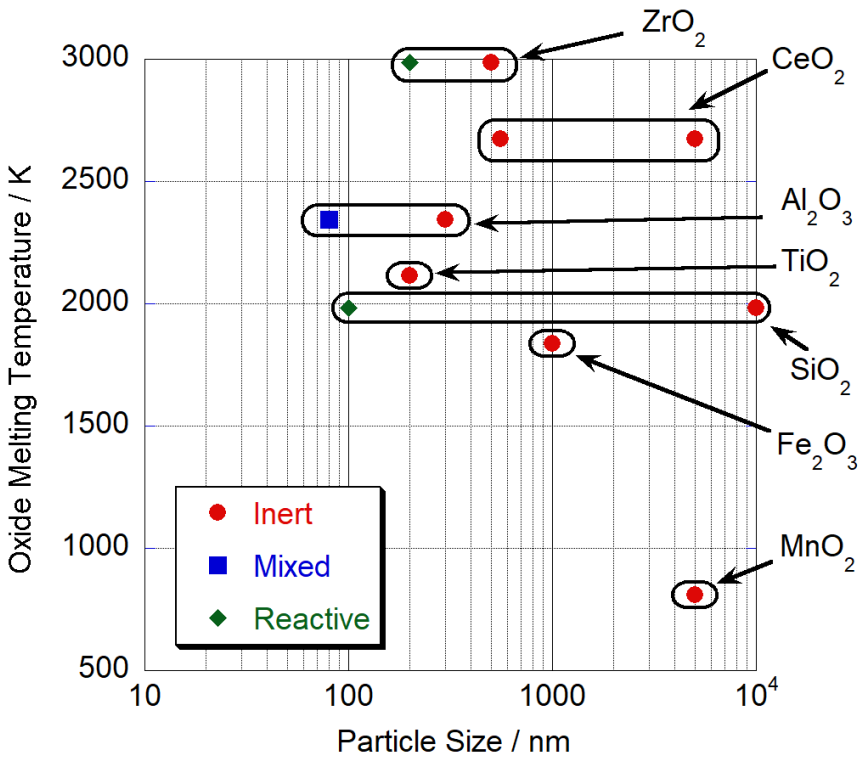

Fig. 3.1 A graphical representation of some data presented in table 3.1 (duplicated particle sizes are omitted) showing the melting point of each oxide, the particle size used in each study and the type of incorporation claimed by the author.

(808 K), so clearly another factor is at play here. Taking the MnO_2 5 μm case as an example, assuming a heat capacity of 54.1 J mol^{-1} K^{-1} and a density of around 5 g cm^{-3} [126], the energy needed to raise the particle to the melting temperature is of the order of 1 μJ, whereas the energy associated with a discharge is of the order of 1 mJ. Much of this energy is used in bubble growth and water vaporisation and is eventually lost to the electrolyte as low grade heat, but this value of 1 μJ is low compared to the energy of a discharge, so it is perhaps surprising that MnO_2 is not incorporated. In any case, there does seem to be a dependence on particle size; in that the highest particle size that has been incorporated reactively (from these studies) is 200 nm.

3.1.2 Non-oxide Particles

Although particles used in incorporation studies have mostly been oxides, some non-oxide particles have been shown to have been incorporated, leading to functional coatings. In particular, coatings with antibacterial properties have been formed by incorporation of silver particles [127–129], in fact a review was published on silver incorporation in 2018 [130]. The incorporation method associated with these particles has not been established from these studies, however examination of XRD data seems to suggest that the particles remain as metallic Ag; perhaps unsurprisingly due to the low driving force for oxidation of silver. It also appears, judging from transverse sections and free surface micrographs, that the particles appear to have adhered to the surface only and are not present through-thickness. This would make sense considering the functionality of the coating, since the antibacterial mechanism necessitates the direct contact of silver and bacteria, leading to the rupture of the bacteria cell wall. It would not, therefore, be particularly advantageous for silver particles to be trapped throughout the coating.

Biocompatible coatings have been enhanced with the incorporation of certain biominerals like hydroxyapatite (HA) [131–134] and other calcium phosphates. The aim with this type of coating is to improve the osseointegration of typical biocompatible Ti and Mg alloys, and HA layers are typically formed by addition of precursors (a common example is a mixture of calcium acetate hydrate and sodium dihydrogen phosphate hydrate [135]) which react during the course of PEO processing to form plate-shaped HA crystals on the free surface. Little in the way of a formation mechanism is given, but the shape of the crystals suggest a high cooling rate, so potentially the constituent ions were present in discharge plasma, which has then collapsed forming crystalline HA. It should be noted that HA production on PEO coatings is not strictly a case of particle incorporation as the precursor chemicals are added

as aqueous solutions, instead, adding these chemicals leads to the formation of a discrete new crystalline phase, which is relevant in the context of reactive incorporation.

Self-lubricating coatings have been created by the incorporation of solid lubricants into PEO coatings, such as polytetrafluoroethylene (PTFE) [4, 14, 136] and graphite [137, 138]. The general idea is that if lubricating particles are trapped homogeneously and through-thickness, as the coating is worn, more lubricating particles are exposed. Chen et al [14] found that the addition of an nonionic surfactant resulted in PTFE particles being more homogeneously distributed through the coating, as the particles were more dispersed. The challenge of homogenous dispersal will be covered in more detail in §3.2.

3.2 Methods of Dispersal

As mentioned previously, in most particle incorporation studies, the foreign particles are added as powder or sol. Occasionally (as is the case in most hydroxyapatite incorporation) particle addition is acheived in-situ by the precipitation of certain compounds if their solubility limit is exceeded in the base electrolyte. Regardless of the mechanism of particle addition to the electrolyte, a major challenge is the homogeneous dispersal and distribution of the particles throughout the electrolyte. The tendency of a certain particle type to agglomerate in a given solution can be evaluated by the zeta potential [139]. The magnitude of this value indicates the degree of electrostatic repulsion between particles in solution. A high (absolute) zeta potential is desirable, therefore, for homogeneous dispersal in the electrolyte. It was also theorised that a high absolute value could aid incorporation via electrophoresis; in theory this would increase mobility of the particle under the influence of an electric field. The zeta potential is usually negative for oxide particles in alkaline solutions (see Figure 3.2). There have been efforts to increase the magnitude of the value with the addition of surfactants, such

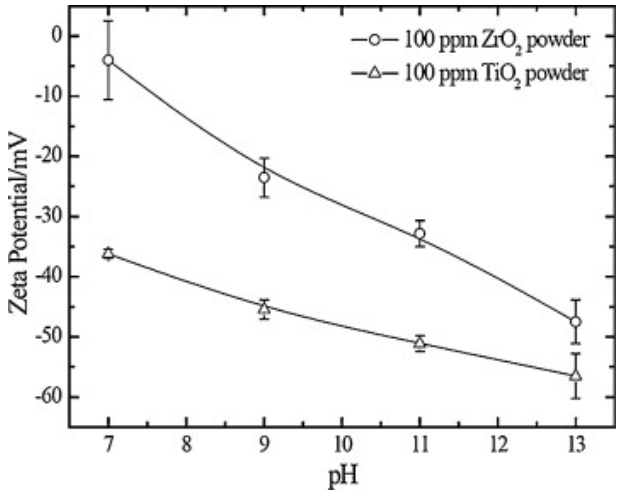

Fig. 3.2 Zeta potentials of ZrO_2 and TiO_2 at different pH levels in fluoride-based electrolyte. Reproduced from [142]

as carboxyl acids [140, 141] and PTFE [136], but the quality of the resultant PEO coating can suffer as a result. Often, mechanical agitation of the electrolyte is sufficient for dispersal (e.g. stirring, bubbling, electrolyte pumping and ultrasonication).

3.3 Electrical Response

The effect of adding particles to the electrolyte on the electrical response of the system is unclear to say the least, given the amount of contradiction in the literature regarding the subject. Li et al [143] published a finding that the voltage ramp at the beginning of the process is slowed with the addition of alumina particles, with the final processing voltage remaining the same. Wang et al [144], however, found the opposite, namely that the voltage ramped up faster at the beginning of the process, and that the final processing voltage was higher. This was claimed to be attributed to the faster growth rate of the coating when the particles were added, such that the voltage was driven higher by the increased thickness of the coating. This would appear to be a flawed theory however, as it has been well-established that if the process is continuing as normal, discharges are forming over a thin oxide layer

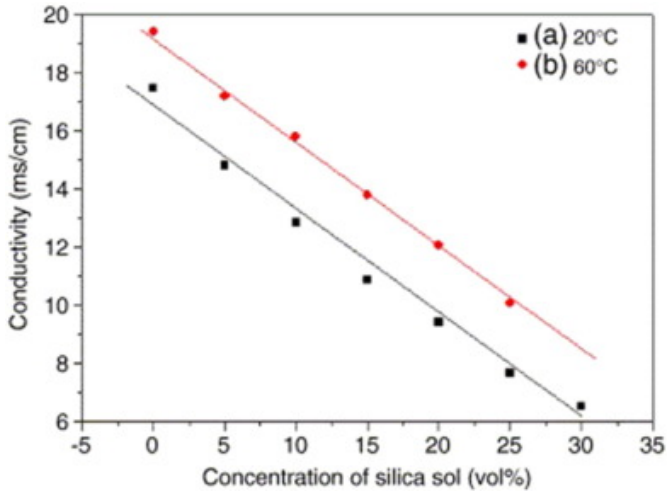

Fig. 3.3 The conductivity of a 1.0 M Na_2SiO_3 electrolyte with varied concentration of silica sol at (a) 20 °C; (b) 60 °C. Reproduced from [147]

near the substrate boundary and, as such, the breakdown voltage will be independent of the overall coating thickness. Lim [145] reported that the final voltage in fact decreased upon the addition of ceria particles, and others have reported that the electrical properties of the system are unchanged by the addition of foreign particles [46, 125, 146].

While there is little in the way of a consensus about the effect of particle addition on the electrical characteristics of the system, it is clear that the addition of insulating particles will alter the conductivity of the electrolyte. The results of one such study [147] are shown in Figure 3.3.

3.4 Effect on Coating Properties

3.5 Mechanisms of Particle Incorporation

The key issue in the relatively novel area of particle incorporation relates to the mechanism(s) of incorporation, since an understanding of this will guide optimisation of processing (and

control over microstructure) and will also be central to any attempt to maximise energy savings. There is no clear consensus in the literature about this issue. The following possible mechanisms of incorporation were identified by Shokouhfar & Allahkaram [146], who attributed them as indicated:

1) Nano-particles agglomerate in micro-pores (presumably discharge sites). They could, however, be ejected during eruptions of molten oxide [148].

2) Continuous micro-discharges trap nano-particles inside molten oxide [121, 149, 150].

3) Nano-particles are adsorbed into the coating by electrophoretic forces [149, 151, 152].

4) The high temperature of the micro-discharges locally melts the oxide so that nano-particles stick to the coating surface [153].

5) The high temperature of the micro-discharges melts the nano-particles, which may then react with substrate oxide to form new phases, cover micro-channels and seal them. [121, 152].

In fact, such mechanisms, or variants of them, have also been suggested by a number of other workers, as outlined in the review of Lu et al. [40]. Shokouhfar & Allahkaram [146] concluded from their own work that mechanisms 1) and 3), as listed above, were the most significant. Other relevant work includes that of Matykina et al. [109], who studied the through-thickness distribution of zirconia nano-particles incorporated into Al PEO via a silicate electrolyte. They observed a tendency for them to be concentrated towards the outer regions of coatings, which were up to about 200 μm thick. Their observations included some particle incorporation during a so-called "soft sparking" (see §2.5.3) regime and they also consider the possibility of electrophoretic effects, but they came to no clear conclusions about probable mechanisms of incorporation. Also relevant in this context is the work of

Liu et al. [154], who compared coatings produced with very fine (70 nm) and somewhat coarser (350 nm) chromia suspensions. They found that the latter were concentrated near the free surface of the coating, while the finer particles tended to be distributed throughout the coating. In fact, there have been a number of reports indicating that finer particles tend to be incorporated more readily and at an earlier stage in the process. Such reports suggest that the incorporation of fine particulate is strongly linked to discharges. There have also been various observations, such as those of Erfanifar et al. [155], specifically suggesting that "nanoparticles are driven to discharge channels due to sparking".

It is possible that different mechanisms might be active under different conditions and various investigations have covered a wide range of combinations of substrate, electrolyte composition and particle type (in terms of both size and chemical composition). The majority of these have been oxides in the form of "nano-particles". While particle size distributions have been provided in relatively few cases, it seems clear that most of the particles successfully incorporated during PEO have been around 1 μm or below in diameter. Furthermore, the addition levels in the electrolyte have typically been in the approximate range of 1–10 g L^{-1}.

Nevertheless, few clear guidelines are available in the literature concerning the way that particulate become incorporated during PEO, or how its incorporation can be controlled. For example, there have been very few studies in which effects of particle size have been systematically studied (apart from a general perception that it happens more readily with "nano-particles"). Moreover, while there have been many microstructural examinations of PEO coatings containing particulate incorporated via suspension in the electrolyte, this has rarely extended to quantification of their proportions in the coating, or how this relates to particulate concentration in the electrolyte or other processing variables.

It seems logical to consider incorporation mechanisms in terms of the basic cycle of a discharge during PEO, which is one of dielectric breakdown (across a thin oxide layer on the substrate), expansion of the plasma into a relatively large gas bubble, shutting down of the current (due to the increasing electrical resistance of the plasma), cooling/collapse of the bubble and finally refilling of the resultant pore with electrolyte. It might be expected that, depending on the size and spatial distribution of the particles, the main incorporation mechanism would be one of suspended particles being swept into the pore during refilling and subsequently becoming physical entrapped (which could be regarded as mechanism 1) in the above list). For this to be effective, the particles will need to be appreciably smaller than the pore diameter, which, in terms of magnitude, is typically 5–30 μm in most cases (with a distinct tendency to become larger as the coating thickens). This is consistent with reports that finer particles can become incorporated at an earlier stage in the process than coarser ones (although these refer to cases in which all of the particles are sub-micron in diameter).

Furthermore, in order for the final volume fraction of particulate in the coating (and consequent energy gains) to be significant, the total mass of particulate swept into a pore at the end of a discharge will need to be comparable to the mass of coating formed during a single discharge (by oxidation of substrate material during cooling of the plasma). Of course, this does not necessarily exclude a role for effects such as "electrophoretic forces", causing charged particles to move under the influence of an electric field. Such fields do arise during PEO, and it is certainly possible for suspended particles to acquire charge. In fact, there have been several studies [156–160] involving PEO processing in the presence of suspended particulate, many of them aimed at biomedical applications, in which it has been assumed that these particles were deposited on the free surface of the coating via electrophoretic forces. Whether such forces could in fact be significant compared to those generated during discharge events is, however, unclear (and does not appear to have been examined theoretically so far).

Chapter 4

Experimental Methods

4.1 PEO Processing

All PEO processing in this study was performed on a 10 kW commercial rig with a 50 Hz sinusoidal coupled supply. This 'coupling' effectively means that the total charge transfer in the anodic and cathodic half-cycles must be equal. In all cases, a current density was pre-programmed and the machine held this preset value through the control of a network of variable capacitors. The electrolyte bath has a volume of 25 L, and the temperature of the electrolyte was kept between 20 and 25$^{\circ}C$ by circulation through a heat exchanger. The outlet of the electrolyte circulation loop has a posable nozzle (of diameter 10 mm) attached which allows the outlet jet to be pointed at or away from the sample, for use in jetting experiments.

For each substrate, the electrolyte was chosen such that it would produce a coating consisting mainly of the substrate metal oxide. For Al, the exact composition used was commercially sensitive, but contained approximately 1-2 g L^{-1} potassium hydroxide (KOH), 3-5 g L^{-1} sodium silicate (Na_2SiO_3) and 3-5 g L^{-1} tetra-sodium pyrophosphate ($Na_4P_2O_7$)

and has a pH of 12.5. This composition has been shown to produce a coating consisting of various phases of alumina [1] when used to process Al substrates. For Ti and Mg substrates, an electrolyte containing 5 g L^{-1} of sodium phosphate tribasic (Na_3PO_4) was used. This has been shown to produce mainly titania [3] and magnesia [161] on Ti and Mg substrates respectively. This electrolyte had a pH of 12.4. These conditions represent a typical industrial set-up.

4.2 Sample Preparation

4.2.1 Plate Samples

Plate samples were prepared with the dimensions shown in Figure 4.1. Samples were made from 1 mm thick Al 1050 ($>$ 99.5% Al) sheet and 1 mm CP Grade 2 Ti sheet ($>$ 99.3% Ti). For Mg samples, 5 mm thick plates were cut from a $>$ 99.0% Mg ingot (the current was therefore increased for Mg samples to account for this increase in surface area, giving a constant current density across the three metals). For all except the "jetting through holes" experiments in §7.4, samples with cross-sectional dimensions shown in Figure 4.1 a) were used, and dimensions shown in Figure 4.1 b) were used for hole-jetting experiments.

4.2.2 Small Area Samples

Samples used for small area investigations in Chapter 5 were composed of a small wire mounted in parallel with a bulk sample of the same metal. These wires were produced by cutting a thin section from the bulk material and swaging a wire through successively smaller dies until the desired diameter (1 mm) was achieved. The wire and bulk sample were

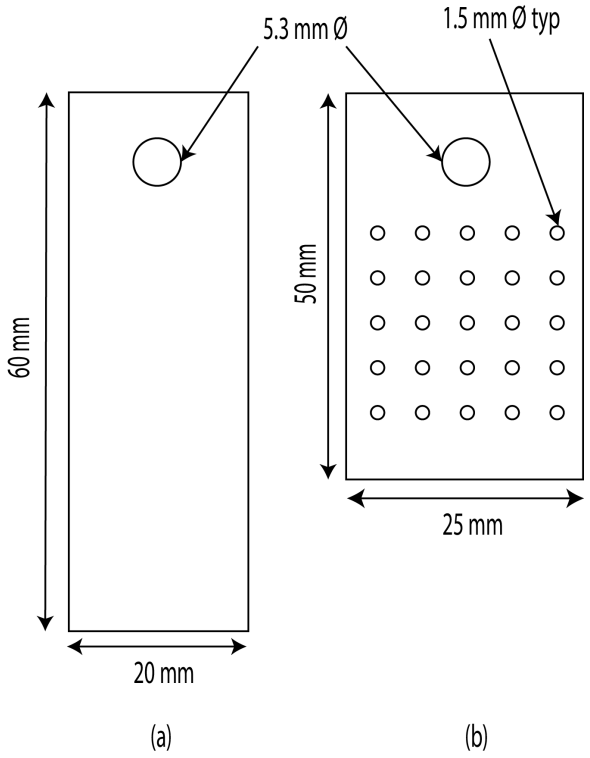

Fig. 4.1 A diagram of the plate samples used. Design (a) was used for non-jetting and side-on jetting, (b) was used for through-hole jetting.

connected to a pair of PVC insulated twisted wires extending out of the tank where a resistor for current monitoring connected the ends of the wires.

4.3 High Speed Video

Individual discharges were recorded visually using a Phantom V12.1 high-speed camera with a 2x teleplus lens and NIKON lens with a focal length range of 3–0.1 m.The small area sample was viewed through a glass window at a distance of $\approx$ 200 mm. The length of each recording is limited by the memory of the camera (16 Gb), however this memory can be partitioned such that multiple shorter sequences can be captured before the data has to be transferred out, which can take up to 30 minutes. With the memory limit in mind, the settings of the camera are a compromise between frame rate, capture length and image resolution. After trialling, it was found that 300 ms represented a length of time where the probability of capturing at least one discharge was reasonably high on each substrate, while a resolution of 128×128 pixels was deemed to provide satisfactory visual data. This limits the frame rate to 187290 fps, with an exposure time of 4.61 μs and an interval between frames of 5.34 μs (the discrepancy between these two times represents the time the camera takes to write each frame into the hard-drive). Still images of the small area samples used are shown in Figure 4.2 (a) (b) and (c). Note that the frame rate has been decreased to 24 for these images to allow the shot to be taken; at higher frame rates the exposure is low enough that the sample cannot be seen unless a discharge is taking place.

While investigating bulk optical processing characteristics in §5.2.2, the frame rate was reduced to 5000 fps (corresponding to an interval of 200 μs between frames). The exposure was kept low at 5 μs in order to avoid saturating the camera with large discharges. The

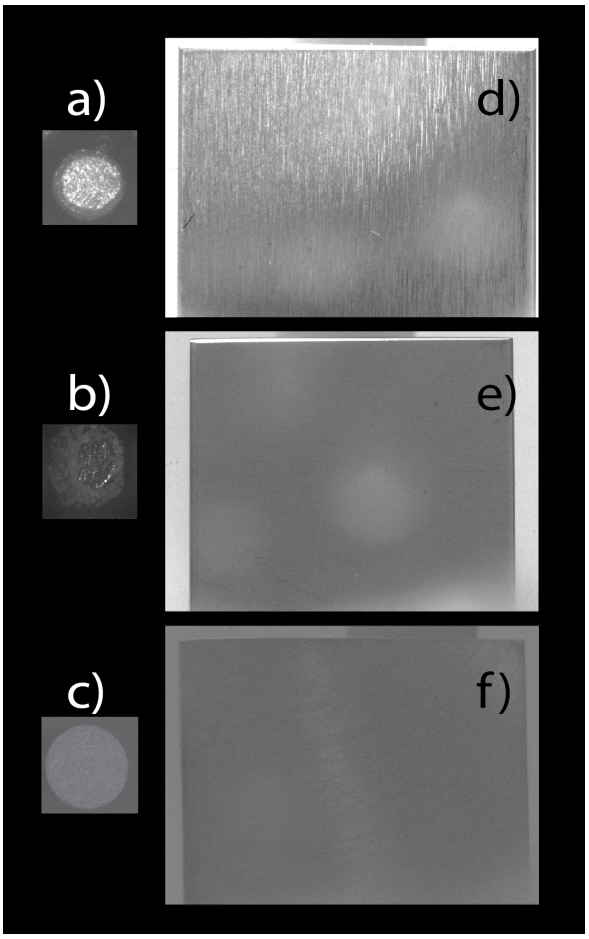

Fig. 4.2 Still images of all samples in situ: a) Al small area, b) Ti small area, c) Mg small area, d) Al plate sample, e) Ti plate sample and f) Mg plate sample.

resolution was increased to 640 × 480 pixels, which allowed for a total recording time of 564.800 ms. Still images of the bulk samples in situ are given in Figure 4.2 (d) (e) and (f).

4.3.1 Image Processing

For the bulk optical study in §5.2.2, further image treatment was needed to produce meaningful results. This processing was performed using the ImageJ software package. Video data were converted from the Phantom (camera manufacturer) proprietary '.cine' format to '.avi', and converted to a stack of images using the software. The '3D stack' function was used to view every frame of the video sequence superimposed onto each other.

4.4 Electrical Monitoring

The small area electrical monitoring technique was developed by Dunleavy [41, 85, 86] and has been well-established as a reliable technique in the study of individual discharges by Troughton and co-workers [77, 89, 114]. It works on the principle that as the area being processed decreases, the probability of more than one discharge event occurring at the same time also decreases. Therefore, by measuring the current flowing through a small area, the current-time profile of an individual discharge can be obtained.

Electrical data were collected using a four-channel, 8-bit resolution PC oscilloscope (Pico Technology, Picoscope 6403), with a sample interval of 51.2 ns for small area studies, and 250 μs for bulk studies. The Picoscope was operated using a laptop with a USB opto-isolator, which converts an electrical signal to an optical signal, and then back to an electrical signal. This was necessary to avoid ground loops between the laptop and floating ground of the power supply. The voltage across the electrolyte tank was measured using a 100× potential

divider, and the current was calculated by measuring the voltage drop across a 1 Ω resistor connected in series between the counter-electrode and the power supply.

The small area current was determined by measuring the voltage drop across a 10 Ω resistor using an active differential probe with $\times 10$ attenuation (Pico Technology TA043), and the connecting wires were twisted together to reduce electrical noise in the current signal.

4.5 Synchronised Electrical and Video Monitoring

To allow synchronised collection of visual and electrical discharge data, the Picoscope electrical monitoring system was set to start recording upon recieving a falling edge into one of its inputs. This was generated by the camera when the user pressed the 'record' button on the camera software. The time difference between the camera and electrical recording start points was approximately 5 ns, which was deemed to be negligible. A diagram showing the electrical monitoring circuitry is given in Figure 4.3.

4.6 Mass Change Measurement

While conventional sectioning and study of (SEM) micrographs are often used to monitor the progression of coating formation, a more reliable and accurate technique was required for the present study. This was done via sample weighing, using a balance with a resolution of about ±1 mg. This allows averaging over the whole of the sample (rather than being dependent on the sections viewed being representative), allows more accurate measurement and is focused on the amount of new coating mass being created (with no dependence on its porosity level). All samples were flushed with de-ionised water, ultrasonically cleaned in acetone and then

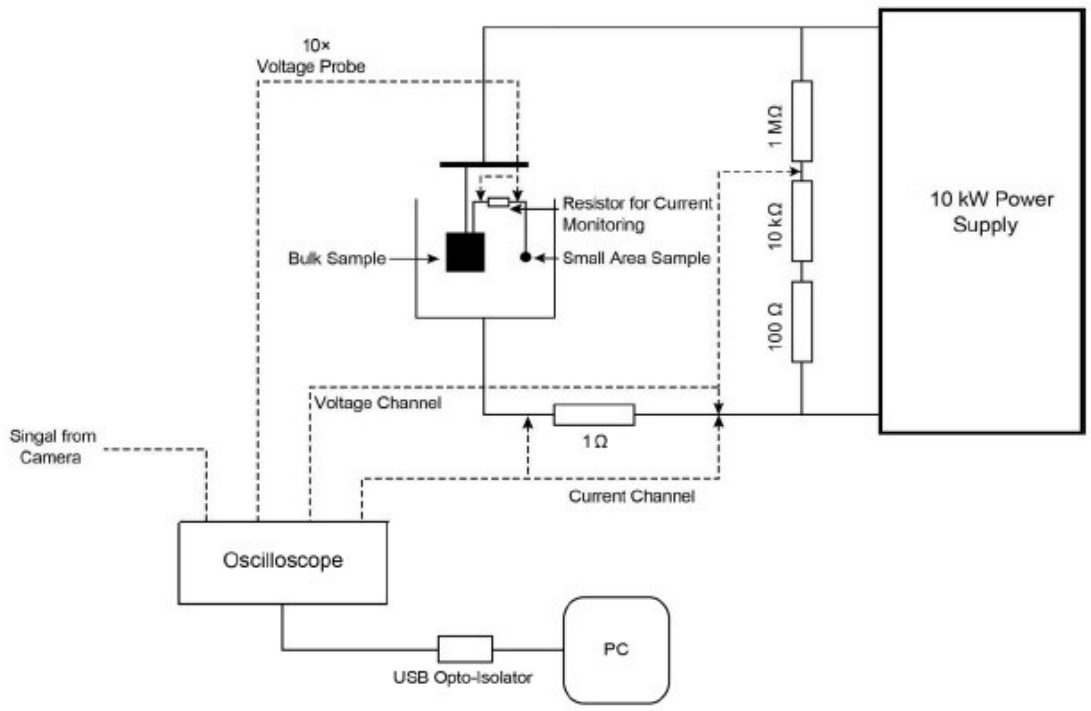

Fig. 4.3 Schematic diagram of the synchronised electrical and video monitoring set-up.

dried before weighing. Of course, the weighing method reflects the average rate of coating formation over the surface of the sample.

4.7 Microstructural Examination

4.7.1 Metallographic Preparation

The transverse sections of plate samples were examined by cutting off a thin ($\approx$ 5 mm) strip using a Struers Secotom-10 precision saw, and mounting it face down using a Buehler Simplimet hot mounting press with conductive bakelite. The sample was then progressively ground to 4000 grit SiC, followed by polishing with 1 μm and finally 0.25 μm diamond paste. An oil-based lubricant was used to prevent excessive oxidation of the pure metal substrates.

4.7.2 Scanning Electron Microscopy

Both free surface and transverse section samples were examined using scanning electron microscopy in both secondary electron (SE) and back–scattered electron (BSE) mode. Prior to imaging, samples were sputtered (Emitech K550, 30 mA for 3 minutes) with a thin (calculated to be $\approx$ 10 nm from the equipment manual) layer of gold to prevent surface charging. SEM observations were carried out on a FEI Nova NanoSEM using a field emission gun.

4.7.3 Thickness Measurements

Coating thickness measurements were made from SEM cross-section images. Image processing software ImageJ was used to define both edges of the coating, by thresholding the images and tracing a line along the boundaries. The mean separation of the two lines was taken as the coating thickness, and the standard deviation calculated for the error. The length over which the measurements were made was in excess of 15 times the coating thickness in all cases.

4.7.4 X-Ray Diffraction

Plate samples to be studied using X-Ray diffriction were cut into 25 $\times$ 25 mm squares. Phase identification was achieved by performing a standard $\theta - 2\theta$ scan between 20 and 80 degrees in 2θ using a Bruker D8 Advance instrument with a step size of 0.05 degrees and a dwell of 1 s. This diffraction program proved sufficient for identifying all major peaks of relevant phases (i.e. those peaks with an expected intensity of 15% of the maximum peak intensity).

4.8 Particle Size Distribution Analysis

Three different types of particulate suspension were added to the electrolyte. These were: (i) "30 μm diameter" Al_2O_3 powder (supplied by Alcoa), (ii) "7 μm diameter" MgO powder (from American Elements) and (iii) "100 nm diameter" Al_2O_3 powder (supplied by Alpha Aesar). Since these particles were added during PEO processing of both Al- and Ti-based substrates, the study encompassed some cases in which the particles were chemically similar to the oxide formed during normal processing and other cases in which they were chemically different. The SEM micrographs in Figure 4.4 show that powder (i) is composed of relatively coarse, well-dispersed spherical particles (Figure 4.4(a)), while powder (b) comprises finer, less regularly-shaped particles, with some agglomeration and a fairly broad size distribution (Figure 4.4(b)). The 100 nm powder is actually composed of individual spheres in the approximate diameter range of 30–100 nm (Figure 4.4(d)), although there is a tendency towards agglomeration into clusters a few hundred nanometers in size (see Figure 4.4(c)). A laser particle size analyser (Malvern Panalytical Mastersizer 2000) was used to measure the particle size distributions of two of these powders. However, powder (iii) is too fine for this technique. The resultant particle size distributions are shown in Figure 4.5. It can be seen that these distributions are consistent with the SEM micrographs and also, broadly, with the size designations of the suppliers. In order to minimise agglomeration of particles in suspension, the powders were first introduced into a small volume of electrolyte and a magnetic stirrer was used for different periods to disperse them thoroughly, before this liquid was added to the bulk. Longer periods were used for the finer particles. For each type of particulate addition, three final levels of suspension in the electrolyte were used. These were: (a) 1, (b) 2 and (c) 4 g L^{-1}. From the densities concerned, these levels approximately correspond (for both materials) to 0.025%, 0.05% and 0.1% by volume. The average spacings between particle centres when in suspension, for the highest concentration, are thus around: (i) 250 μm, (ii)

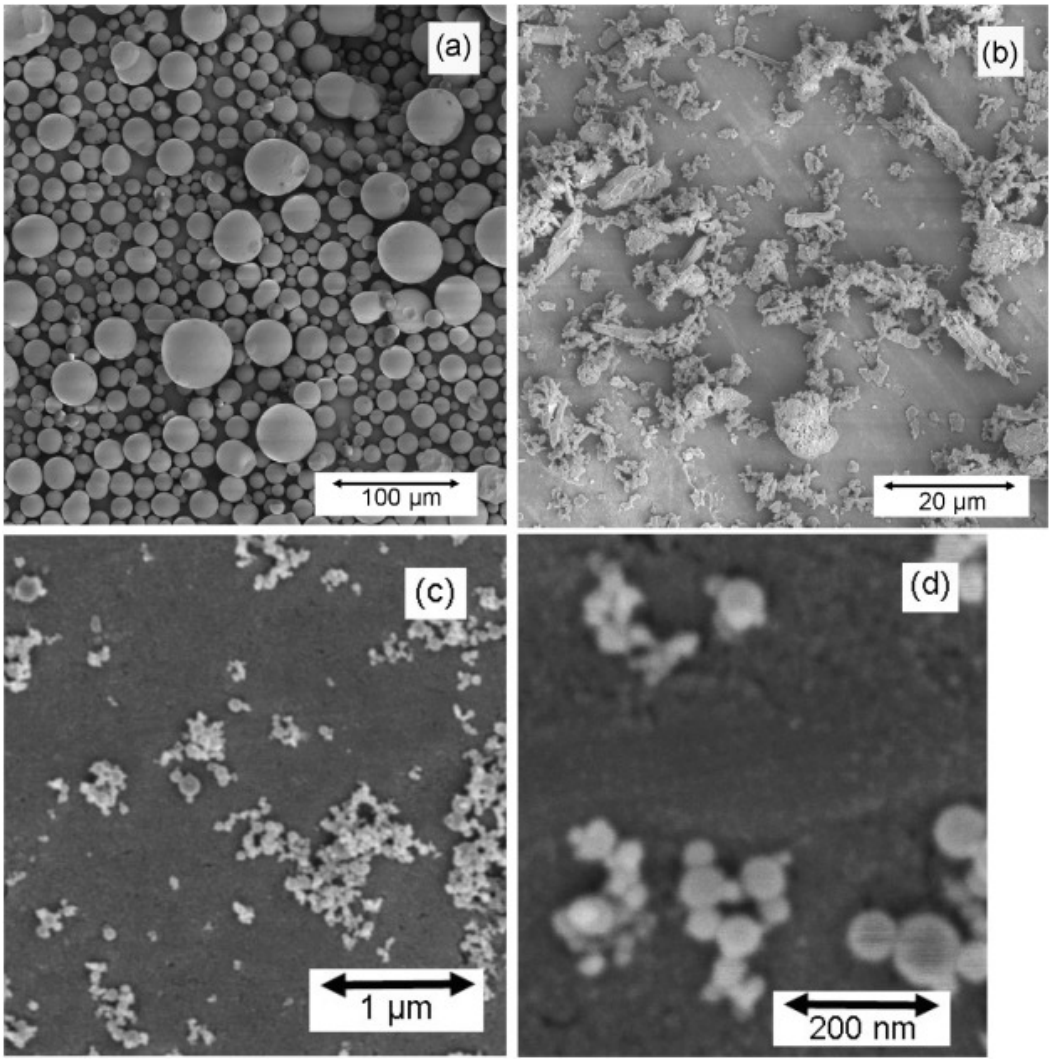

Fig. 4.4 SEM (SE) images of the three as-received powders, showing (a) 30 μm Al_2O_3, (b) 7 μm MgO and (c) and (d) 100 nm Al2O3, at lower and higher magnification.

50 μm and (iii) 0.8 μm, with these figures raised by a factor of about 70% for the lowest concentration. Such information is potentially helpful when considering how the particles might become incorporated into the coating during PEO processing.

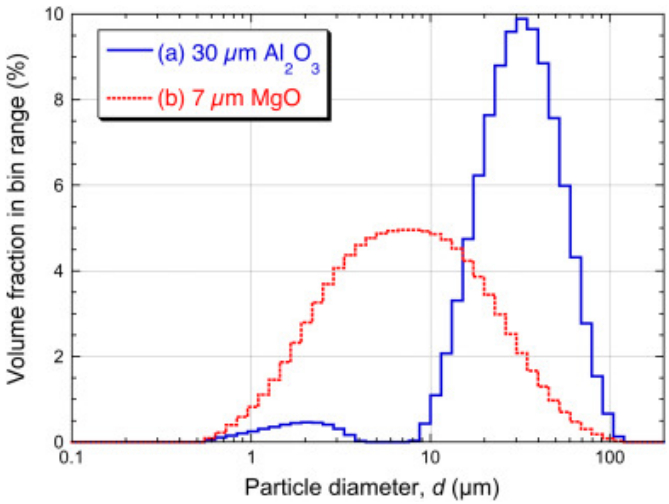

Fig. 4.5 Particle size distributions for two of the three as-received powders.

4.9 Fibre Milling

Chapter 7 studies the effect of the addition of alumina fibres to the electrolyte. The ideal fibre needed to be fine enough to allow the possibility of entrapment in a ≈ 20 μm pore, while remaining large enough to be able to handle safely without difficulty. "Saffil"® fibres were selected for this purpose, since they have a diameter of about 3 μm (and are free of the coarse "shot" that is present in some such products). They were supplied by Saffil Ltd (Widnes), as chopped fibre mat. These fibres are routinely used for high temperature insulation purposes, being predominantly δ-Al_2O_3 and being stable up to about 1600 °C. They have also been investigated extensively for other purposes, notably as reinforcement in Metal Matrix Composites.

In the as-received form, most of the fibres are relatively long (mm range), such that the entanglements give the material handling strength for insulation purposes. In this form, it was not suitable for mixing with the electrolyte. It was thus subjected to short milling operations, in a ball mill (DECO All-Direction Planetary Ball Mill). A 1.5 litre alumina chamber was used, containing 200 alumina balls of diameter 10.75 mm. The most suitable arrangement

was found to be five layers of balls, separated by four layers of fibre mat, each layer being about 5 g in weight. The rotational speed of the container was 300 rpm, with the sense of rotation being reversed once every minute. It was found that this arrangement gave good mixing and milling efficiency, with the average fibre length being progressively reduced.

The objective was to have fibre aspect ratios of the order of 10–20, it being anticipated that this would be low enough to allow good mixing within the electrolyte, but high enough to retain fibrous "effects", such as toughening, and the creation of an inter-linked network. Since this corresponds to fibre lengths of the order of 30–60 μm, it can be seen that the milling time of 5 min was most suitable. Longer times led to aspect ratios that were too low (with the product effectively starting to become a fine powder after about 10–20 minutes). On the other hand, after times of less than 5 min, the mat was still too tangled for effective blending with the electrolyte. A milling time of 5 min was therefore used to mill all the fibre used in the study described in Chapter 7. The fibre aspect ratio after various milling times is shown in Figure 4.6. A BSE micrograph of the fibres after milling is shown in Figure 4.7.

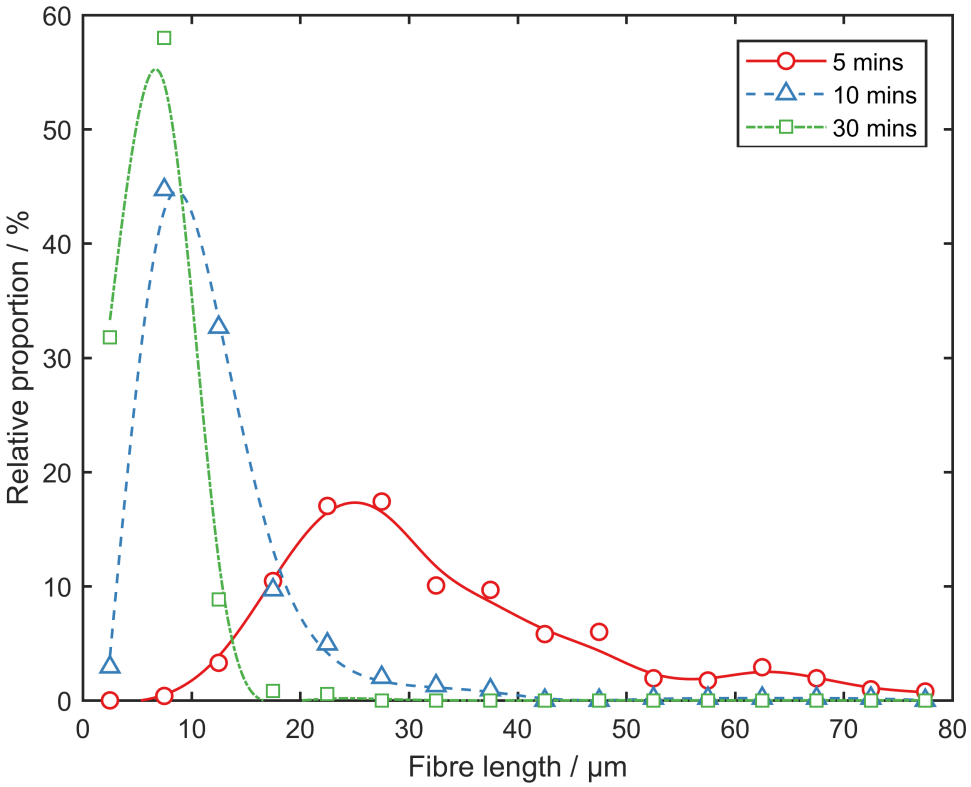

Fig. 4.6 Fibre length distribution after different milling times, measured using SEM image analysis.

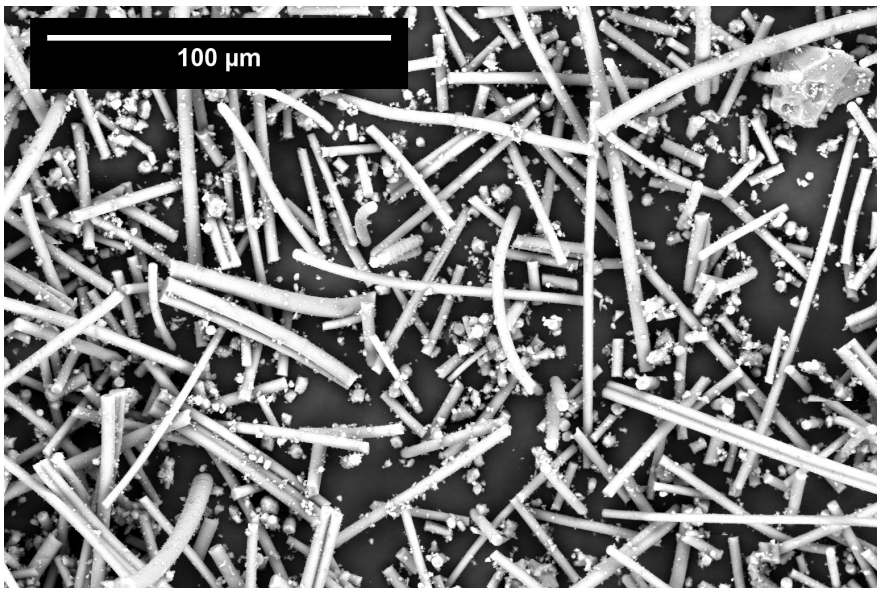

Fig. 4.7 BSE micrograph of the Saffil fibre after milling for 5 mins.

Chapter 5

Comparison of PEO Processing Characteristics of Al, Mg and Ti

This chapter provides a comparison of the processing characteristics of the three most widely-used substrates for PEO processing; Al, Mg and Ti. It has long been recognised that the processing of Ti in particular differs from the Al and Mg, but this has not been described in any great detail at the bulk level, let alone at the individual discharge level. Using the established synchronised electrical and high-speed video monitoring technique, together with conventional bulk processing measurements, the processing differences of the three metals will be correlated to the properties of their oxides.

5.1 Outline of Experiments

The experimental programme for this chapter can be split into two components. The first concerns the macroscopic characteristics of the PEO processing of the three metals. In §5.2.1,

plate samples of Al, Mg and Ti are processed continuously under a constant current condition of 20 A dm^{-2} RMS for a duration of 30 minutes. Under the constant current condition, the amplitude of the fixed frequency sinusoidal voltage was free to vary, in order to hold the RMS current constant. Secondly, a single sample of Mg and Al were each processed in 5 minute increments up to 60 minutes, and the mass of the single sample was measured initially and after each 5 minute treatment. For Ti, it was found that the rate of mass gain was actually negative after approximately 5 minutes, so it was necessary to use processing increments of 1 minute, up to a total of 5 minutes of processing, after which increments of 5 minutes were used until a processing time of 30 minutes was reached. In order to measure how the optical properties of the process vary with processing time, a camera (described in more detail in §4.3) was used to capture a recording of $\approx$ 500 ms half-way through each processing increment for each metal.

The second component of this chapter studies the processing of each metal at the individual discharge level. A small area sample of each metal was prepared (see §4.2.2) and processed under the same conditions as the bulk samples, and using the electrical and video monitoring set-up outlined in §4.5, syncronised optical and electrical small area data were collected at the same increments as for the bulk samples. The duration of the high speed camera recording was the limiting factor in setting the length of these captures, which was 307.762 ms. The interval between camera frames was 5.34 μs and the frame exposure was 4.61μs. The electrical monitoring system was able to run at a higher resolution, with an interval of 51.2 ns.

5.2 Macroscopic Characteristics

5.2.1 Coating Growth

Figure 5.1 shows the peak anodic and cathodic voltage over the course of processing of each metal. The shape of these voltage curves are typical of fixed current PEO processing, although differences can certainly be observed between the three substrates. Al is the most well-characterised substrate, and it has been well established that the form of the voltage response in Fig 5.1 is caused by the following processes:

- During the first 30 seconds or so (before discharges occur), conventional anodising takes place, as the electrolyte is in physical contact with the substrate through numerous pores in the native oxide coating. The voltage applied quickly rises to levels greater than those used in conventional anodising, so the rate of coating growth is fairly high at this point.
- The increase in thickness effectively raises the resistance of the oxide layer, causing the applied voltage to rise to generate the prescribed current density.
- Once the voltage rises above the dielectric breakdown voltage of the oxide, discharges begin to occur preferentially at sites of low dielectric strength.
- The voltage begins to stabilise as dielectric breakdown is now occurring across a thin barrier, the thickness of which does not vary (appreciably) with coating thickness.

It can be seen that the processing voltage of Al ramps up earlier in the process than with the other two substrates. Al is anodised quite widely and is known to have quite a high growth rate, so it is likely that the Al peak voltage stabilises earlier than the other metals because the critical coating thickness is reached faster than for Mg or Ti.

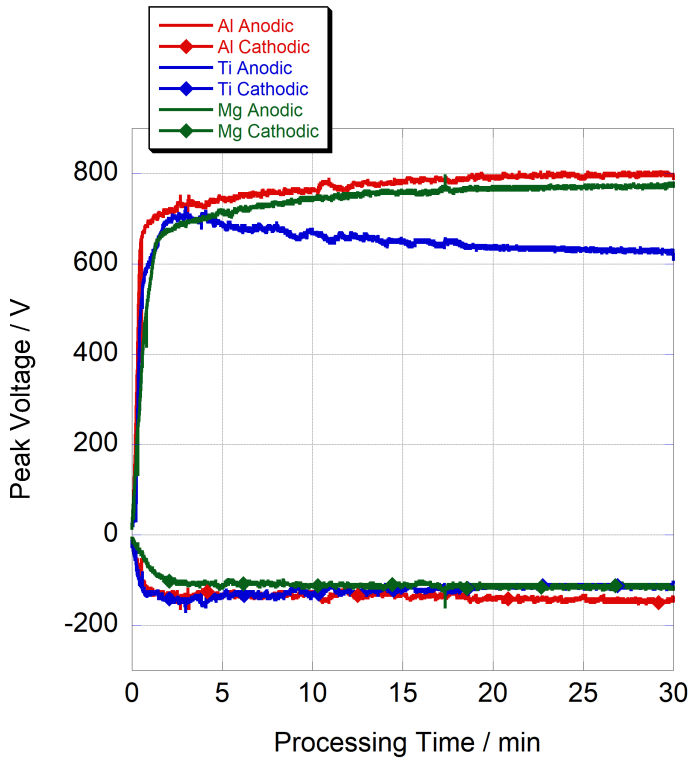

Fig. 5.1 Peak anodic and cathodic voltages during processing of Al, Mg and Ti at a fixed current density of 20 A dm^{-2}

The voltage required to cause dielectric breakdown of each metal is dictated by the dielectric strength. For Al this is in the range 15-20 kV mm^{-1}. An example of a discharge pore in the Al coating is given in Figure 5.2a, showing a thickness at the base of the pore of ≈ 5 μm. It should be noted that while this thickness value is not extremely accurate (the grinding and polishing technique usually deforms elements of the coating), it is generally accepted that the thickness at the base of a pore is around this value. This gives a lower bound of the dielectric breakdown voltage at this location of around 75 V (in reality, due to porosity and other defects, the real value may be slightly less than this). A similar exercise for the Mg pore in Figure 5.2b, using a base pore thickness of ≈ 10 μm and a lower bound of dielectric strength of 6 kV mm^{-1} gives a theoretical breakdown voltage of 60 V, and for the Ti pore in Figure 5.2d, with a pore base thickness of ≈ 3 μm and a dielectric strength of around 4 kV mm^{-1}, a breakdown voltage of around 12 V. These values are obviously much lower than what is generally applied by the power supply during processing, but it should be borne in mind that most of the voltage applied is dropped across the electrolyte tank. Nevertheless, since the conductivities of the electrolytes used were broadly similar (12.3 and 12.7 mS cm^{-1} for the Al and Mg/Ti electrolyte respectively) this calculation can be used to rank the three substrates in terms of their expected "steady state" processing voltage for a given current density.

Of course, it can be seen in Figure 5.1 that the peak voltages are not in fact steady state, but vary slightly over the course of processing. It is likely that this is linked to the coating thickness. Calculations can be made concerning the potential drop across a pore using electrolyte conductivity data. On the scale of the complete set-up, these are complicated by convection etc., but simple estimates can be made relating to the potential drop across a (stagnant) column of liquid within the pore above a discharge site. The variables involved, apart from electrolyte conductivity, σ, are the dimensions of the pore (depth L and diameter

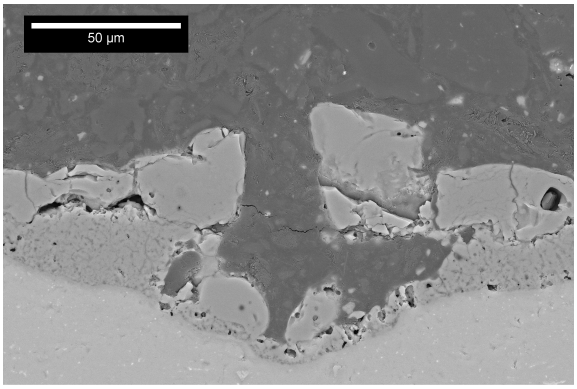

(a) Al discharge channel after 60 minutes of processing

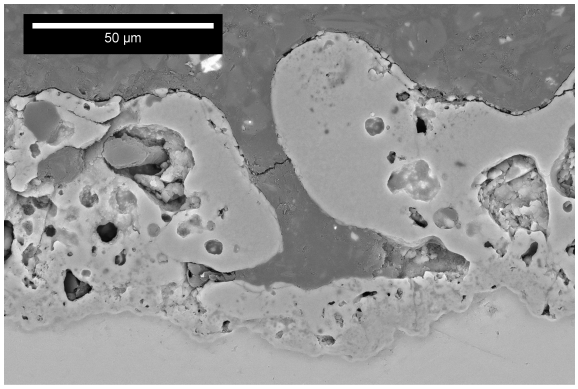

(b) Mg discharge channel after 60 minutes of processing

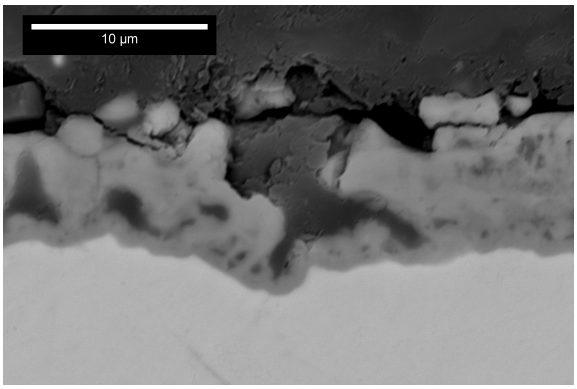

(c) Ti discharge channel after 2 minutes of processing

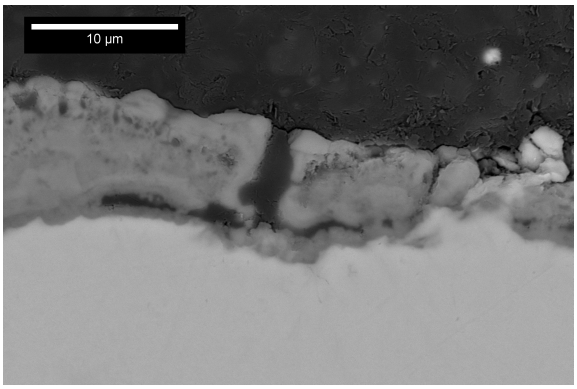

(d) Ti discharge channel after 30 minutes of processing

Fig. 5.2 BSE micrographs of discharge channels in coatings formed on the three metals

D) and the (discharge) current, I_{dis}. The voltage drop is then given by:

$$\Delta V = \frac{4LI_{dis}}{\pi D^2 \sigma} \tag{5.1}$$

From this equation, it can be seen how as the coating thickness (and therefore the pore depth, L) increases, as does the voltage drop across the electrolyte column within a discharge channel. Therefore, it is expected that the applied voltage will need to increase (slightly) with coating thickness. This is indeed what is seen during Al and Mg processing, but not during the processing of Ti, which experiences a reduction in applied voltage under prolonged processing. To understand this, it is helpful to consider the mass change of each metal during processing. The growth behaviour of Al and Mg has been well characterised in the literature in terms of coating thickness growth. This is typically measured using an eddy current gauge or by examination of a polished cross-section, both of which, as discussed, are not terribly accurate portrayals of how coating growth is progressing. Figure 5.3 shows the bulk mass gain of a single sample of each substrate processed in discrete steps, with thorough washing, drying and weighing between steps. This gives a clearer image of what is actually occurring during processing. It can be seen that the mass gain increases linearly with processing time for Al and Mg, agreeing well with established work that coating thickness also increases linearly with time for these two metals. Ti clearly behaves quite differently to these two; mass gain is linear for only 2 minutes or so, before reducing and becoming linearly negative. In this instance it is certainly relevant to consider the cross-sectional coating thickness. A cross section showing a discharge channel for the coating after 2 minutes of processing is given in Figure 5.2c, and it can be seen that the thickness of the coating has barely changed after the subsequent 28 minutes of processing (see Figure 5.2d). This shows that the thickness actually reaches a peak after 2-3 minutes, and subsequent discharges cause a net loss of mass from the coating (i.e. the substrate is consumed). It is not immediately clear why Ti shows

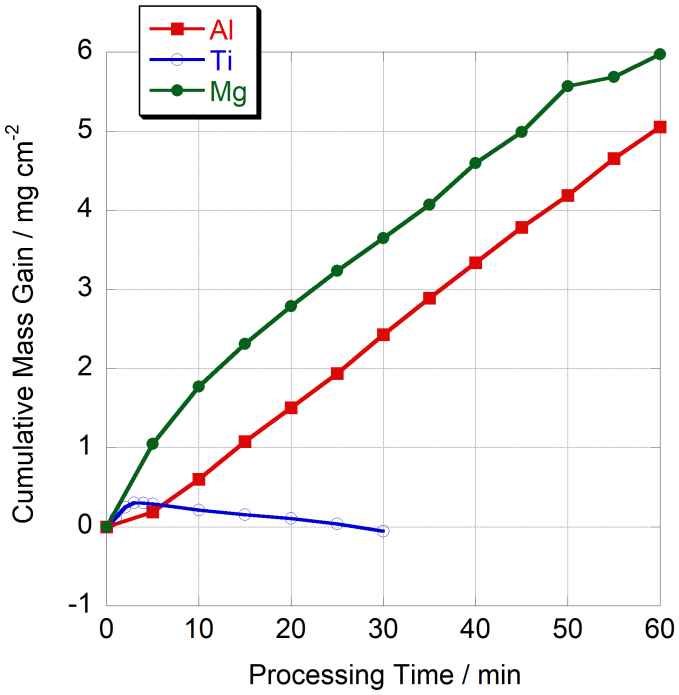

Fig. 5.3 The cumulative mass gain (normalised for processing area) of a single sample of each substrate, processed in 5 minute steps up to 60 minutes for Al and Mg, and processed in 1 minute steps up to 5 minutes, and in 5 minute steps thereafter up to 30 minutes for Ti.

this limit on coating thickness, but it should be noted that in industry, thicker coatings can be produced by using higher concentrations of phosphates, silicates or aluminates in the electrolyte to form a deposition-based coating containing elements from the electrolyte. The current work is limited to those coatings composed of predominantly the substrate oxide.

5.2.2 Optical Characteristics

Measurement of the bulk optical response of substrates undergoing PEO processing has often been used in earlier works as an indication of the intensity and distribution of discharges. Figure 5.4 contains various images which are composed of around 500 ms of video frames superimposed onto each other at various points throughout processing, to provide a 500 ms history of the discharges that occurred on the portion of the sample in view. After 30 seconds,

diffuse discharges can be seen on the Al sample, and some extremely faint ones on the Mg, but the Ti sample shows none. This correlates with the recorded voltage trace, that Al ramps the quickest and must therefore reach discharging conditions before the other two metals. The discharge pattern shown in these images is typical of what has been reported in the literature for Al and Mg, that discharges begin diffuse and become more spatially sparse and intense as processing continues. On the other hand, there is a distinct lack sustained large discharge sites on the Ti substrate after 30 minutes of processing. The 'edge' effect can be seen on the Ti sample, where discharges tend to be concentrated at the sample edge, due to electric field effects. There is no evidence to suggest that these discharges are unconventional in nature, but they are clearly not contributing to thickening of the coating. It may be that the newly formed oxide (formed from the collapse of these discharges) is not attaching to the existing coating, or that more previously formed oxide is detached by the new discharge than new oxide created. There does seem to be a tendency with Ti substrates for some of the coating to be ejected into the electrolyte, often visible as accumulating suspended particles in the electrolyte.

5.2.3 Macroscopic Energy Consumption

The macroscopic energy absorption in this context is defined as the amount of total electrical energy used to form the coating divided by the normalised mass of coating produced (coating thickness multiplied by free surface area). This data is shown in Figure 5.5.

The amount of energy consumed was found by multiplying the average root mean square (RMS) current and voltage to obtain the RMS power for each run, and this was multiplied by the process time to give total electrical energy. As the mass gain was fairly linear with processing time for Al and Mg, the mass gain (and injected electrical energy) was taken after 60 minutes of processing, and for Ti after 3 minutes. 3 minutes was chosen for Ti as it

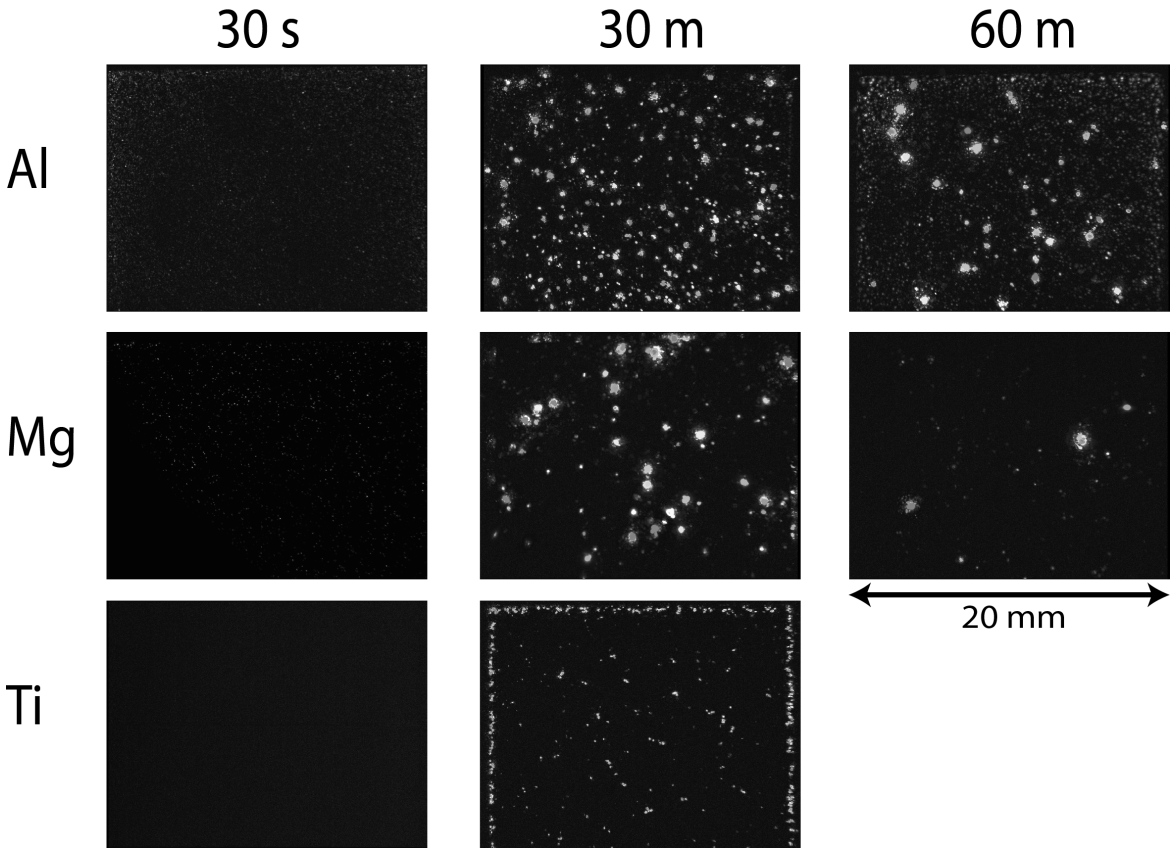

Fig. 5.4 A set of images showing the discharge distribution for each metal at various stages of processing. Each is the result of superimposing 2500 frames from a video lasting 500 ms (i.e. a 200 μs interval between frames). The video was started at the time stated in the figure.

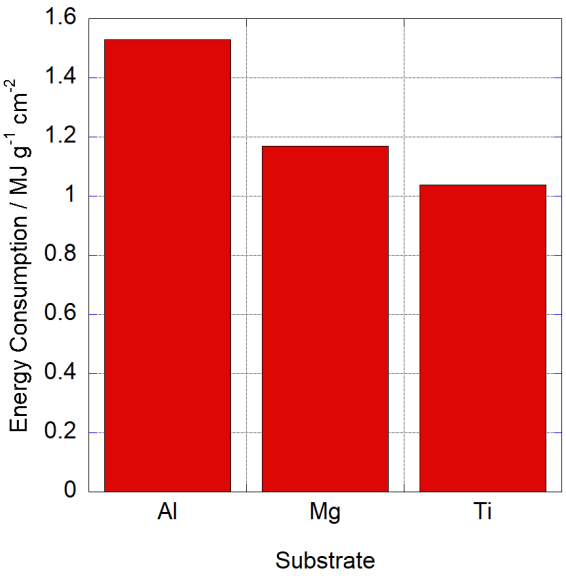

Fig. 5.5 Specific energy consumption for PEO processing of Al and Mg for 60 minutes, and Ti for 3 minutes.

represents the maximum mass gain of the sample throughout the 30 minutes of processing, and the end of the brief linear region of mass gain at the start of processing. If a longer process duration were to be considered, the specific energy consumption would approach infinite as the mass gain approaches zero. Therefore, the figures presented in Figure 5.5 are a good representation of the inherent energy consumption of the underlying processes which result in productive coating formation for each of the three substrates. As the current density imposed for the three substrates was identical, the energy consumed was dependent solely on the voltage generated by the power supply. As discussed in §5.2.1, Al and Mg process at a similar voltage, with Ti considerably lower.

5.3 Small Area Baseline Voltage and Current

As discussed in §2.4.1, an asymmetry is seen in PEO processing, in that the vast majority of discharges occur during the anodic part of the cycle. Current does flow during the

cathodic part albeit at a lower voltage, implying the barrier for charge transfer is lower in the substrate $\rightarrow$ oxide $\rightarrow$ electrolyte direction than vice versa. The behaviour of current flow through the oxide in the absence of discharges is relevant to the overall energy consumption of the process, as under the current theoretical framework, oxidation (and therefore coating growth) can only occur through discharging (apart from the brief anodising stage at the beginning of processing). In this context, current passively flowing through the oxide could be viewed as a source of wasted energy. A complete voltage cycle, with associated small area current, for all three substrates at 30 seconds and 30 minutes into processing is shown in 5.6. For each substrate, the cathodic voltage is higher later in the process than earlier. This is attributed to the effect described in Figure §5.2.1, that the voltage drop across a column of electrolyte increases as the depth of the column (i.e. coating thickness) increases. This effect is less pronounced for the Ti substrate; which is consistent with the observation that the Ti coating thickness does not change dramatically thoughout processing. For Al and Mg, the cathodic voltage increases in magnitude as the process progresses. It is generally accepted in the literature that hydrogen is generated at the cathode, due to the transport of H^+ ions through the coating, which combine with electrons at the interface to form the gas. Ionic transport is more difficult when the coating is thicker, so it is unsurprising that the cathodic voltage increases with time in this way for Al and Mg. On the other hand, the Ti cathodic voltage remains fairly constant throughout the process, and this again is consistent with the fact that the Ti coating thickness is not changing with time.

While there is some baseline current 'leakage' with Al and Mg later in the process, there is a dramatic increase in the baseline current for Ti in the 30 minute current trace. This current surge was not associated with optical emissions of any sort. Speculatively, these current surges could be due to some kind of charge capacitive phenomenon, with the potential for complex (out of phase) effects in view of the short timescales involved. It is perhaps worth noting in this context that the dielectric constant (reflecting the capacity to store charge)

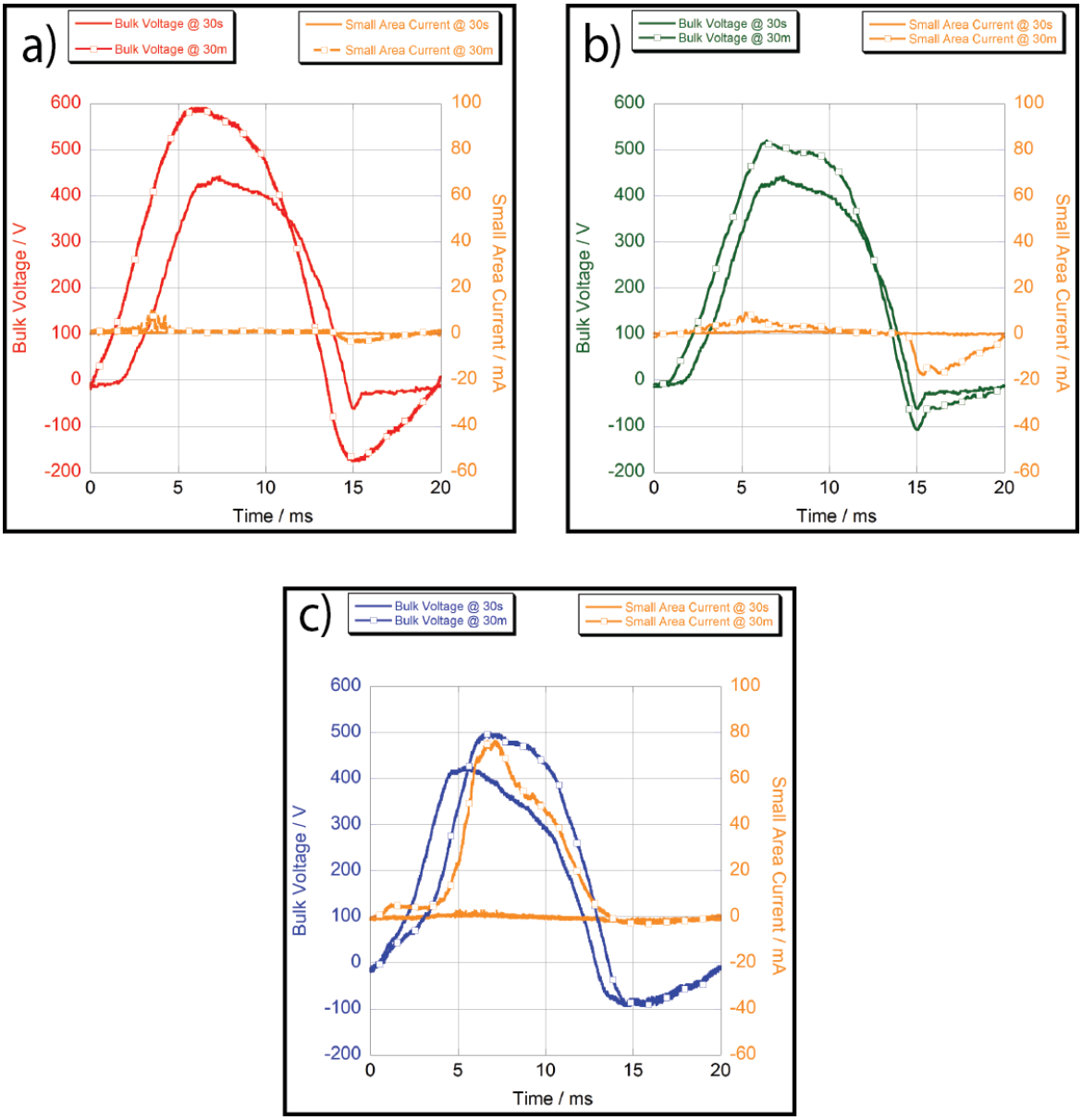

Fig. 5.6 A complete voltage cycle showing small area current for a cycle containing no discharges during processing of a) Al, b) Mg and c) Ti at 30 seconds and 30 minutes into processing.

of TiO_2 is much higher than that of most other oxides. This could certainly play a part in decreasing the rate of charge build up at the oxide/substrate interface and inhibiting the generation of high-energy discharges on Ti.

5.4 Discharge Characteristics

5.4.1 Discharge Current and Duration

Using the synchronised small area current and high-speed video monitoring method outlined in §4.5, data showing typical discharge sequences for the three main candidate substrates for PEO processing (Al, Mg and Ti) were captured and characterised. It is perhaps useful at this point to recap the currently accepted sequence of events that occur during a PEO discharge:

- Dielectric breakdown of a thin (micrometer-scale) oxide layer at the base of an electrolyte-filled pore
- Current rises as plasma expands, incorporating elements from the substrate, oxide and electrolyte. The local high temperature generates a relatively large vapour bubble.
- Current shuts off as the growing bubble increases electrical resistance.
- New oxide material is formed as plasma collapses, and is ejected out of the pore and injected into interconnected pockets of porosity.
- Pore refills with electrolyte.

For Al and Mg, there were several well-defined discharges detected during the anodic part of each cycle, which appeared to coincide with the voltage rising past $\approx$ 500 V. An

example of a typical anodic cycle for Al is shown in 5.7a and for Mg in 5.7b. The small current fluctuations seen early in the cycle for both metals did not coincide any detectable optical emission. For these half-cycles, the first optical emission came at approximately 6.1 ms for Al, and 4.5 ms for Mg. Current also flowed during the cathodic part, although the voltage only reached about 100 V for both metals.

Ti, however, showed significantly different characteristics. Discharges did occur during the anodic part of the cycle, but there were more of them and their discharge currents were smaller. This information is shown in Figure 5.7c and at higher resolution in Figure 5.7d. Optical emissions associated with individual discharges were detectable for Ti, but they were short-lived ($\approx$10 μs) and weak. In fact, for Ti, it could be seen optically that more than one discharge cascade often occurred at the same time on the small area sample: this means that the intervals between individual discharges cannot reliably be inferred from these plots, although the current associated with them should still be correct. Also, the proportion of the total anodic current being carried by discharges was clearly smaller than for Al and Mg. Furthermore, the anodic voltage developed ($\approx$500 V at the peak) was somewhat lower than for Al and Mg. These observations are consistent with the idea that electron flow through the oxide layer was taking place more readily with Ti, inhibiting the development of high electric fields across the oxide and hence of large, well-defined discharges.

5.4.2 Cascading

Troughton et al [77] were the first to study the so-called 'cascading' behaviour of discharges on Al. This work confirmed the tendency for discharges to occur repeatedly at the same location, with a relatively regular interval between events. It is fairly well-established that these cascades initiate at the base of a discharge pore, such as those shown in Figure 5.2, where discharges will repeatedly occur and thicken the coating locally until the local electrical

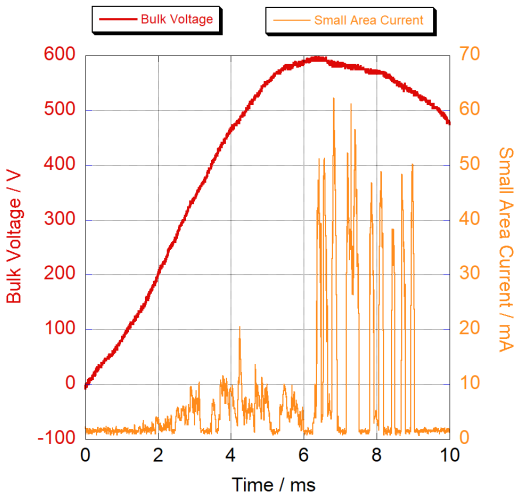

(a) Voltage and small area current data showing typical discharges during processing of Al. The coating is approximately 30μm thick at this stage.

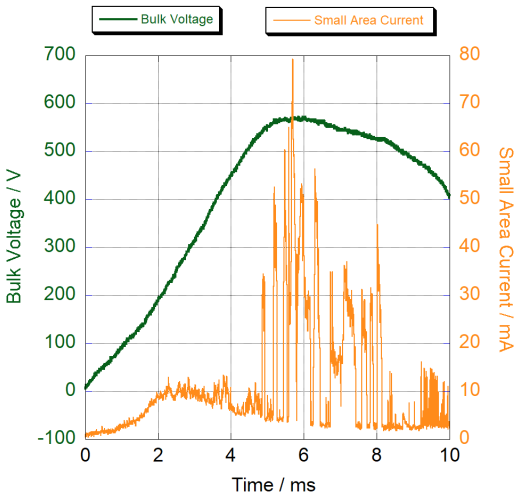

(b) Voltage and small area current data showing typical discharges during processing of Mg. The coating is approximately 30μm thick at this stage.

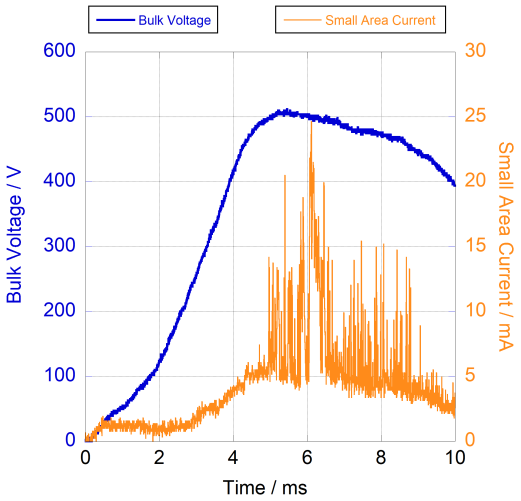

(c) Voltage and small area current data showing typical discharges during processing of Ti. The coating is approximately 5μm thick at this stage.

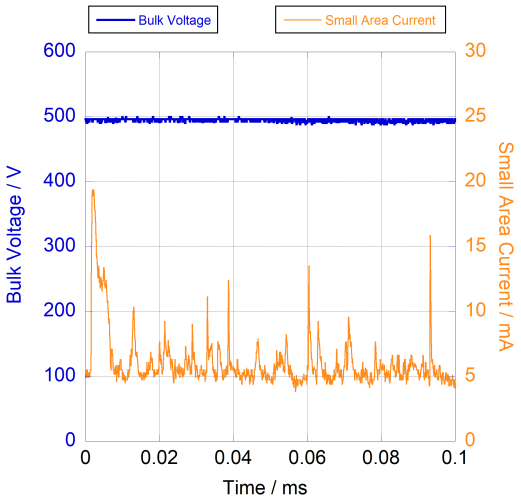

(d) A higher resolution plot of the data in c), starting at a time corresponding to 6.1 ms in that graph. This corresponds to the first optically detectable discharge in that cycle.

Fig. 5.7 Synchronised bulk voltage and small area current data showing typical discharge behaviour for the three substrates

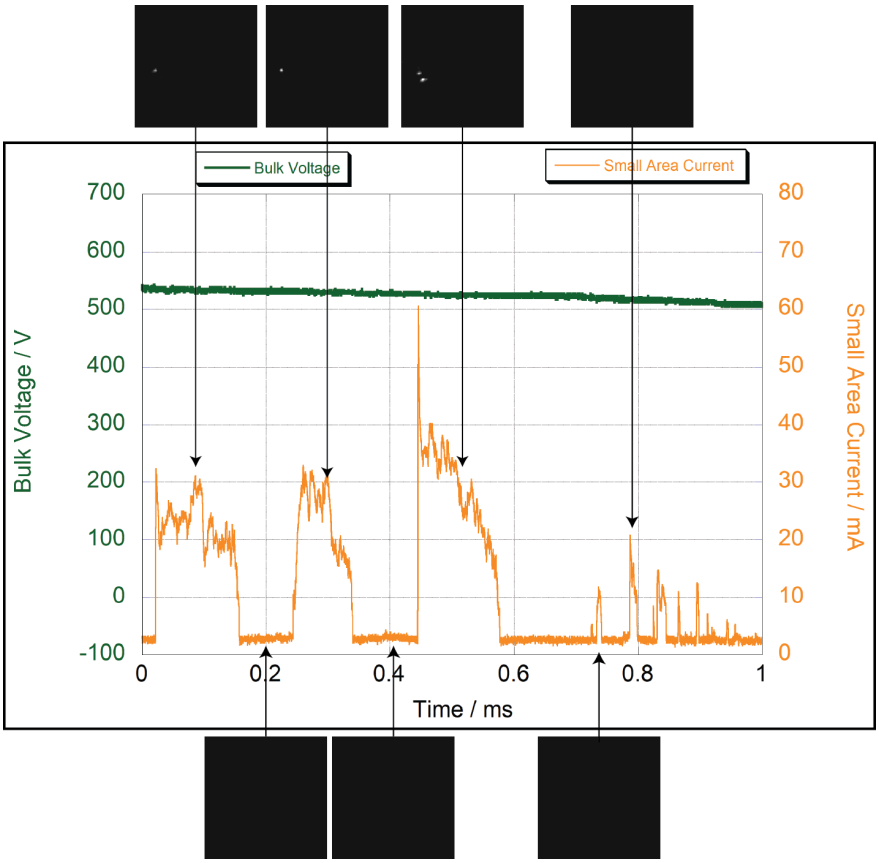

Fig. 5.8 Synchronised small area electrical and optical data showing a cascade during PEO processing of Mg. Each image shown was captured with an exposure of 4.61 μs. This set of discharges is a higher resolution plot of a sequence of discharges shown in Figure 5.7b, starting at 7 ms.

resistance is raised to a level where discharges will preferentially occur at a different, less resistant site. This behaviour has previously been recorded for processing on Al substrates only, but cascades were recorded for all three substrates in this study. Synchronised small area current and optical data showing a cascade during processing of Mg is shown in Figure 5.8. The three distinct discharges (i.e. between 0 and 0.6 ms) were similar to those captured on Al substrates, with peak currents of around 40-50 mA, durations of 100-200 μs with an interval between discharges of 50-100 μs. It is likely that this time period represents the time taken for the discharge pore to refill with electrolyte.

Ti, as discussed, presented a difficulty in inferring discharge characteristics from the small area current data, as it was recorded optically that two discharges often existed at the same time on the small area sample. Therefore inter-discharge durations cannot be inferred from the current traces. Synchronised current and optical data for Ti are presented in Figure 5.9. It can be seen that the optical intensity of the discharges seen in images **1**, **3** and **7** is considerably lower than those recorded on Al or Mg, and two separate discharge sites are active. The largest discharge in this sequence is the first, with a peak current of ≈ 20 mA and a duration of ≈ 5 μs. These values can be quoted with relative confidence as it can be seen that only one discharge site is active. A different discharge site is then (faintly) visible in image **3**, and the same site is active again in image **7**. This cascading behaviour was seen regularly during processing of Ti.

5.5 Discharge Energies

The energy of a discharge can be calculated by integrating the power (product of discharge current and initiation voltage) of a discharge over the temporal duration of the event. The energetics of Al discharges have been fairly well established, with discharge currents typically several tens of mA and initiating at a voltage (in the main stage of processing, after ≈ 5 minutes) of 700-800 V, leading to discharge energies in the region of a few mJ. It has been shown in the present work that discharges on Mg substrates are of similar energy, although optical evidence (see §5.2.2) suggests that the amount of discharges occurring at any point in time is lower for Mg. Ti discharges however, appear to have energies of an order of magnitude lower than the other two substrates (with discharge currents of the order of 10 mA, durations of $\approx 10\mu$s and an initiating voltage about 100 V below that of Mg and Al. Of course, absolute energy figures are very approximate and the parameters concerned

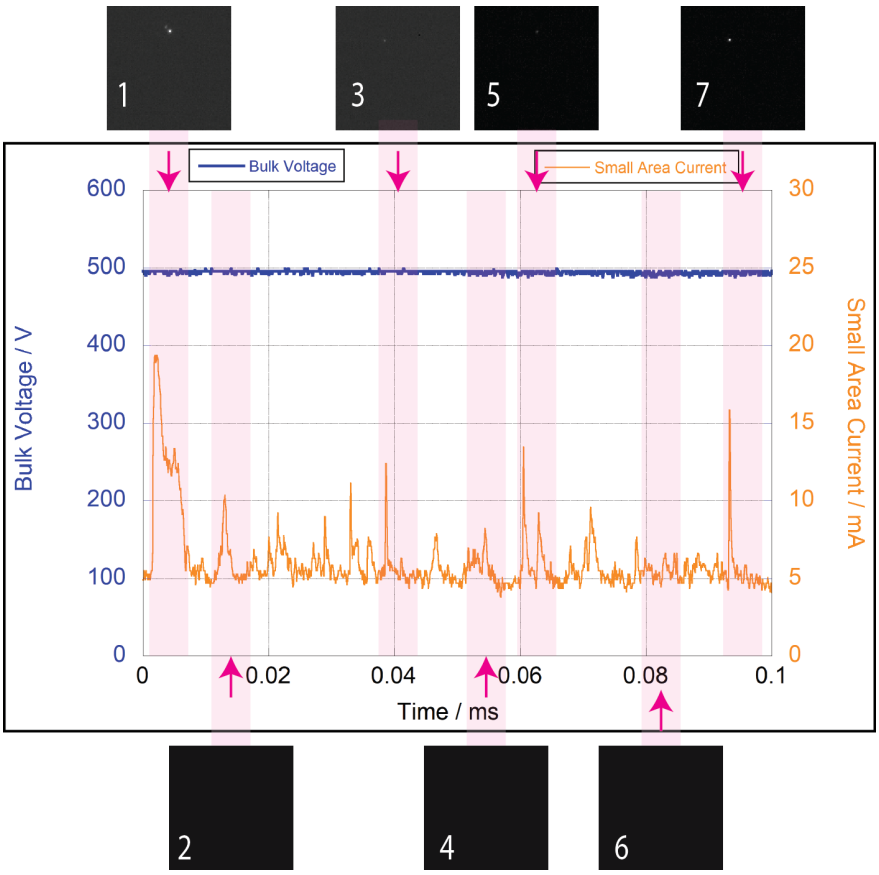

Fig. 5.9 Synchronised small area electrical and optical data showing a sequence of discharges during PEO processing of Ti. Each image shown was captured with an exposure of 4.61 μs, and the shaded pink regions indicate the time period that each image corresponds to. This set of discharges is the same set as were plotted in Figure 5.7d.

(discharge current and duration) are far from uniform. It is clear, however, that Ti discharges have a substantially lower energy associated with them than Al or Mg.

5.6 Oxide Properties and Energy Consumption

The concept of an "energy efficiency" of a PEO process is not a well-defined one, given that the desired outcome, i.e. oxidation of the substrate, will release energy rather than consume it. For this reason, it is generally more simple to consider the electrical energy input per unit mass of coating produced. As observed in §5.6, however, not all current is carried in the form of discharges. This baseline current represents wasted charge, that is not contributing to coating growth. This wasted electrical energy is difficult to quantify for two reasons. The first is that the baseline current density is difficult to measure. The surface area of the small area sample is hard to calculate, given that the resin used does not give a perfect seal, and some ingress did occur. It can be seen that some of the mounted wire ($\approx$ 2.5 mm) has been processed, effectively meaning the small area sample should be treated as a small cylinder rather than a circular plane. The second is that because the voltages involved in the process is so large and the sample area is small, the effective electric field is relatively higher for the small area sample due to convergent electric field lines. This tends to increase the current flowing through the small area sample. For example, taking the baseline current of 80 mA seen in Figure 5.6(c), this represents a baseline current density of over 1000 A dm^{-2} if it is assumed that only the face of the small area wire is carrying current. Clearly, this is not physical, and if the extra processed area is accounted for, the figure reduces to a more reasonable 100 A dm^{-2} (while this is much higher than the set current density, it is common for local current densities in the vicinity of a sharp 'edge' to be this high).

Despite this difficulty, the importance of the baseline current with regards to energy consumption can be demonstrated using a simple procedure. The RMS of a set of small area current data spanning 0.5 seconds where there were no discharges was calculated, and divided by the RMS of a 0.5 second section of data from the same experimental run where discharges occurred on every anodic half cycle. This gives the fraction of current carried by the baseline over discharges, while accounting for 'small area' effects, which should affect both sets of data equally. The baseline was estimated to account for 12% of the overall current density for Mg, 37% for Al and 70% for Ti. These baseline current effects can be explained by the band gap values of each oxide. TiO, as shown in Figure 2.6, has a considerably lower band gap than the other two oxides, while MgO has the highest. The aim during PEO processing is to cause dielectric breakdown of the coating, therefore it is preferential for the coating to be insulating. An oxide with a low band gap will conduct more current through the coating than one with a higher band gap, without breakdown, and will therefore waste energy and not contribute to coating growth.

While appearing decidedly inefficient in that regard, Ti was calculated to have the lowest specific energy consumption of the three substrates (see Figure 5.5) in the linear growth region. The main factor in this low energy consumption value is the low applied voltage necessary to sustain discharges on Ti substrates. This is possible due to the low dielectric strength of TiO_2, compared to the other two substrates, as discussed in §5.2.1.

5.7 Summary

This chapter has presented a comparison of the processing characteristics of the three most common substrates used in PEO: Al, Mg and Ti. By processing each substrate under identical electrical conditions (and electrolytes with very similar pH and conductivity values),

properties such as mass gain rate, electrical response and energy consumption rates can be meaningfully compared. Ti has shown substantially different processing behaviour to the other two substrates. In terms of macroscopic properties, the initial voltage ramp at the start of processing was similar for all three metals, but for Ti, this levelled off around 150-200 V lower than the other two, and actually began to decline slightly. This was reflected by a decline in the mass of the sample when processed for longer than ≈ 5 minutes, while the coating thickness remained constant. While the sample was losing mass later in the process, it was shown that discharges were still forming as normal, but were much less electrically and optically intense than those recorded on Al or Mg.

In the linear growth region, Ti appeared to consume the least amount of energy per unit mass of coating, primarily due to the lower applied voltage necessary to initiate discharges. This has been linked to the low band gap of titania, which allows electrons to move comparatively freely through the oxide interface between electrolyte and substrate, preventing the build-up of an electric field large enough to cause energetic discharges. After a certain coating thickness is reached however, these small discharges are no longer energetic enough to cause further coating growth and actually negatively affect coating growth.

The phenomenon of discharge cascading, i.e. the tendency of dielectric breakdown to occur repeatedly at the same region, has previously been shown to occur on Al substrates, however, in the present work the cascading phenomenon has been shown to also occur on Mg and Ti substrates. This reinforces the idea that the fundamental mechanisms at play during a discharge are very similar, if not identical, for all three substrates.

Chapter 6

Incorporation of Small Particles Suspended in the Electrolyte

PEO processing for light metals is known for decades and has been established as a well-known industrial surface treatment offering a reasonable wear and corrosion resistance. However, long-term protection is compromised by the intrinsic porosity and limited range of composition of such coatings. There has been considerable recent interest in the concept of particle addition to the electrolyte, aiming at their eventual incorporation into the coatings during processing. The idea is that with the help of particles the defects can be sealed, and the composition range and the functionalities of produced coatings can be enhanced. In this study, a mechanism for the inclusion of small oxide particles will be proposed.

6.1 Outline of Experiments

The three powders used in this investigation were:

1) 30 μm diameter Al_2O_3 powder, supplied by Alcoa,

2) 7 μm diameter MgO powder, supplied by American Elements; and

3) 100 nm diameter Al_2O_3, supplied by Alpha Aesar.

These were characterised according to the methods described in §4.8 and the size distribution of each batch of particles was consistent with the size designations of the suppliers.

All processing was carried out using a 10kW supply, with a constant current density setting of 20 A dm^{-2}. Two substrate types were used; CP Grade 1 Ti sheet and 1050 Al sheet, both of thickness 1 mm. All samples were rectangular in shape, with dimensions corresponding to those of the plate sample shown in 4.1(a).

Different samples (with the same dimensions) were processed for times of 2, 30 and 60 min for Al and 2, 15 and 30 min for Ti. Samples were weighed before processing, and after processing were flushed with de-ionized water, ultrasonically cleaned in acetone and then dried before being weighed again. Tests were run in electrolyte containing no particulate, and in electrolyte containing 1, 2 and 4 g L^{-1} of each powder.

6.2 Incorporation of Suspended Particulate

Figure 6.1 shows the measured changes in mass, for different processing times and particle concentrations, on both Al and Ti substrates. It can be seen that similar trends are observed for both substrates in terms of the effect of the presence of the particulate, although the rates of mass gain are lower for the Ti. In fact, it can be seen that, in the absence of particulate, there is actually a mass loss for the Ti, even though a (predominantly TiO_2) coating is being formed. The explanation for this is that there is a tendency with Ti substrates for some of the

coating to be ejected into the electrolyte, often visible as accumulating suspended particles. This is consistent with reports in the literature [48].

These mass changes have been normalized (divided by the surface area of the samples). It may first be noted that a baseline for interpreting these values can be obtained by converting them to coating thickness values, assuming that the process involves only oxidation of the substrate (and that none of the coating is lost into the electrolyte). The specific mass gain can be written:

$$\Delta m = H(1-p)\rho_{ox} - h\rho_{met} \tag{6.1}$$

where H is the coating thickness (with porosity level p), h is the thickness of metal substrate consumed and ρ_ox, ρ_met are the densities of oxide coating (pore-free) and metal respectively. There is also a relationship between h and H, based on conserving metal atoms. For example, in the case of Al (being converted to Al_2O_3), this is:

$$\left(\frac{H}{h}\right) = \frac{(2M_{Al}+3M_O)}{2M_{Al}} . \frac{\rho_{Al}}{\rho_{Al_2O_3}} \tag{6.2}$$

where M_{Al} and M_O are atomic masses. This allows a value of Δm to be converted to a value of H, provided the porosity level in the coating is known. Using these equations, and assuming a value of 20%for the porosity [2], the factor by which Δm (in mg cm^{-2}) needs to be multiplied in order to obtain H (in μm) is thus about 9.2 for Al, while the corresponding figure for Ti is about 11.9. For example, the Δm value of about 6.5 mg cm^-2 seen in Figure 6.1(b) for Al after 60 min of processing, with no particulate, corresponds to a thickness of about 60 μm. This is broadly consistent with what is observed (in Figure 6.2 (a). This

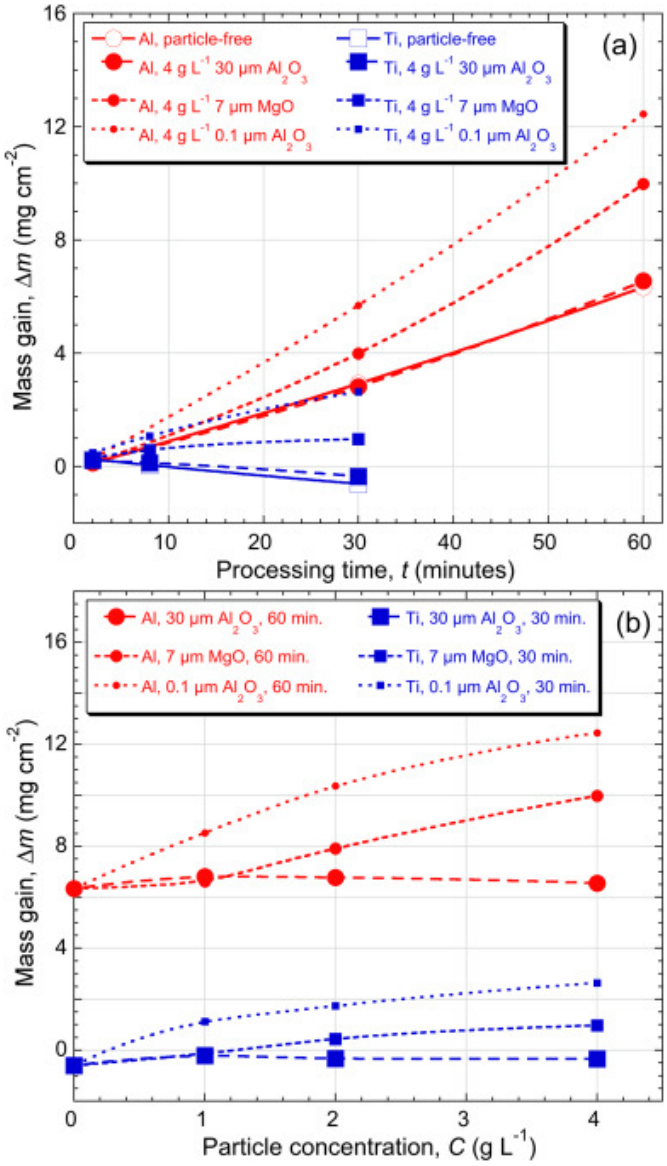

Fig. 6.1 Mass gain data, showing specific mass changes for both Al and Ti substrates, (a) as a function of processing time, for a particle concentration of 4 g L^{-1}, and (b) as a function of particle concentration, for processing times of 60 min (Al) and 30 min (Ti).

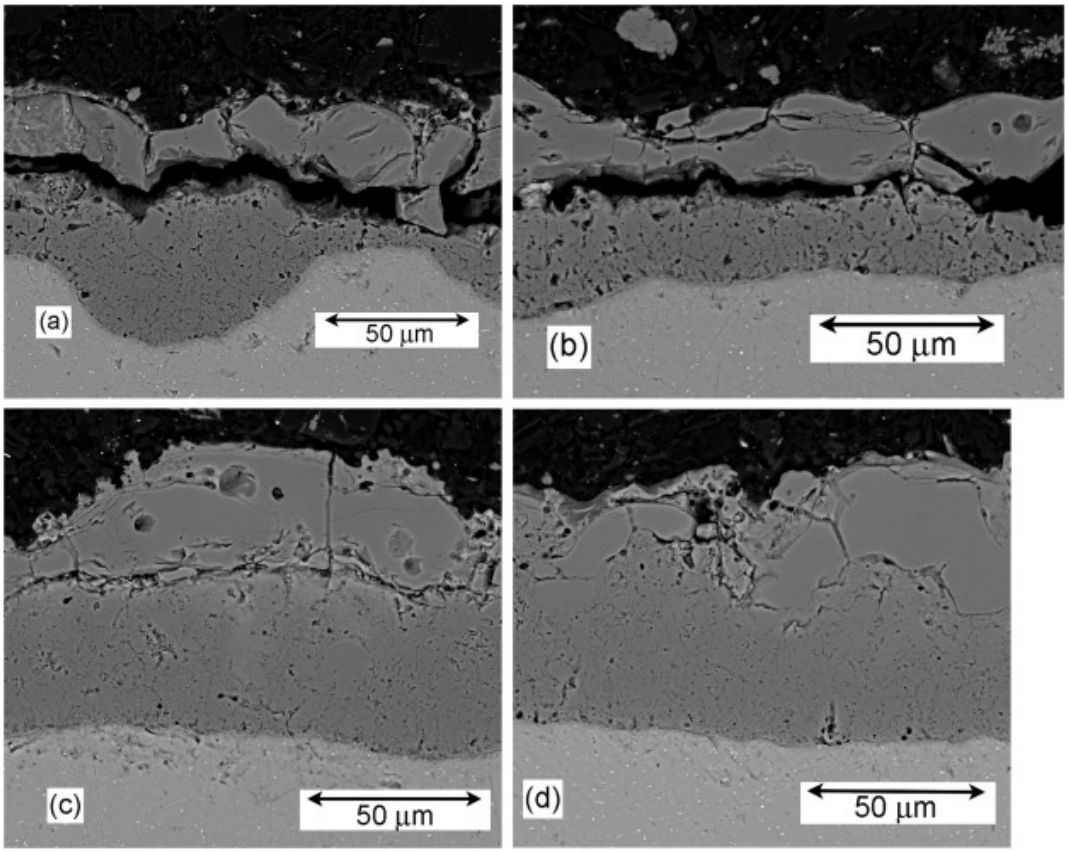

Fig. 6.2 SEM images of polished cross-sections of Al substrates, after processing for 60 min, with (a) no particulate, and with 4 g L^{-1} levels of: (b) 30 μm Al_2O_3, (c) 7 μm MgO and (d) 0.1 μm Al_2O_3

treatment provides a basis for assessment of both losses and gains that a coating might exhibit (other than via substrate oxidation) during PEO processing.

If a similar level of substrate oxidation is assumed for particle-containing and particle-free electrolytes, then an approximate increase in coating thickness due to particle incorporation can be estimated. This is a slightly different calculation from the one above, since the mass gain is now a combination of capture of the oxygen reacting with the substrate to form the oxide and entrapment of suspended particulate. For the highest loading of Al_2O_3 nano-powder, processed for 60 min, the extra mass gain from the particulate is about 6 mg cm^{-2}. This corresponds to an expected thickness increase of about 20 μm, depending slightly on the assumed porosity level. This also is broadly consistent with Figure 6.2 (d).

Referring in more detail to the data in Fig. 3, it can be seen that, for both substrates, there is a clear dependence on the size of the suspended particulate. The presence of the "30 μm particles" has little or no effect on the mass gains and it seems clear that particles in this size range do not become incorporated into the coatings. For the "7 μm particles", there is a noticeable effect, with observed increases in mass gain for the Al of $\approx$ 30–50% of the values with no particles present. The increase is greater still for the "100 nm particles", with mass gains being raised by as much as 100%, particularly after longer processing times and with higher particle concentrations. With the Ti substrate, the mass gains cannot be expressed in this way, since there is no mass gain in the absence of particles, but it is still clear that their presence can lead to significant mass gains, with similar trends in terms of the effects of processing time and particulate concentrations.

6.3 Microstructure

6.3.1 Transverse Section Microscopy

These variations in coating mass were also apparent in the thicknesses observed in transverse sections, despite the difficulties in assessing thickness in this way, arising from local variations, polishing artefacts etc. This can be seen in Figure 6.2 above, which refers to Al samples processed for 60 min, with and without the highest loadings of the 3 types of particle. The coatings are thicker, and possibly more homogeneous, in the presence of the two finer types of powder, particularly the "nano-powder". (It may also be noted that effects of the type seen in Figure 6.2 (a) and (b), where a tendency is apparent for partial detachment via decohesion within the coatings, can commonly be attributed to damage arising during grinding and polishing operations.)

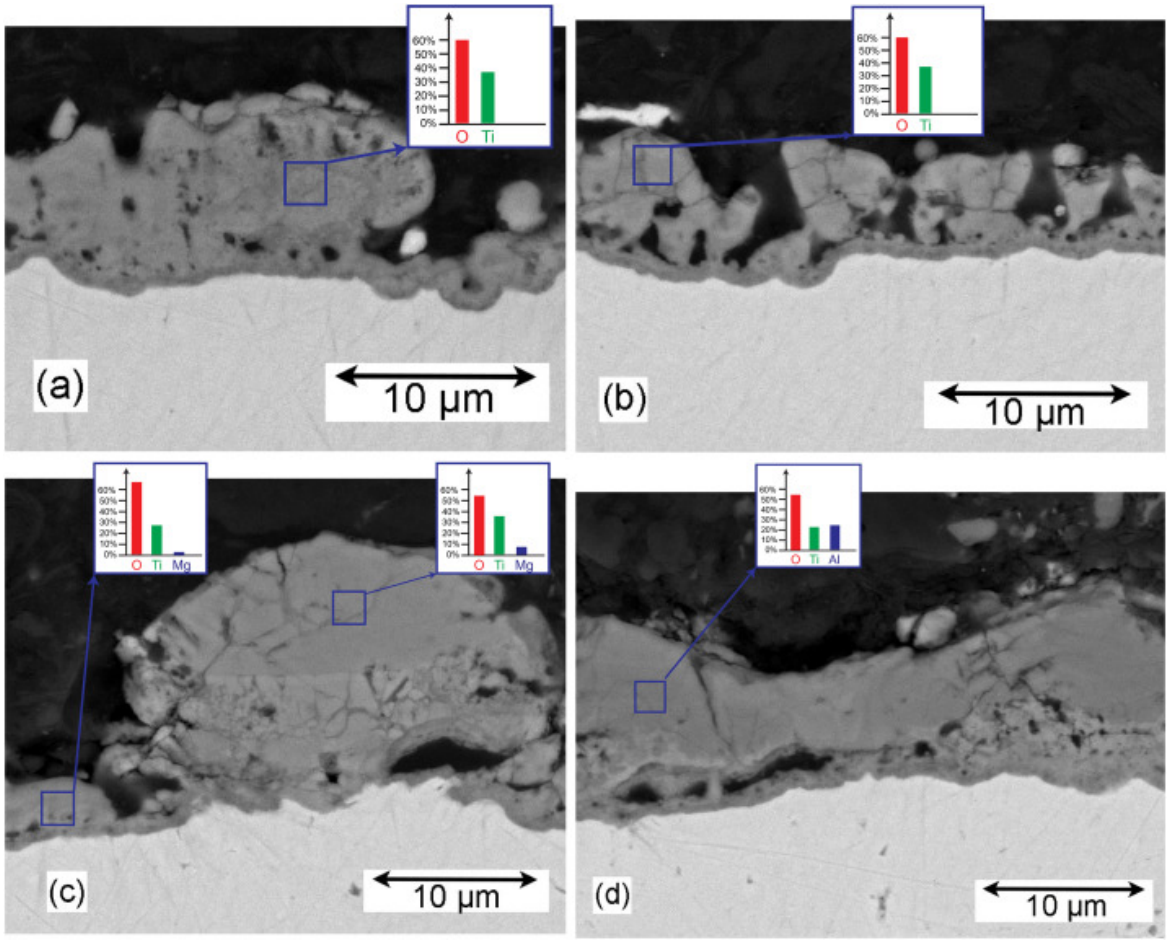

Fig. 6.3 SEM images of polished cross-sections of Ti substrates, after processing for 30 min, with EDX compositions of the regions indicated, with (a) no particulate, and with 4 g L^{-1} levels of: (b) 30 μm Al_2O_3, (c) 7 μm MgO and (d) 0.1 μm Al_2O_3.

Corresponding SEM micrographs are shown in Figure 6.3 for the Ti substrate, in this case after processing for 30 min. Similar trends to those seen for the Al substrate are observed in coating thickness, which is enhanced by the presence of the finer particles in the electrolyte. These micrographs also show the average compositions (in atomic %) of the regions indicated, obtained by EDX analysis. It can be seen that, with the 7 μm MgO powder and, particularly, for the alumina nano-powder, the coating compositions are relatively rich in Mg and Al respectively. This is clear evidence that these powders have become incorporated into the coatings, although they may have undergone phase changes in doing so.

It may be noted at this point that it is very difficult to identify incorporated particles in polished transverse sections. There are several reasons for this. One is that they are relatively small and their boundaries are likely to have been smeared during polishing. Another is that many of them were probably changed considerably during their entrapment in discharge sites and the subsequent plasma growth and collapse. They may well have been melted and re-solidified or vaporized and re-condensed during this process. They may even have become ionized in the plasma before some kind of re-formation took place as the plasma was quenched. Clearly, their size, shape and general appearance is likely to change dramatically during such transformations.

6.3.2 X-Ray Diffraction

An indication of the phase proportions in the coatings formed on the Al substrate can be obtained from the X-ray diffraction spectra shown in Figure 6.4, which relates to the longest processing time and the highest particulate loadings in the electrolyte. It is not a simple matter to unambiguously identify all of the peaks in these spectra, but in general it may be concluded that they probably all arise from α or γ Al_2O_3 phases. It should be noted that the intensities with truncated peaks correspond to substrate peaks. Because of the highly textured nature of the substrate, the peaks needed to be truncated to avoid saturating the spectra. The relative contributions from these two phases appear to be similar for both the particle-free electrolyte and the one containing the 30 μm particulate, which is consistent with there being little or no incorporation of suspended particles in the latter case. When the 100 nm particulate is present, however, there does appear to be a stronger contribution from the α phase in the spectrum. Since the original 100 nm powder was entirely α phase, this is consistent with a substantial proportion of the coating having been formed by incorporation of this material.

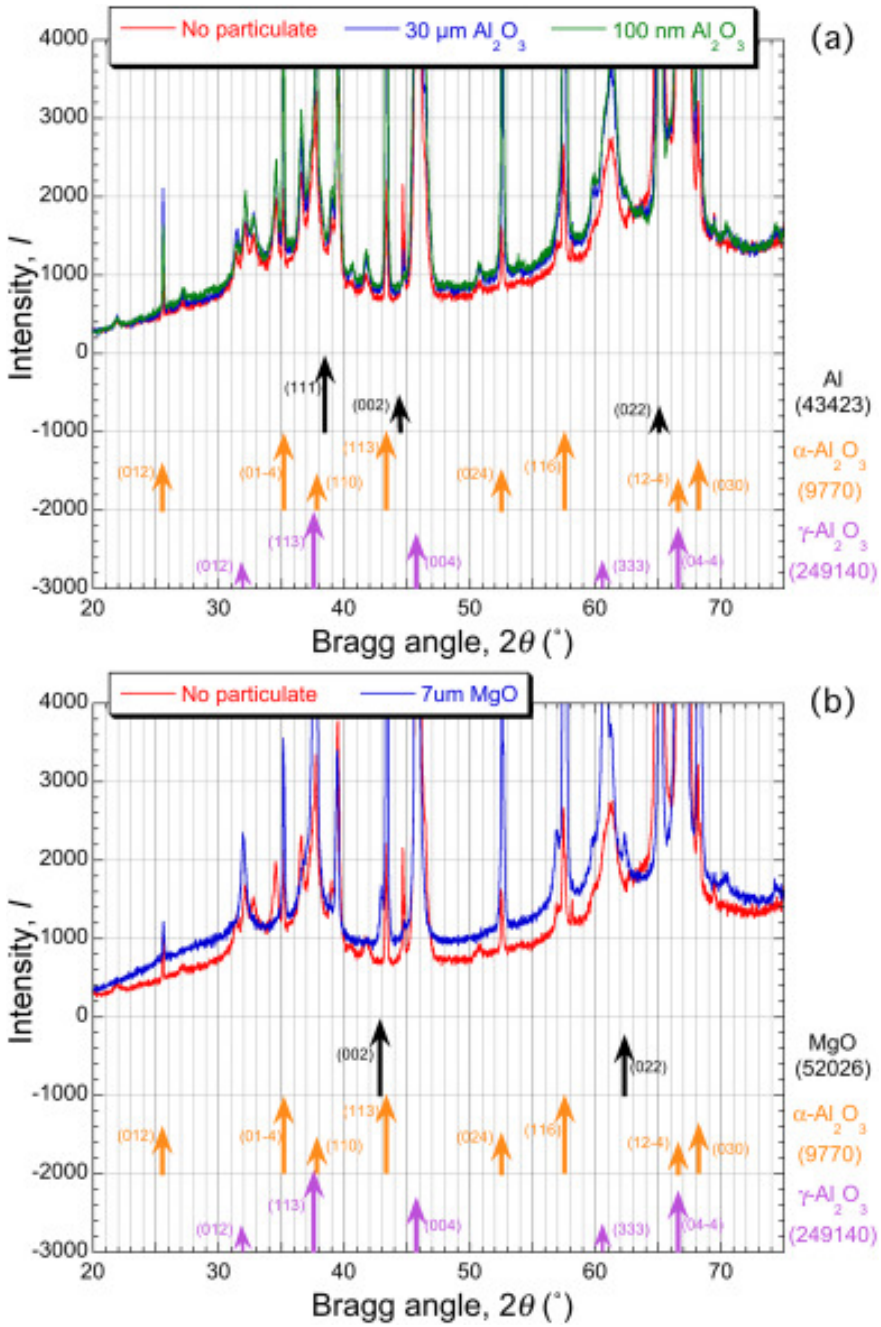

Fig. 6.4 X-Ray diffraction spectra from free surfaces of Al samples, after processing for 60 min, with the types of particulate shown (at a concentration of 4 g L^{-1}), for additions of: (a) Al_2O_3 and (b) MgO. The reference peaks shown are those with predicted relative intensities above about 15%.

The MgO powder offers the potential for rather clearer evidence concerning the origin of material in the coating. Referring to the set of reference peaks in Figure 6.4 (b), however, it can be seen that the MgO phase is not expected to provide many strong peaks that would be easy to differentiate from those due to the alumina phases being formed. However, a couple of peaks are present that probably are due to MgO, although they are not very prominent. This is consistent with the concept that there has been at least some incorporation.

Corresponding XRD spectra are shown in Figure 6.5 for the Ti substrate, after processing for 30 min. Figure 6.5 (a) shows the spectra without any particulate and with the highest loading of the 100 nm alumina. (The spectra from samples with the 30 μm alumina addition were indistinguishable from those with no addition.) The spectrum with no particulate mainly comprises anatase peaks, with a few from the rutile phase. The spectrum from the sample processed with the alumina nano-powder present is rather more complex, with relatively little from anatase or rutile, but a number of other peaks present. While it's difficult to unambiguously identify all of these peaks, at least the majority of them are from either α-Al_2O_3 or from aluminium titanate (Al_2TiO_5). This is, of course, consistent with substantial quantities of the suspended particles being incorporated into the coating, some of which react with Ti. This reaction presumably takes place during cooling of the plasma at the end of the discharge cycle. The Al_2TiO_5 phase is highly stable and is known to form quite readily when the elements concerned are all present. (In fact, it is commonly used [162] in Diesel Particulate Filters, which experience severe thermal and chemical environments.) Its formation does, of course, imply that the particulate has been exposed to high temperatures during the processing.

Fig 6.5 (b) compares the spectra with and without addition of the 7 μm MgO powder. It can be seen that the presence of the MgO does not in fact lead to any Periclase (MgO) peaks. However, there are several significant peaks from the magnesium titanate (Mg_2TiO_4) phase.

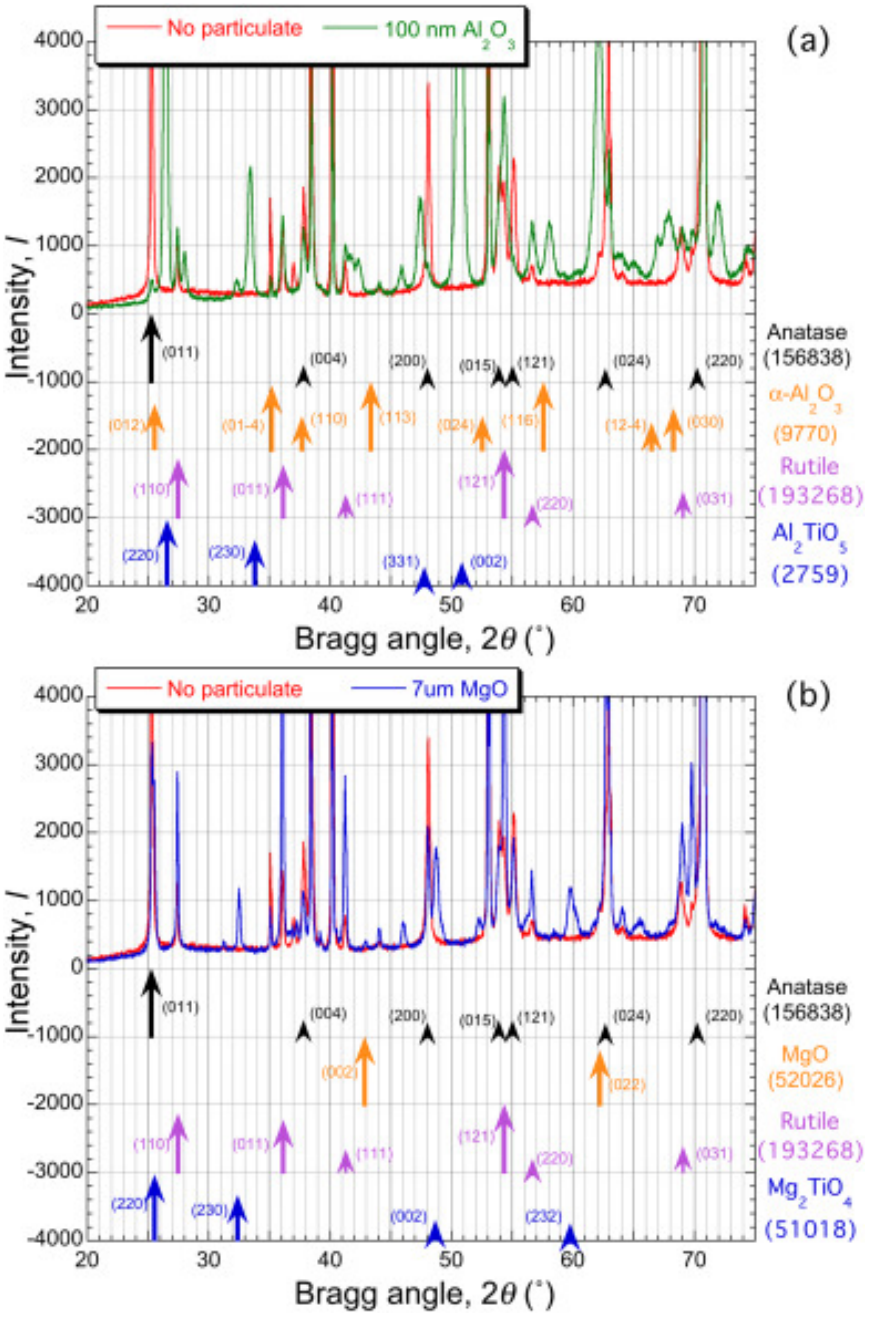

Fig. 6.5 X-Ray diffraction spectra from free surfaces of Ti samples, after processing for 30 min, with the types of particulate shown (at a concentration of 4 g L^{-1}), for additions of: (a) Al2O3 and (b) MgO. The reference peaks shown are those with predicted relative intensities above about 15%.

Again, this implies exposure to high temperature. It seems clear that in this case virtually all of the MgO absorbed into the coating has reacted to form this phase. Of course, there are clear indications (see Figure 6.1) that less of this type of particulate is incorporated into the coatings than is the case for the alumina nano-powder. It should be borne in mind that the sequence of events as the plasma starts to grow (with ingested particulate present in the electrolyte contained within the discharge site) is inevitably a complex and rapidly evolving one. Some of the particulate may be ejected into surrounding porosity, where it may undergo little or no change. Other particles, however, are likely to enter the plasma, where they will undergo rapid heating and probably at least melting, if not vaporisation and ionisation. They could subsequently solidify or condense into forms and phases that are quite different from the original. It is presumably more likely that particulate will be altered in this way if the plasma composition is such that phases can be formed that are thermodynamically more stable than that of the original particles. On the other hand, a high particulate content in the electrolyte probably makes it more difficult for it all to be transformed in this way, and also more likely that some will "escape" into surrounding porosity. This is consistent with virtually all of the MgO being converted to other phases, while some of the Al_2O_3 is retained in the α form.

6.3.3 Free Surface Morphology

Images of the free surfaces of these coatings, as shown in Fig. 8, are also potentially informative. For example, they give an indication of the diameters of the discharge pores, which are typically of the order of 10–30 μm in these cases. It's also sometimes possible to get an impression of how particulate might have deposited on the surface, although it should always be borne in mind that the view seen is that at the end of the process, after there has been time for particles to sediment in a way that might not have been possible during PEO

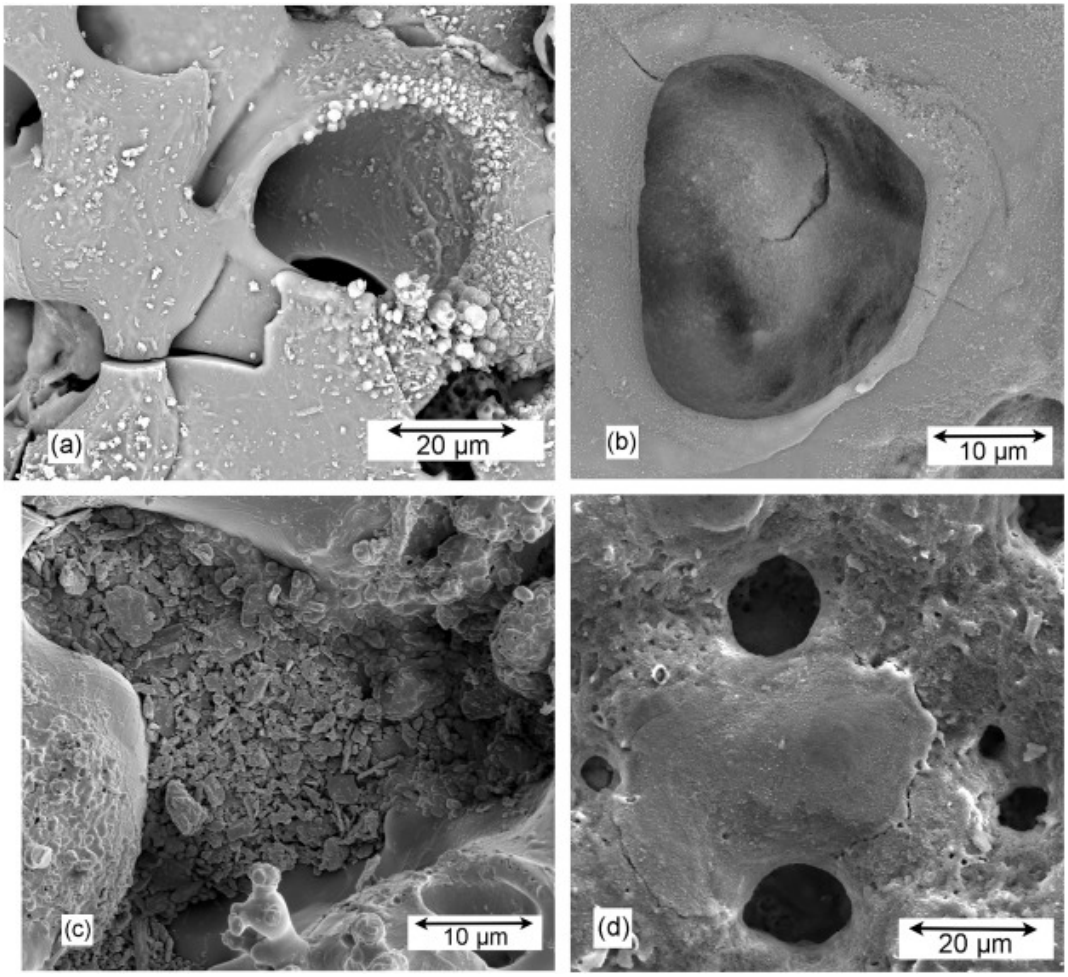

Fig. 6.6 SEM micrographs of free surfaces for the following cases: (a) Al substrate, 4 g L^{-1} of 7 μm MgO for 60 min, (b) Al substrate, 4 g L^{-1} of 0.1 μm Al_2O_3 for 60 min, (c) Ti substrate, 4 g L^{-1} of 7 μm MgO for 30 min and (d) Ti substrate, 4 g L^{-1} of 0.1 μm Al_2O_3 for 30 min.

processing (when there is pronounced convective motion in the liquid, particularly in the vicinity of discharges). Nevertheless, such images can be at least suggestive. For example, the active discharge site visible in Fig. 8(c) clearly contains a lot of MgO particulate from the electrolyte.

6.4 Mechanism of Incorporation

6.4.1 Al Substrates

With the Al substrates, the rate of mass gain is unaffected by the presence of relatively coarse (30 μm) particulate, but increases in the presence of smaller (7 μm) particles and is raised substantially when nano-particles (100 nm) are present. For the latter two cases, the extra mass gain rises more or less linearly with particle concentration in the electrolyte, at least up to a level of 4 g L^{-1}. As was mentioned in §4.8 , at this level the individual nano-particles are about a micron or so apart, assuming that they have become uniformly dispersed (which in practice may not be a reliable assumption for many nano-powders). It seems clear that these finer particles, particularly the nano-particles, are absorbed into the coatings, making them thicker (and also apparently more homogeneous - see Figure 6.2). For both the magnesia (7 μm) and the alumina (100 nm) additions, there appears to have been little or no chemical reaction during incorporation. This is probably expected in view of the thermodynamics relevant to the chemical environment. The standard PEO coating is composed almost entirely of alumina (α or γ), with it being likely [1] that the metastable γ phase is the one that forms during the rapid quenching of the plasma, while subsequent "annealing" of regions around discharges leads to conversion of some of it to the thermodynamically stable α phase. Formation of other phases seems unlikely. It is possible under certain conditions [163] to form a spinel by reaction between Al_2O_3 and MgO, but this is not likely to be a favoured reaction in the environment of interest here.

6.4.2 Ti Substrates

With the Ti substrates, there is no mass gain in the absence of particles, presumably due to some of the coating being lost into the electrolyte while PEO takes place. However, the presence of particulate, particularly when fine, does lead to mass gain, and to thicker coatings being formed. This works for both the magnesia (7 μm) and the alumina (100 nm) additions. However, unlike the Al substrate case, there is evidently considerable scope for chemical reactions to take place during incorporation. In fact, a substantial proportion of the alumina, and virtually all of the magnesia, get converted to a titanate phase. This observation does suggest that the process is not simply one of particles being adsorbed onto the surface, since it clearly requires exposure of the particulate to high temperature in the presence of Ti. While a general (electrophoretic) attraction of particles to the surface could play a role, it would appear that they become preferentially located in discharge sites, suggesting that they are carried in by convective filling of the pores (at the end of the discharge cycle).

6.4.3 Electrophoresis

There have been many studies [164, 165], over an extended period, of the fundamentals of electrophoresis. The case of interest here is that of small ($<\approx 1\mu$m diameter) particles in dilute aqueous electrolytes. Electrophoretic forces arise when individual particles acquire a net charge, in the presence of imposed electric fields. There is, however, complexity in this, since the nature of the electrolyte tends to have a strong effect on both the dispersion of the particles and the charge distribution in the vicinity of each one. For example, Hanaor et al. have shown [140, 141] that carboxyl acids are very effective in covering particles with negatively charged species, imparting highly negative zeta potential values and allowing fine (ZrO_2 and TiO_2) particles to be maintained in dispersed suspension over a wide range of

pH. In fact, there have been several PEO studies [146, 166, 167] with suspended particulate in which the zeta potential of particles has been measured to be a few tens of millivolts (in typical alkaline electrolytes).

Nevertheless, it is possible to make some crude estimates concerning electrophoretic forces on particles, and likely resultant motion, in the vicinity of a PEO surface. The electric field, E, being generated within the electrolyte [74, 88, 168–171] in such a location could be of the order of a hundred V m^{-1} at most: it's unlikely to be more than this, since most of the applied potential during PEO is dropped across the residual oxide layer on the substrate. The resultant force, F (Newtons) acting on the particle is the product of this and the net charge, q (Coulombs). Setting this equal to the drag force ($3\pi d\eta u$), the terminal velocity of a particle in water is given by:

$$u_{ter} = \frac{qE}{3\pi d\eta} \tag{6.3}$$

where d is the particle diameter and η is viscosity (in this case of water). This can also be expressed in terms of the mobility, μ of the charged particle:

$$u_{ter} = \mu E \tag{6.4}$$

Estimating the effective net charge on a small particle of this type is not straightforward, so a simpler alternative is to use the relationship between the zeta potential, ζ, and the mobility, given by the Smoluchowski relationship:

$$\mu = \frac{\varepsilon_r \varepsilon_0 \zeta}{\eta} \tag{6.5}$$

where ε_r is the relative permittivity of the electrolyte and ε_0 is the permittivity of free space. Taking ε_r and η for water to be about 80 and 10^{-3} Pa s, and using upper bound values of $\zeta \approx 100$ mV and E ≈ 100 V m^{-1}, leads to $\mu \approx 7$ x10^{-8} m^2 V^{-1} s^{-1}. This gives a value for the terminal velocity of about 7 μm s^{-1}. Not only is this very much an upper bound, but it also takes no account of the time needed to reach the terminal velocity. Furthermore, for a typical supply frequency of 50 Hz, the period during which a substantial field acts is only about 5 ms. The distance that an individual particle would be likely to move during this period as a result of electrophoretic forces is thus a small fraction of a micron. This is unlikely to make any significant contribution to the flux of particulate needed to explain the observed incorporation. Furthermore, any such motion is likely to be completely inconsequential compared with other forces in the electrolyte, such as convective motion from the pump and movement due to rapid expansion and contraction of the gas bubble during each discharge cycle, which has been shown [114] to occur with a velocity of ≈ 10 m s^{-1}.

6.4.4 Particle Sweeping into Discharge Pores

In fact, it seems clear that the main mechanism of incorporation of suspended (fine) particles involves them being swept into pores or depressions on the coating surface as part of the PEO discharge cycle, during the refilling with electrolyte that follows expansion and subsequent collapse of the plasma "bubble". Figure 6.7 shows a schematic depiction of a single cycle, for an electrolyte containing suspended particulate that is fine compared to the scale of the discharge pore. (This representation is based on the architecture of a real PEO discharge pore, captured tomographically [74].)

Some order of magnitude estimates can be carried out relating to this cycle. If a typical pore (discharge cascade site) is taken to be a cylinder of diameter D and length L, then the volume of electrolyte entering it is given by

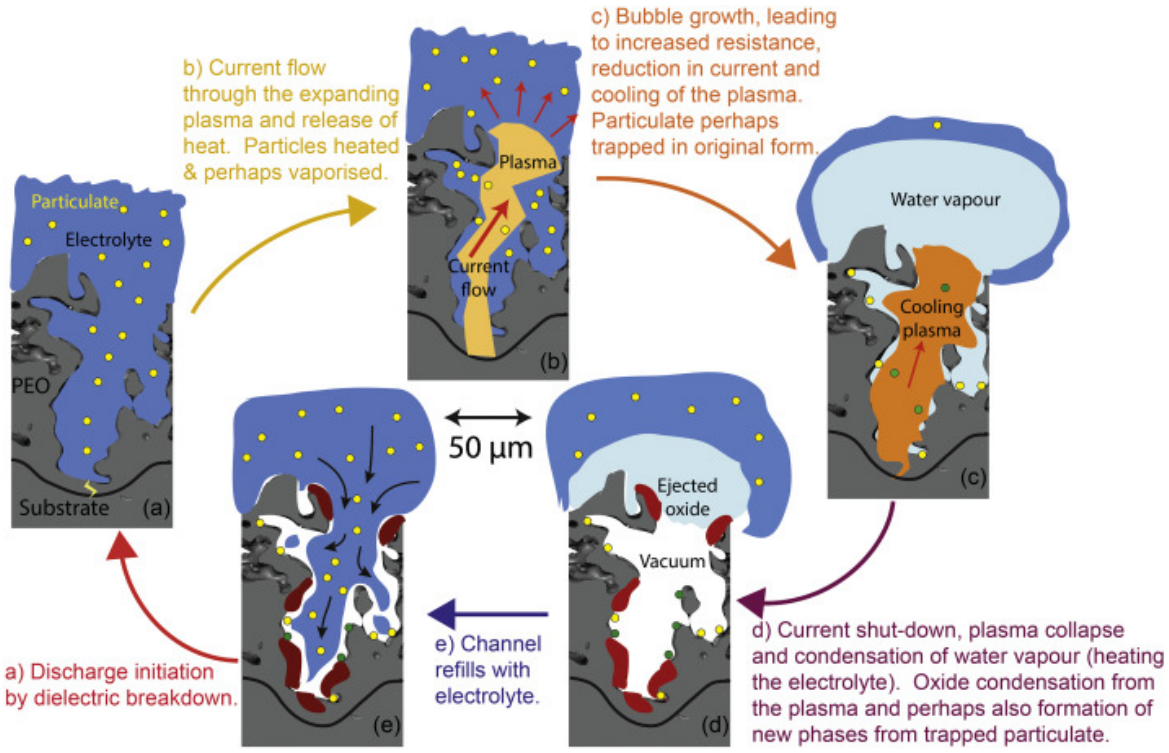

Fig. 6.7 Schematic representation of a single PEO discharge cycle, with the electrolyte containing suspended particulate.

$$V \approx \frac{\pi D^2 L}{4} \tag{6.6}$$

and hence, for a particle concentration level in the electrolyte of C g L^{-1}, the mass of particles entering the pore, m_p is given by:

$$m_p \approx \frac{\pi D^2 LC}{4} \approx \frac{\pi(20\times10^{-6})^2(50\times10^{-6})(4\times10^3)}{4} \approx 10^{-10} g \tag{6.7}$$

The numbers being used here are estimates of typical (discharge site) pore dimensions [77] and a value of 4 g $L^{-}1$ for C. Of course, the estimate is a crude one, to say the least. Nevertheless, it may immediately be noted that this figure is similar in magnitude to what is thought [74] to be a typical value for the mass of oxide formed during a single discharge cycle of conventional PEO.

It follows that more particulate is likely to be incorporated per discharge when the coating has become thicker and the discharge site pores have thus become deeper (and usually wider as well). This is consistent with the observations of Matykina et al. [109] that higher concentrations of incorporated zirconia particles were found towards the outside of thicker coatings. On the other hand, it is commonly observed [74] that the discharges become more energetic with thicker coatings, so that more substrate oxidation is also expected to occur per discharge. (It's commonly the case that the process progresses with the current, and power, remaining approximately constant as the coating thickens, with this increase in the energy associated with each discharge being accompanied by a progressive decrease in the spatial and temporal frequency of discharges.) This is consistent with the observation that the relative contributions to mass gain from particulate incorporation and from substrate oxidation remain approximately constant with increasing coating thickness.

It may thus be concluded that particulate incorporated in this way can have a noticeable effect in increasing the rate of mass gain, provided that at least some of the particulate swept into a discharge site in this way does become trapped in the coating. In fact, such entrapment seems very likely, and could involve the particles becoming molten, or even vaporised, as the plasma expands, possibly followed by a different phase being formed during cooling. Of course, not all ingested particulate will necessarily reach very high temperatures. Some of it could be projected into surrounding porosity as the plasma expands. This is consistent with the observation that a proportion of the incorporated Al_2O_3 nano-particles remained as α, whereas rapid heating and quenching might have been expected to convert it to a metastable form such as the γ phase.

6.5 Summary

This investigation concerned the mechanisms by which (fine) particles become incorporated into plasma electrolytic oxidation (PEO) coatings when added to the electrolyte. Three different types of particle were used, covering a wide size range, and processing has been carried out with both Al and Ti substrates. For some of these combinations, the particulate was chemically similar to the expected PEO product, while for others it was different. It has been established that, where such reactions are chemically favoured, phase changes can occur that must have involved the particulate reaching very high temperatures. From this and other evidence, it is concluded that the main incorporation mechanism involved is that of (fine) particulate being swept into the pores associated with active discharge sites, while they are being refilled with electrolyte immediately after collapse of the plasma. They are then likely to become entrapped, and in many cases to be strongly heated as the plasma is created during the next discharge cycle. Typical pore sizes are such that particles (or particulate clusters) above about 10 μm in size would be unlikely to enter them. While particles a few

microns in diameter can become incorporated, it takes place more readily with sub-micron particles. It is also concluded that electrophoretic forces are unlikely to play any significant role in the incorporation process.

Chapter 7

Incorporation of Alumina Fibres Suspended in the Electrolyte

There has been much recent interest in modifying the surface topography of PEO coatings to increase surface area, particularly for functional coating applications such as photocatalysis. The incorporation of relatively high aspect ratio fibres into the coating shows promise for achieving this, and this chapter concerns the effect of adding Saffil® fibres to the electrolyte on sample mass gain and on the electrical repsonse of the system. A mechanism for the uptake of these fibres will be proposed.

7.1 Outline of Experiments

Saffil® fibres of nominal diameter 3 μm were milled according to the methodology outlined in §4.9, until aspect ratios of 10-20 were achieved. An SEM micrograph of the milled fibres is given in Figure 4.7.The milled fibres were then mixed with a small amount of electrolyte

using a magnetic stirrer before this suspension was added to the bulk. This reduced the likelihood of agglomeration. Plate samples of aluminium and titanium were processed for 60 and 30 minutes respectively, in electrolytes with a fibre concentration of 0, 1, 2 and 4 g L^{-1}. Processing was carried out at a current density of 20 A dm^{-2}, and the voltage generated by the machine to hold this current was recorded for the duration of processing in each case. The mass of each sample was measured before and after processing. The free surface and sectional morphology of the resulting coatings were examined using SE microscopy, and their phase constitutions were determined using XRD.

The effect of direct electrolyte jetting on the sample was examined. The electrolyte circulation pump is fitted with a posable nozzle of diameter 10 mm which was directed at the sample in two orientations:

- **Side-on Jetting**: The nozzle positioned such that the electrolyte impinged on the edge of the sample, so as to cause electrolyte flow across the face of the plate (i.e. parallel to the surface). The leading edge of the plate was positioned approximately 20 mm from the nozzle outlet. This configuration used the standard plate geometry as described in Figure 4.1 (a).

- **Jetting Through Holes**: A plate sample with a 5 $\times$ 5 array of 1.5 mm^2 drilled holes, as described in Figure 4.1 (b) was used in this configuration. The nozzle outlet was directed normal to the face of the plate, and arranged such that the centreline of the jet aligned with the centreline of the central drilled hole. The plate was positioned approximately 30 mm from the nozzle outlet.

The flow rate through the pipe was measured to be $\approx$ 6 L min^{-1}, corresponding to a velocity at the nozzle outlet of $\approx$ 12.7 m s^{-1}. Aluminium and titanium samples were processed using the same electrical regime, using a fixed current density of 20 A dm^{-1}

(the current was adjusted for the 'jetting through hole' samples to account for the change in surface area in order to keep the current density constant). Sample masses were again recorded before and after processing. The effect of electrolyte jetting on the free surface morphology was examined using SE microscopy, and a fibre incorporation mechanism is proposed.

7.2 Mass Gain

Mass gain data for all test cases are shown in Figure 7.1. It can be seen that similar trends are observed for both substrates in terms of the effect of the presence of fibre in the electrolyte, although the rates of mass gain are lower for the Ti. As was the case in Chapter 6, it can be seen that, in the absence of fibre there is actually a mass loss for the Ti for all cases except for the highest concentration (4 g L^{-1}). The explanation for this, as discussed in Chapter 6, is that there is a tendency with Ti substrates for some of the coating to be ejected into the electrolyte, often visible as accumulating suspended particles. The increase in mass gain with concentration was less pronounced for fibre addition than small particle addition, which is not surprising given that in the previous chapter, it was found that the likelihood of a particle becoming incorporated increases with decreasing particle size.

7.3 Coating Microstructures

7.3.1 Morphology

Figure 7.2 contains free surface micrographs of both substrates processed with and without fibre suspension in the electrolyte. For aluminium substrates (Figures 7.2a and 7.2b) it was

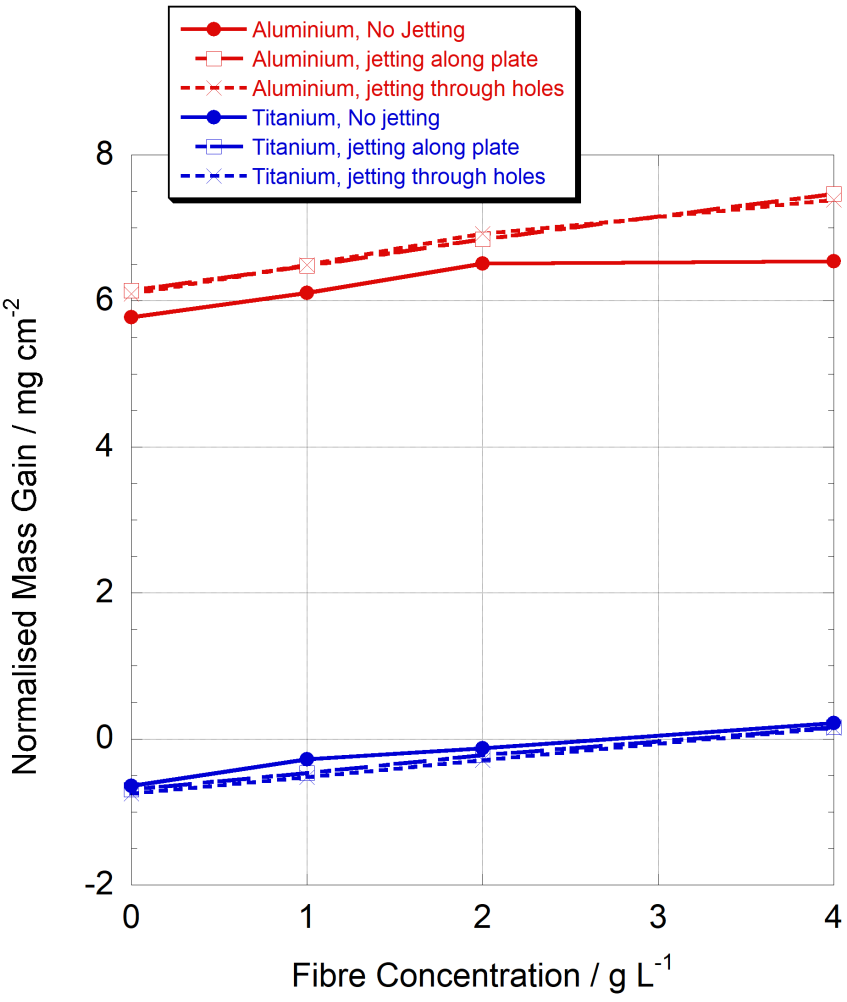

Fig. 7.1 Mass gain data for all experimental cases on aluminium and titanium, normalised by sample area.

found that the free surface morphology did not change significantly, and any fibres visible appear to be rested on the surface and not substantially incorporated into the coating. As discussed previously, during processing, the coating is constantly being restructured by constant discharging, and any micrograph shown simply shows a 'snapshot' of the coating at that moment in time (in this case after 60 minutes of processing). The fibre seen in Figure 7.2b has more than likely settled onto the free surface as the sample was being removed from the electrolyte.

Titanium on the other hand, shows evidence of reactive incorporation. Multiple mounds of diameter 20–30 μm are evident across the surface on the coating processed in fibre-containing electrolyte. A BSE micrograph of one such mound viewed in transverse section is given in Figure 7.3, along with EDX maps of the same image. It can be seen that the whole mound contains at least some Al, and there is a region near the top that is predominantly Al and deficient in Ti. This strongly suggests the presence of a Ti-Al mixed oxide in the vicinity of the mound, which has been shown to form readily in PEO conditions where both Al and Ti are present [172].

If a fibre with a length of 25 μm (approximately the median of the length distribution) were to be fully melted and solidified as a circular mound of diameter of 25 μm, the mound thickness would be $\approx 3\mu$m to conserve volume (for a fibre diamter of 3μm). The mound in Figure 7.3 is somewhat thicker than this, but this could be due to a variety of reasons. Firstly, the mound is not cylindrical in shape but hemispherical, which could lead to the thickness being overestimated at the edges, but most markedly the mound clearly incorporates Ti from the coating, meaning the final volume needs to be larger to include the new material. From this evidence, it is presumed likely that each mound is the result of the entrapment and melting of at least one discrete fibre.

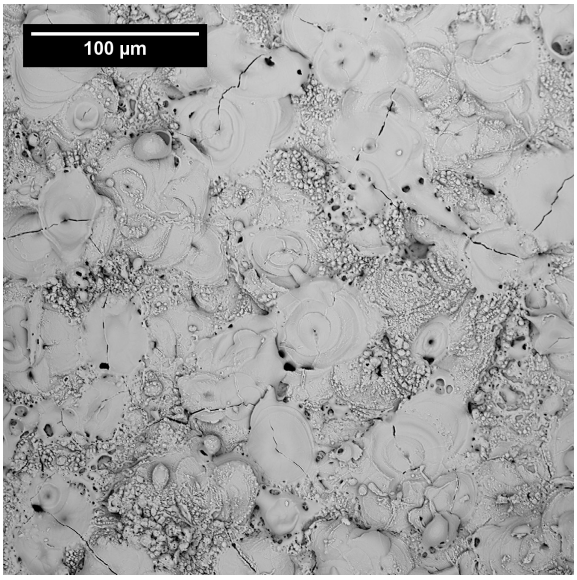

(a) Aluminium substrate coating after 60 minutes, with no fibre addition.

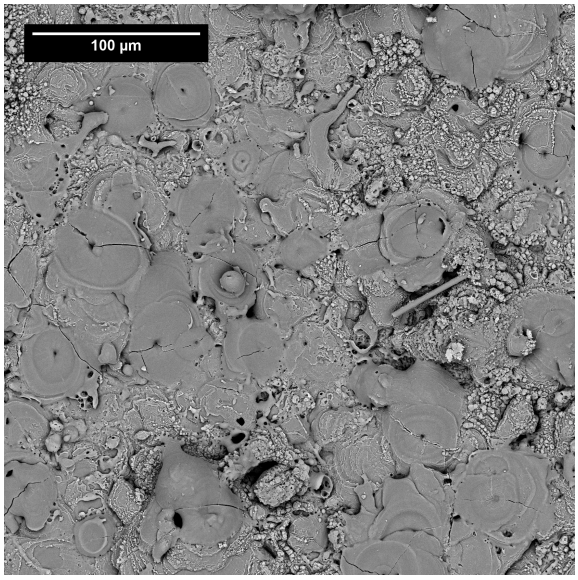

(b) Aluminium substrate coating after 60 minutes, with 4 g L^{-1} fibre addition.

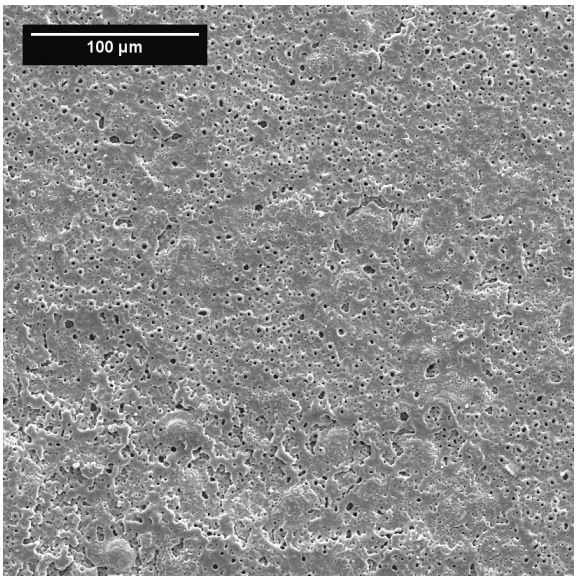

(c) Titanium substrate coating after 30 minutes, with no fibre addition.

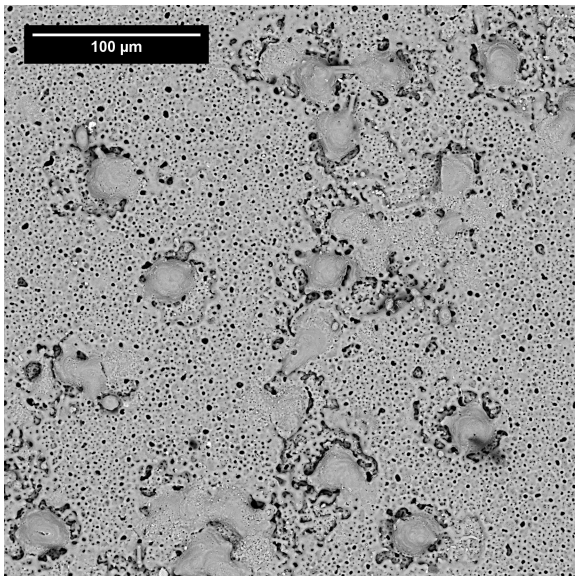

(d) Titanium substrate coating after 30 minutes, with 4 g L^{-1} fibre addition.

Fig. 7.2 Free Surface BSE micrographs of Al and Ti samples with and without fibre addition.

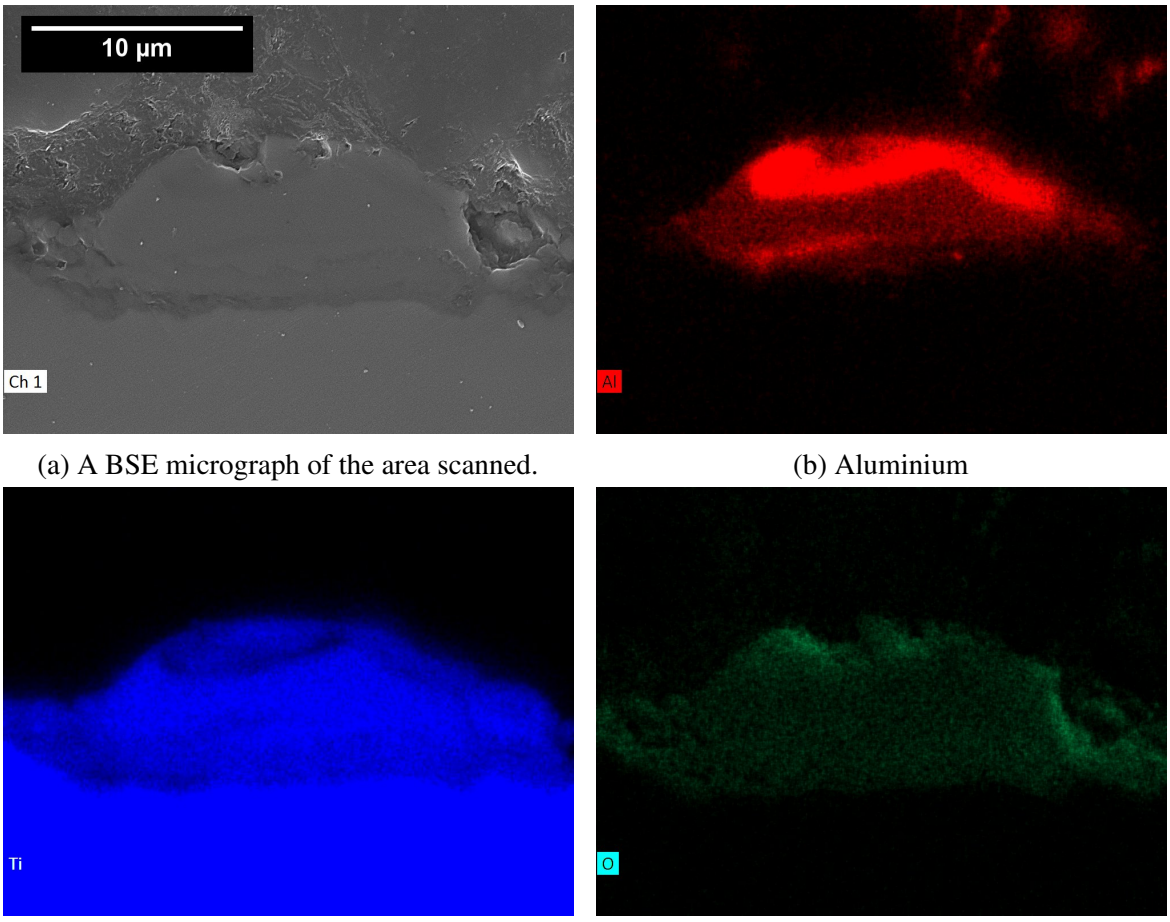

(a) A BSE micrograph of the area scanned.

(b) Aluminium

(c) Titanium

(d) Oxygen

Fig. 7.3 A BSE micrograph and corresponding elemental composition maps of a “mound” in cross-section, in a Ti coating processed in electrolyte containing 4 g L^{-1} Saffil fibres for 30 minutes. Only elements with an overall composition of more than 5% were included.

7.3.2 X-Ray Diffraction

An indication of the phase proportions in the coatings formed on both substrates can be obtained from the X-ray diffraction spectra shown in 7.4, which relates to a processing time of 60 minutes for Al and 30 minutes for Ti. Spectra are provided for both the zero and the highest (4 g L^{-1}) fibre loading case. It can be seen from 7.4a that for both Al coatings, the majority of coating material consisted of α, γ or θ-Al_2O_3 phases. The relative contributions from these three phases appear to be similar for both electrolytes, although since the fibres were composed of alumina, it is difficult to draw any meaningful conclusions from this. It is telling, however, that no δ-Al_2O_3 peaks were recorded, suggesting that the in-tact surface fibres such as that in Figure 7.2b do not constitute a significant proportion of the coating mass.

Corresponding XRD spectra are shown in Figure 7.4b for the Ti substrate, after processing for 30 min. Spectra are shown for samples processed without any fibre addition and with the highest loading. The spectrum with no fibre mainly comprises anatase peaks, with a few from the rutile phase. The spectrum from the sample processed with fibre addition is rather more complex, but it is fairly clear that the main phases are still anatase and rutile, but a number of other peaks are present. These appear to be caused by the presence of aluminium titanate (Al_2TiO_5). This is consistent with the EDX map in Figure 7.3, showing overlapping presence of Al and Ti in the mound. This reaction presumably takes place during cooling of the plasma at the end of the discharge cycle. As discussed in Chapter 6, this phase is highly stable and is known to form quite readily when the elements concerned are all present, and implies that the particulate has been exposed to high temperatures during the processing. It should be noted that the relative proportion of Al_2TiO_5 appears to be low compared to the anatase and rutile phases, but this reflects the relatively minor increase in mass gain, when processed in fibre-containing electrolyte.

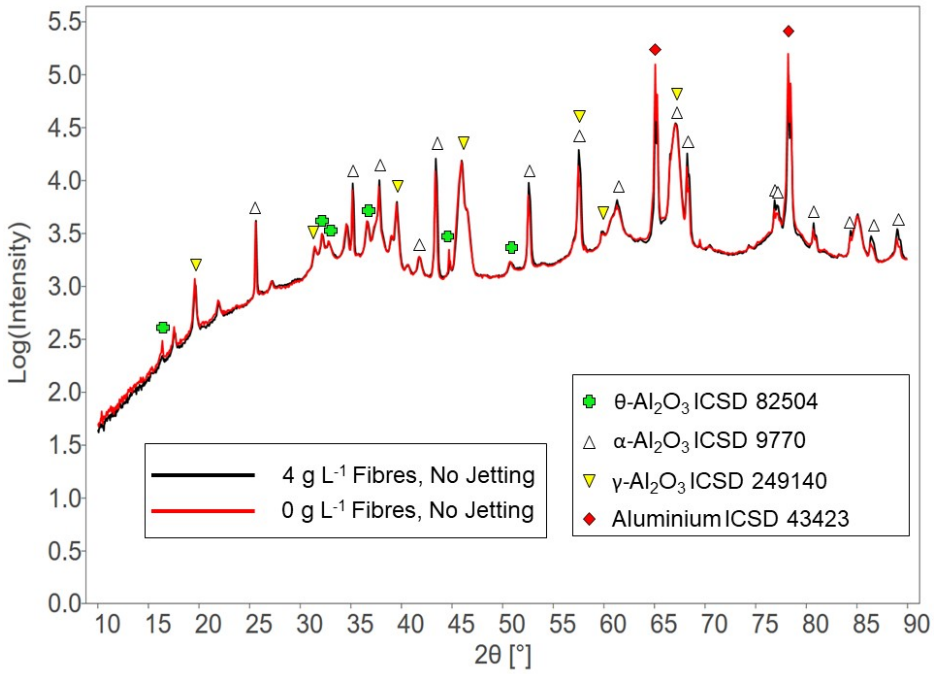

(a) Al

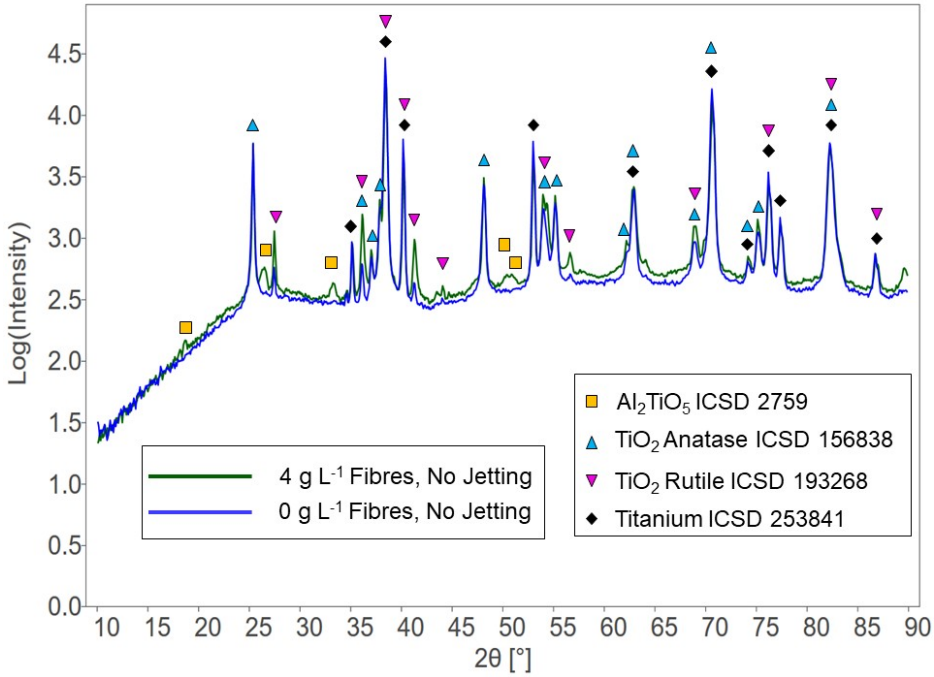

(b) Ti

Fig. 7.4 XRD spectra of Al and Ti coatings after processing for 60 and 30 minutes respectively, with fibre loadings of 0 and 4 g L^{-1}

7.4 Effect of Electrolyte Jetting

It is important to firstly consider the change in structure of the coating when electrolyte jetting is used, without the presence of additions. BSE images of the free surface of the Al coating under the three electrolyte jetting conditions are given in Figure 7.5. For the "jetting through holes" case, the free surface was indistinguishable from the conventional case on the free surface, away from any holes. Around the drilled holes (entrance and exit), a build-up of coating material was observed, particularly at the hole exit region in Figure 7.5b, in which it can be seen that the coating appears to overhang the edge of the hole. It has been observed that convergent electric field affects at edges can cause a local increase in current density, resulting in a thicker coating at geometric edges. This thickness variation is usually slight, but is observed regularly in plate samples.

When jetting is applied parallel to the surface, evidence of the molten oxide flow (i.e. after being heated by an active discharge) in the direction of flow was seen. Regions such as those shown in Figure 7.5c were common, as were individual discharge pores such as that shown in Figure 7.5d, which show a distortion of the conventional 'pancake' shaped pools of solidified oxide, possibly by viscous forces caused by the electrolyte flow.

The free surface of the Ti coatings after processing under the three jetting conditions are given in Figure 7.6. The coating around the drilled hole appears to be unaffected by the flow of electrolyte, and again the coating on regions away from the drilled holes is indistinguishable from the conventional coating. When the electrolyte is jetted parallel to the surface, however, a directional coating structure was observed. Streaks of oxide can be observed in Figure 7.6c (and in higher resolution in Figure 7.6d), which are aligned with the flow direction. It was observed that the thickness of these streaks were roughly twice that of the surrounding material (≈ 15 μm compared to ≈ 8 μm). It is not immediately clear why

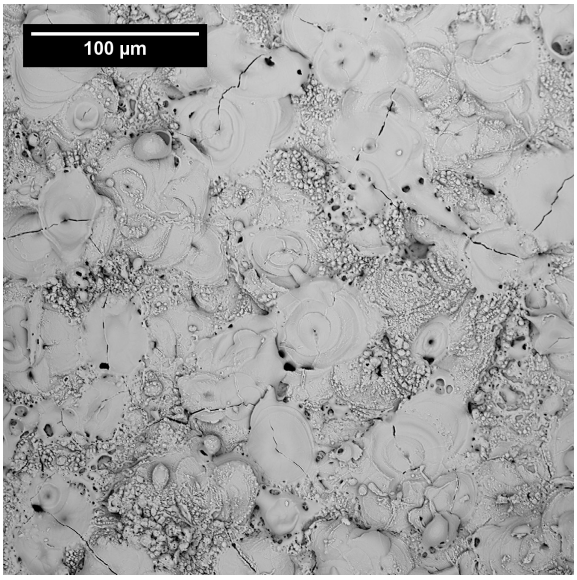

(a) Al, conventional processing (no jetting).

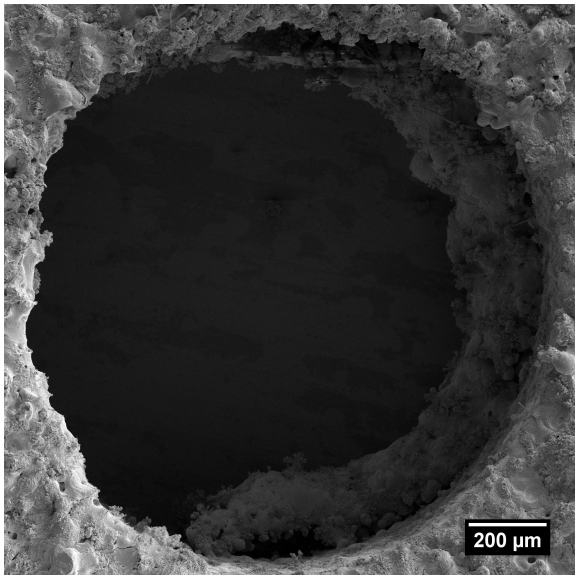

(b) Centreline hole (flow is normal, into page).

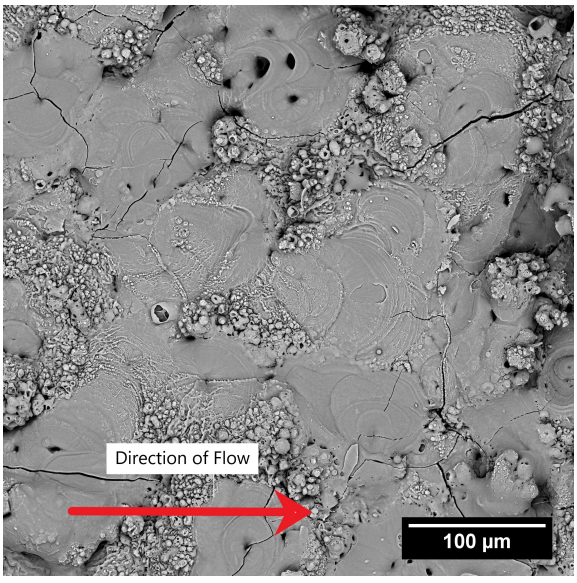

(c) Side-on jetting sample

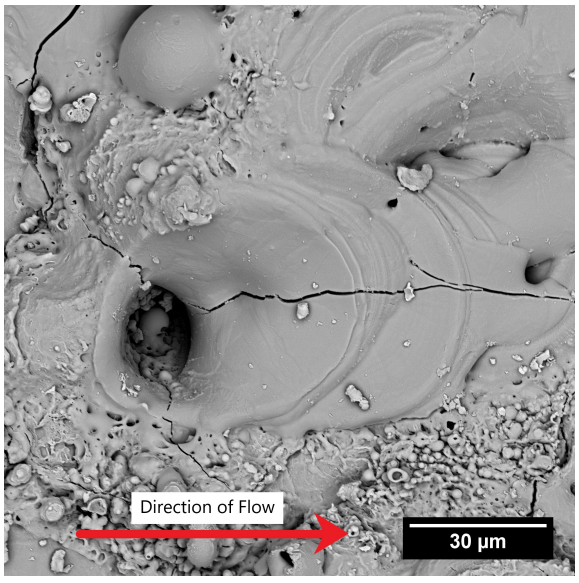

(d) An individual pore on the side-jetting sample.

Fig. 7.5 BSE micrographs of the free surfaces of Al samples processed for 60 minutes under different electrolyte jetting conditions, with no electrolyte addition.

the effect of parallel jetting is more pronounced in this case than on the Al coating. If the melting point of titania were considerably lower, it would be possible that the coating were simply remaining molten for a longer period of time, allowing the streak of molten oxide to elongate. The melting points of the oxides are, however, actually quite similar, at 2345 K for alumina and 2116 K for titania, so this is unlikely to be a major factor. While the streaks do appear to have some fine-scale porosity (see Figure 7.6d), there is a distinct lack of the characteristics of rapid cooling as seen on the Al coating such as the appearance of large cracks.

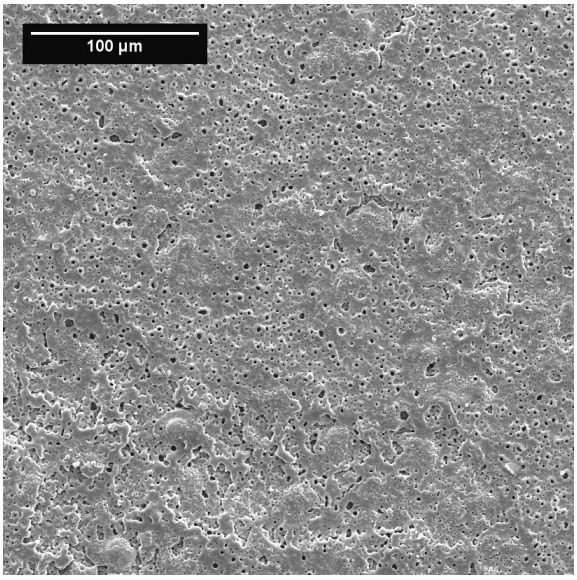

(a) Ti, conventional processing (no jetting).

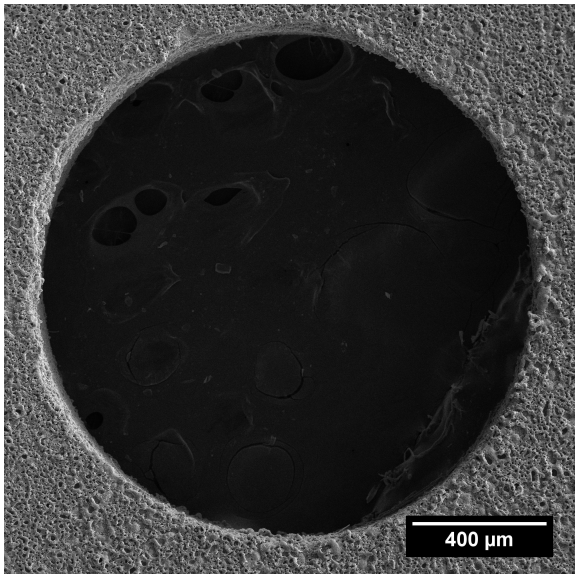

(b) Centreline hole (flow is normal, into page)

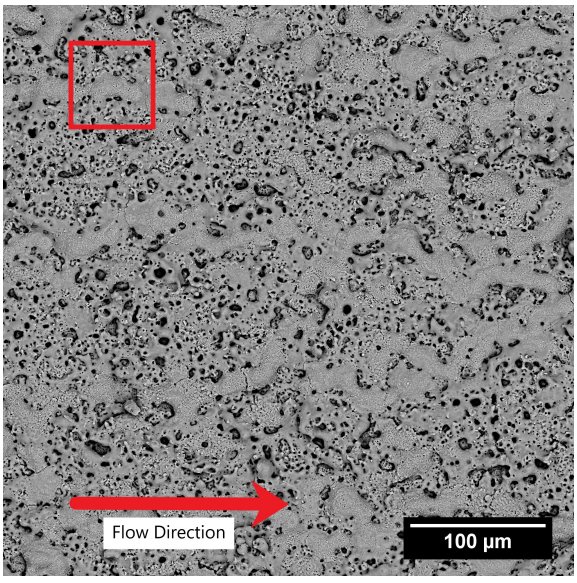

(c) Side-on jetting sample.

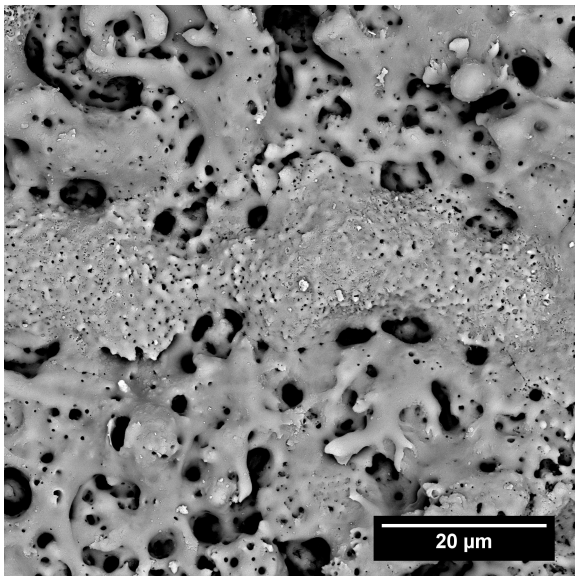

(d) The image in c), zoomed in to the area surrounded by a red square.

Fig. 7.6 BSE micrographs of the free surfaces of Ti samples processed for 30 minutes under different electrolyte jetting conditions, with no electrolyte additions.

7.5 Electrical Response

The issue of whether or not electrolyte additions affect the electrical response of the system during PEO processing has raised some confusing and contradictory results, as discussed in §3.3. In the present work, a constant current density condition was set, such that the power supply was free to vary the voltage to maintain that current (20 A dm^{-1}). The voltage response of the system for the processing of both substrates is given in Figure 7.7, with and without the presence of fibres (the highest loading case of fibres is shown, i.e. 4 g L^{-1}). It can be seen that for the Al substrates, the addition of fibre particulate has the effect of slightly increasing the anodic processing voltage, although it should be noted that such an increase is roughly within the range of experimental variation. For Ti, the traces are virtually indistinguishable. Since the fibre being added is alumina, an excellent electrical insulator, it might be expected that the conductivity of the electrolyte would decrease (indeed this would correlate with the increase in processing voltage observed), however it must be borne in mind that the amount of fibre added, even in the highest loading case, has a volume fraction of fibre of only around 0.1%, and as such the conductivity did not change measurably when fibres were added.

The discharging behaviour of the two substrates tested may, however, provide in an insight into the slight increase in processing voltage observed with the Al substrate. In §5.2.2, it was reported that Ti discharges tended to be less energetic and more spatially diffuse than those on Al. Although the volume fraction of fibres in the electrolyte as a whole is low, if a fibre were to become entrapped in a pore (which, as will be discussed in §7.6.1 is the likely mechanism for incorporation), the electrical resistance between the top of the pore channel and the barrier layer could increase measurably, if not significantly. Since there are more active discharge sites at any point in time for Al, that local increase in resistance would raise the overall electrical resistance of the system more significantly than if one discharge pore

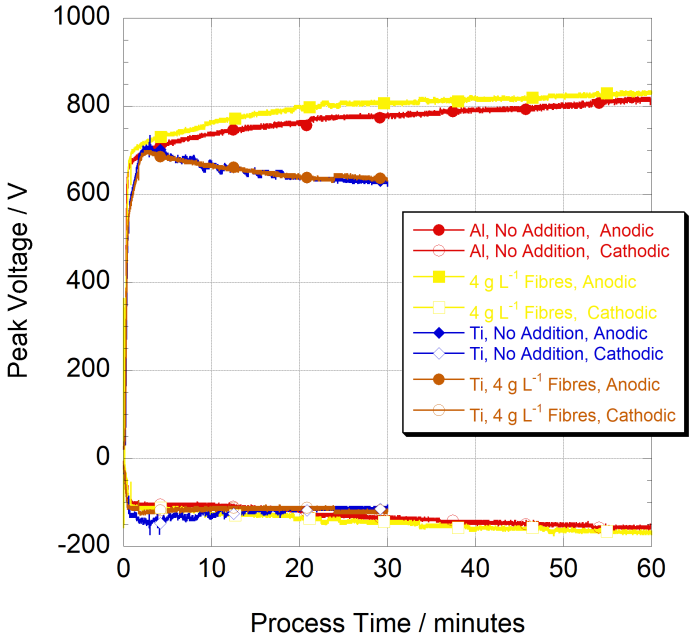

Fig. 7.7 Peak anodic and cathodic voltages recorded during processing of Al and Ti substrates without electrolyte jetting for 60 and 30 minutes respectively, with no fibre additions and with the addition of 4 g L^{-1} Saffil fibres to the electrolyte.

in a Ti coating contained a trapped fibre. This is speculative, but what is clear is that the conductivity of the electrolyte itself does not change measurably and is therefore not a factor concerning the difference in electrical response when fibres are added.

As the jetting set-up used in this study is novel, the effect of jetting alone on the electrical response should be investigated. The voltage response of the system for the processing of both substrates with no addition, under the various jetting conditions is given in Figure 7.8. It can be seen that for Al, each voltage trace is effectively indistinguishable, and any differences are well within what would be expected as experimental variation. For Ti, the edge jetting appears to necessitate a slightly higher voltage, but as with the fibre addition, it is within experimental variation. If the flow (parallel to the surface) over a given pore had a velocity of a known value, then a related pressure drop could be calculated. The growth of a bubble after the initiation of a discharge would be energetically more favourable, as the pressure differential between the interior and exterior of the bubble would be lower (for a

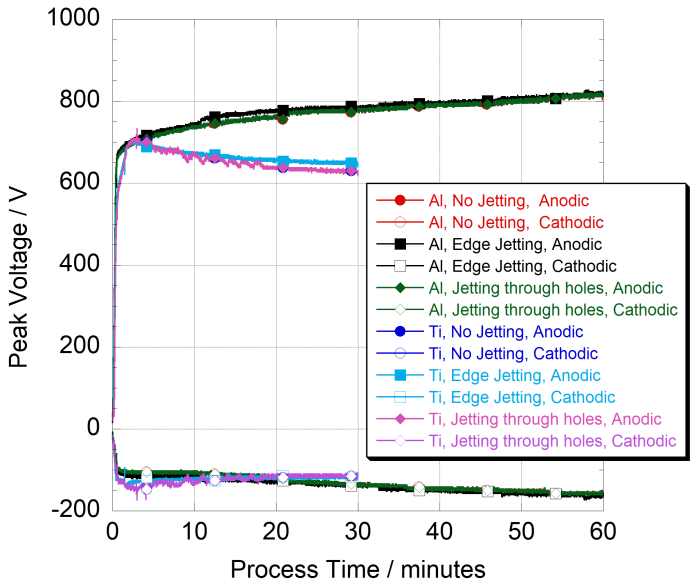

Fig. 7.8 Peak anodic and cathodic voltages recorded during processing of Al and Ti substrates with no electrolyte addition for 60 and 30 minutes respectively, under various electrolyte jetting conditions.

given bubble radius). This could potentially allow discharges to persist for a longer period of time. Alternatively, a high flow velocity could shear off bubbles prematurely and terminate discharges in the process. More experimental work is needed in this regard, to elucidate the effect of a defined electrolyte flow velocity on discharge behaviour.

7.6 Mechanism of Incorporation

7.6.1 Fibre Entrapment in Pores

Due to the chemical difference in species between the alumina-rich fibres and titania-rich Ti coating, more salient information about possible incorporation mechanisms can be extracted from the Ti cases than the Al, although it has been established from the mass gain studies that at least some fibre incorporation is occurring on both substrates, (in fact the absolute

mass gain is quite similar for the two substrates). It is unlikely that any incorporated fibre would remain as δ-alumina, as XRD spectra have shown no evidence for the structure in the Ti coatings (which has been shown to contain Al in EDX studies), therefore it is still possible for the fibre to have been incorporated into the Al coating, where it is converted to another form of alumina. Figure 7.9 gives an EDX map scan of the free surface of a Ti coating processed in electrolyte with the highest loading case. It can be seen that the surface is scattered with Al-rich mounds, which are slightly depleted in Ti. Some partially intact fibres can also be seen in Figure 7.9b as bright red elongated particles. A BSE micrograph of a partially melted fibre from this coating is given in Figure 7.10.

In terms of the mechanism of incorporation of these fibres, electrophoresis can probably be discounted immediately, as the relatively large drag factor of these fibres will drastically reduce their terminal velocity under an applied field (see Equation 6.3 in §6.4.3). The most likely method of incorporation is likely the entrapment of fibres in molten oxide ejected by a recent discharge. To illustrate this, a schematic with four situations showing how a fibre may be trapped is shown in Figure 7.11. In situation (1), a fibre has contacted the surface of the coating near an inactive discharge pore. This is very likely to occur, as even without direct electrolyte jetting, the mean centre-to-centre distant between particles is of the order of 250 μm in perfectly dispersed electrolytes. In this case, as the site is inactive, there is no force retaining the fibre in that position, and hydraulic forces will, at some point, remove this fibre from the surface. Situation (2) illustrates a fibre contacting the coating surface immediately after a discharge has occurred. The fibre becomes embedded in the molten material ejected, and is not carried away by the bulk fluid forces. Sustained discharging at that site will then lead to situation (3) (show in Figure 7.10) where cascading (persistent discharging) has led to melting of the fibre. It is likely (based on the XRD evidence) that the Al in the fibre ends up as aluminium titanium oxide (Al_2TiO_5). Situation (4) represents the individual mounds seen

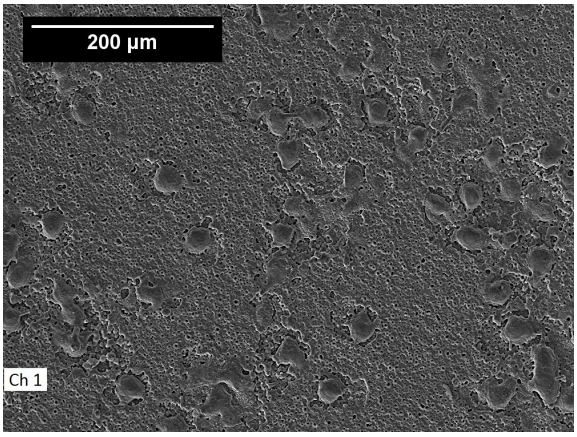

(a) BSE micrograph of the area scanned

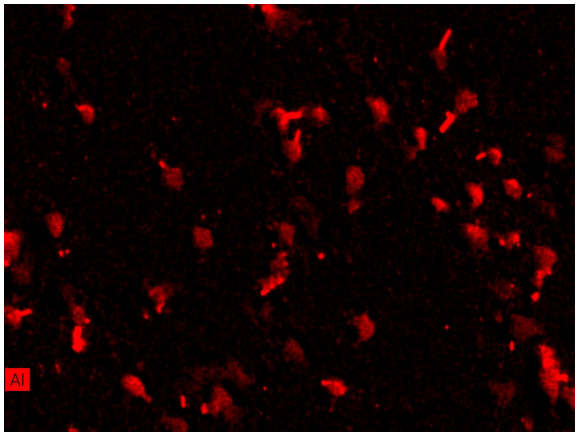

(b) Aluminium

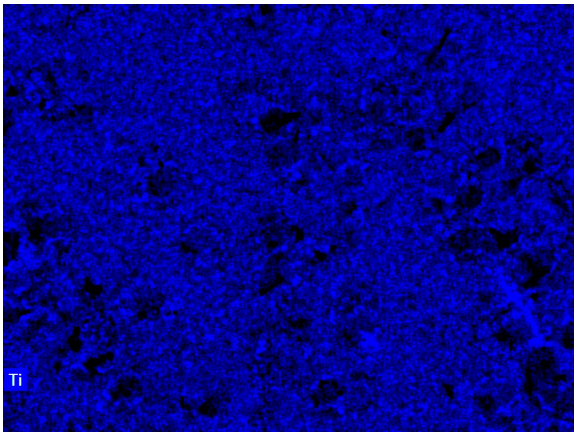

(c) Titanium

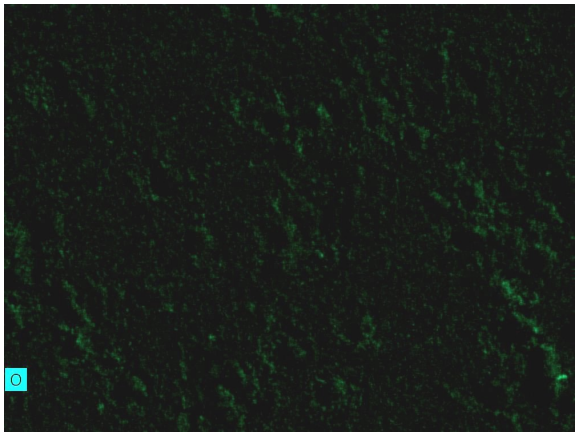

(d) Oxygen

Fig. 7.9 EDX maps based on the BSE micrograph in a), of the free surface of a Ti coating processed for 30 minutes in electrolyte containing 4 g L^{-1} Saffil fibres, with no electrolyte jetting.

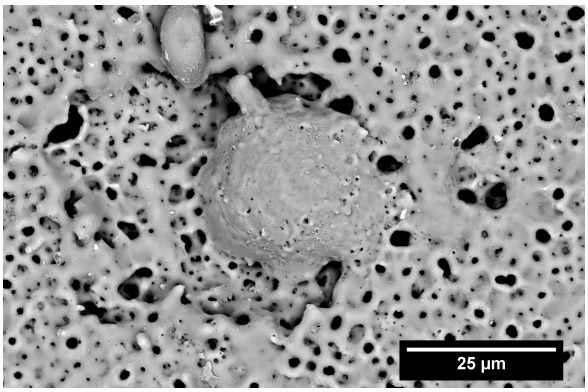

Fig. 7.10 A partially melted Saffil fibre on a Ti coating, with no electrolyte jetting.

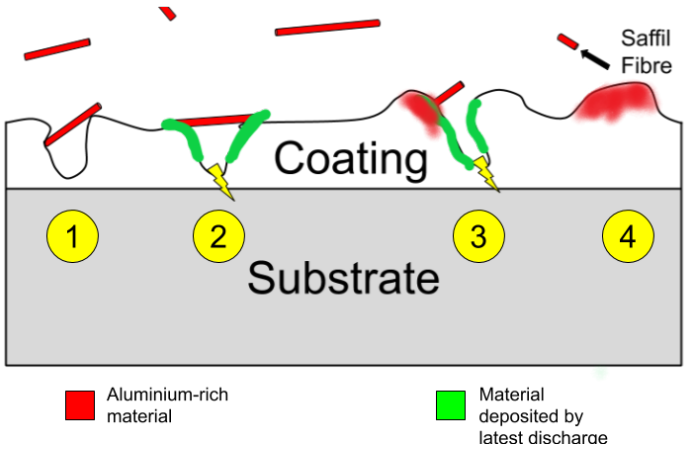

Fig. 7.11 A schematic showing a possible incorporation mechanism for Saffil fibres. Region (1) shows a fibre that has come to rest above an unactive discharge pore, region (2) shows a fibre that has become attached to the coating by becoming embedded in molten oxide, (3) shows a partially melted fibre, and (4) is a fully melted fibre, resulting in the observed mound structure.

across the surface of the Ti substrate, and occurs when full melting of fibre has occurred, due to sustained discharging.

7.6.2 Fibre Entrapment and Jetting

Jetting has been shown, in §7.4, to alter the surface morphology of the coatings, and for Al, to slightly increase the amount of fibre incorporated. Free surface and cross-sectional micrographs of Al coatings processed under various jetting conditions are shown in Figure 7.12. Considerably more unincorporated (i.e. discrete, unmelted) fibres were observed on the free surface of the sample which was jetted side-on. Features such as those shown in Figure 7.12a were common, as the fibres appeared to clump together, assisted by what appears to be previously molten oxide. As the fibre is essentially chemically identical to the coating, it would only be speculation to state the origin of this 'binding' oxide, but it is telling that even with jetting, no δ-alumina was detected in the XRD spectra. It should also be remembered that these images provide a snapshot of the final coating surface, while in reality the surface

is constantly being restructured through-thickness by energetic discharges, in this case for 60 minutes. It is therefore likely that these are 'stray' fibres, captured by molten oxide produced by the last set of discharges before processing was stopped, but are not strongly bound to the surface and would eventually detach if processing were to continue.

The 'jetting through holes' samples showed interesting microstructures when processed in fibre-containing electrolyte. After processing, it could be seen even by eye that the holes, especially those near the centre-line, appeared 'fuzzy'. A BSE micrograph of the centre-line hole, processed in electrolyte with the highest loading of fibres is shown in Figure 7.12b. It can be seen that fibres were trapped preferentially around the circumference of the hole. A Cross-sectional micrograph of the same hole is shown in Figure 7.12c. A relatively large bundle of fibres can be seen, mostly aligned tangential to the drilled hole. The reasons for this behaviour are not clear, although it is interesting to note that these fibres appear to be cocooned by a solid layer of coating material above, so it is possible that a molten flow of oxide, under the influence of the electrolyte jet, covers fibres that are captured early in the process. The cross-section of a drilled-hole sample processed in fibre-free electrolyte is shown for comparison in Figure 7.12d.

For Ti, the mass gain was virtually unchanged with the introduction of jetting. As can be seen in 7.13, the surface is no longer covered with mounds, but strands of Al-rich ridges, elongated in the direction of flow (left to right in this case). This is most likely due to the elongation of the molten fibre/oxide mixture due to viscous forces caused by jetting. An example of such molten flow under the influence of jetting was given in Figure 7.5d. It appears, for the Ti case at least, that this form of jetting causes a more even distribution of fibre material across the surface, but does not actually cause more fibre, in absolute terms, to be incorporated. There is a similar for the "jetting through holes" sample, an EDX map of which is shown in Figure 7.14. The normalised mass gain did not actually increase, but a

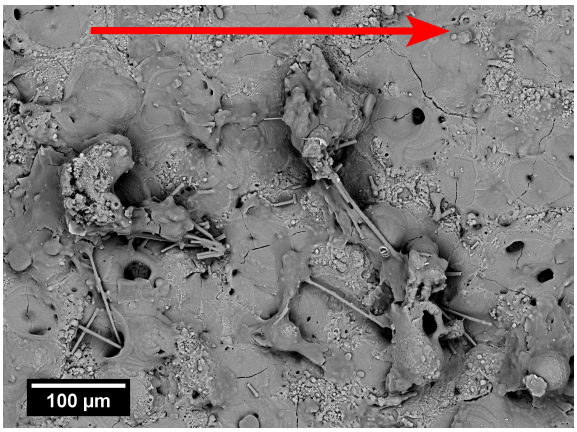

(a) The free surface of an Al substrate, processed for 60 min in electrolyte containing 4 g L^{-1} fibres, with electrolyte jetting across the face of the sample, in the direction of the red arrow.

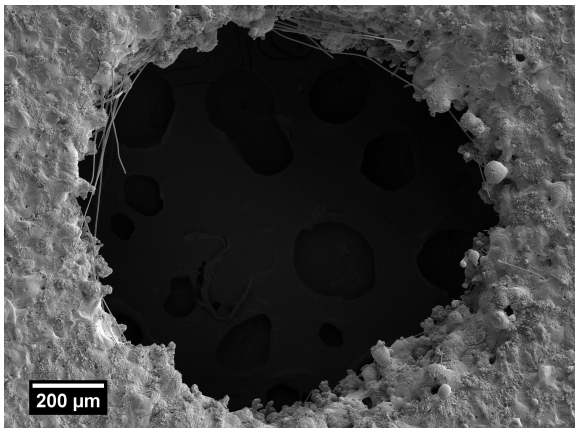

(b) The free surface of the centre-line hole of an Al sample, processed for 60 min in electrolyte containing 4 g L^{-1} fibres, with electrolyte jetting into the plane of the page.

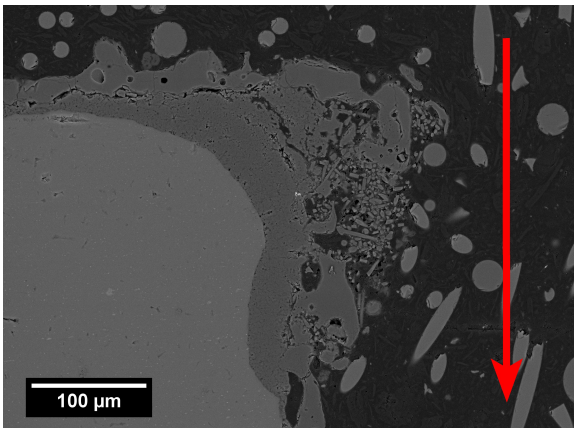

(c) The cross section at the centre-point of a hole, from a sample processed for 60 minutes in electrolyte containing 4 g L^{-1} fibres, with jetting in the direction of the red arrow. Note that this image is at a magnification two times that of (d), to show the incorporated fibre in more detail.

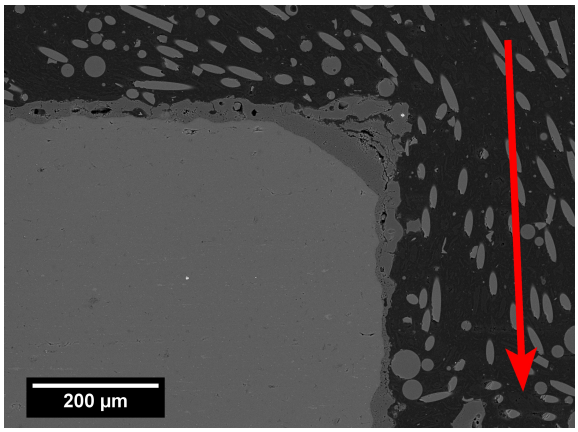

(d) The cross section at the centre-point of a hole, from a sample processed for 60 minutes in fibre-free electrolyte, with jetting in the direction of the red arrow.

Fig. 7.12 BSE micrographs of Al coatings processed for 60 minutes, showing the effect of fibre addition and jetting on coating morphology.

higher concentration of Al was observed around the rime of each drilled hole, at the face of the plate normal to the flow. This behaviour mirrors what was observed in the same case on the Al substrate (see Figure 7.12c), in that a higher concentration of fibres is observed at the edges of the hole.

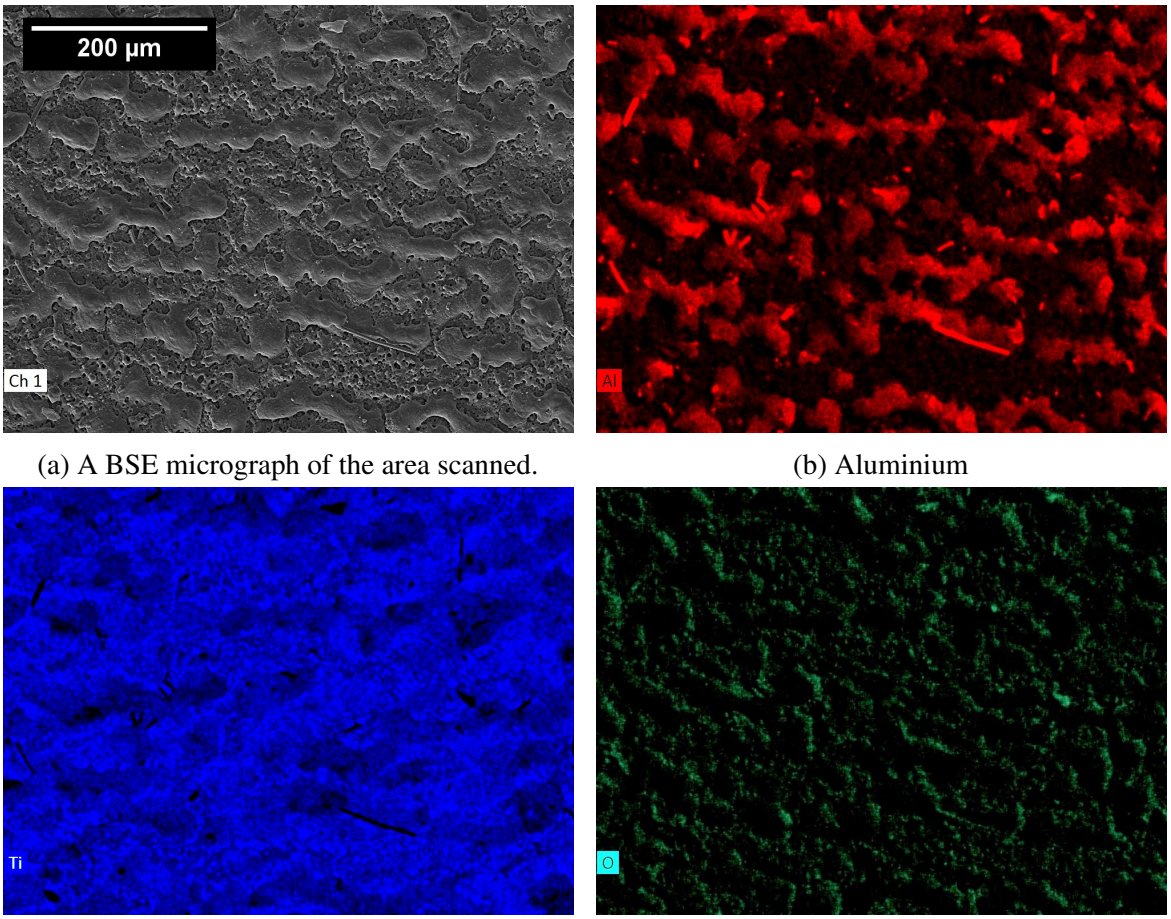

(a) A BSE micrograph of the area scanned.

(b) Aluminium

(c) Titanium

(d) Oxygen

Fig. 7.13 A BSE micrograph and corresponding elemental composition maps of the free surface of a Ti coating, processed for 30 minutes in electrolyte containing 4 g L^{-1} Saffil fibres, which was jetted at parallel to the thin edge of the sample, causing electrolyte flow parallel to the surface. Only elements with an overall composition of more than 5% were included. Jetting flow is from left to right.

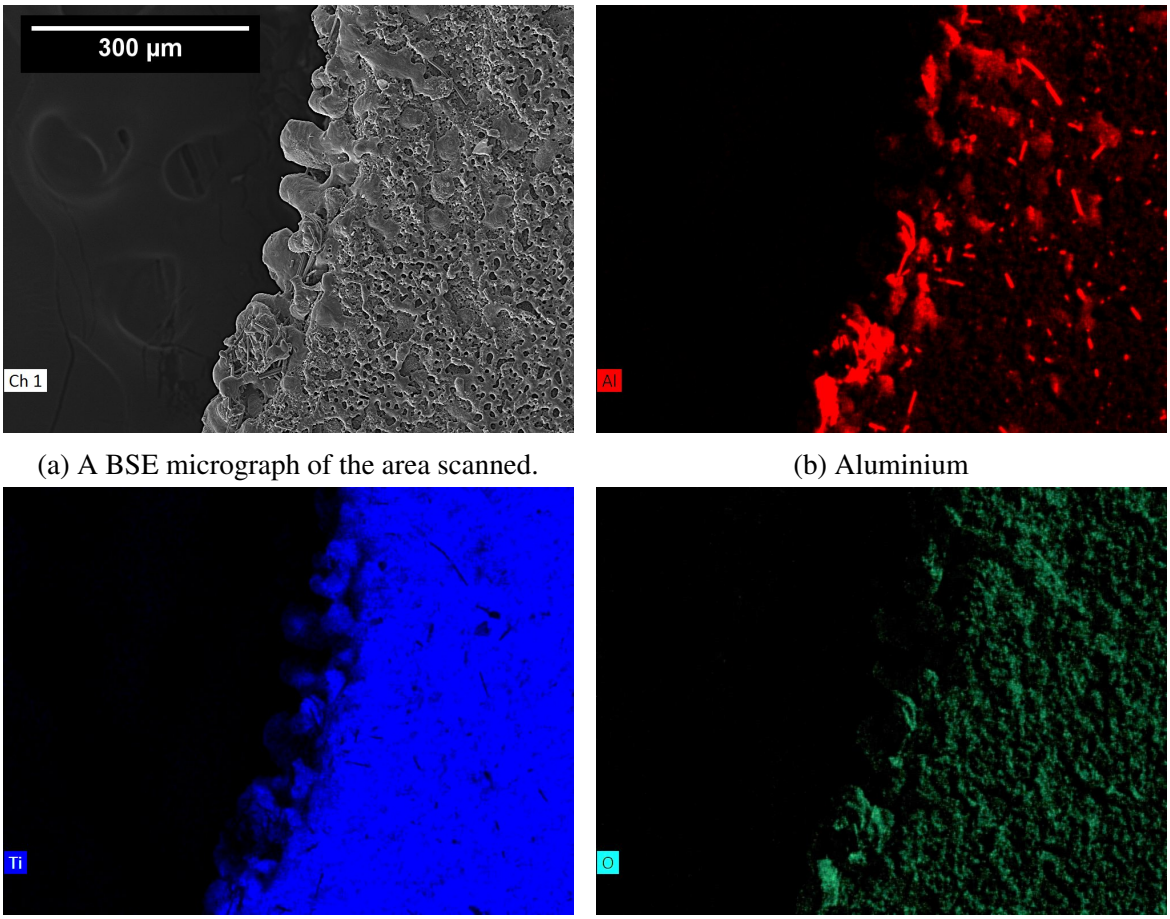

(a) A BSE micrograph of the area scanned.

(b) Aluminium

(c) Titanium

(d) Oxygen

Fig. 7.14 A BSE micrograph and corresponding elemental composition maps of a section of the centreline hole of a Ti sample, processed for 30 minutes in electrolyte containing 4 g L^{-1} Saffil fibres, which was jetted normal to the plane of the circular hole, causing electrolyte flow normal to the surface. The flow direction was into the page. Only elements with an overall composition of more than 5% were included.

7.7 Summary

In this study, alumina fibres of diameter 3 μm were successfully incorporated into Al and Ti substrates, by adding them to the electrolyte. The nature of their incorporation into the Al coating was difficult to elucidate due to the chemical similarity of the two materials concerned, but on Ti, it was shown that fibres were incorporated reactively to form mounds of (predominantly) Al_2TiO_5 across the surface. A mechanism for this incorporation was proposed, in that fibres were likely to become entrapped in molten oxide around active discharge pores. Subsequent discharging would then cause melting of the fibre. It was found that the introduction of fibre to the electrolyte had no significant effect on the electrical response of the system.

In an attempt to increase the amount of fibres incorporated, the electrolyte was jetted at the sample in two orientations: initially parallel to the face of the sample and secondly perpendicular to a sample with through-holes drilled into the surface. It was found that, even without fibre in the electrolyte, the morphology of the free surface was altered by jetting across the sample. On Al substrates, the nominally circular 'pancakes' of solidified oxide were distorted into an oblong shape, elongated in the direction of jetting, strongly suggesting that the molten oxide was being distorted by viscous forces due to jetting. On Ti the effect was even more significant, thin strata were observed across the surface, aligned parallel to the jet of electrolyte. When fibre was introduced to the jetted electrolyte stream, a number of effects were observed. On the through-hole jetted samples, it was seen that fibre tended to build up along the entrant edge of each drilled hole. This was attributed to the trapping of fibres by molten oxide flow through the drilled hole. On 'side-jetted' Al samples, an increased amount of free, unmelted fibres were observed on the surface, clumped together by oxide material. It is not clear if this oxide originated from the fibres themselves or the coating. In any case, it was determined that they did not account for a substantial proportion

of sample mass, as no δ alumina was present in the XRD spectra. On Ti samples jetted in this configuration, it was observed that the strata formed were rich in Al, but the overall mass gain was virtually unchanged from the unjetted case. Jetting, in this context, appeared to provide a more uniform distribution of fibre distribution.

Chapter 8

Conclusions

8.1 Comparison of PEO Processing Characteristics of Al, Mg and Ti substrates

Al, Mg and Ti remain the most common substrates for use as PEO coatings, although systematic comparisons about their processing cannot be made based on current academic and industrial knowledge. This is due to the highly empirical nature of the current work on PEO coatings

a) Differences in the processing characteristics of the three most common substrates for PEO processing, namely Al, Mg and Ti, were examined at the macroscopic and individual discharge level. The substrates were processed under identical electrical conditions, and using electrolytes with similar pH and conductivity values. The electrolytes were chosen so as to produce a coating composed primarily of the substrate oxide for each substrate.

b) Applied voltage traces were recorded for fixed-current processing, for a duration of 30 minutes for each substrate. It was shown that for the same current density, the Ti substrate required an applied voltage 150-200 V lower than that which was required for the other two substrates. As dielectric breakdown is occurring over a similar thickness of oxide (at the base of a pore) for each substrate, it was concluded that this is due in part to the low bandgap of TiO_2, which is also a cause of lower discharge intensity on Ti substrates.

c) The mass gain for Ti is linear only in the first 3-4 minutes of processing, although discharges appear to generate as normal as the process is allowed to progress past this point, until the growth rate becomes linearly negative. This was linked to the ease of charge transfer through the titania coating under anodic potential, leading ultimately to a lower charge build-up at the oxide-substrate barrier and weaker discharges.

d) Mg and Ti discharges were shown to occur in cascades; i.e. discharges tend to persist in one location repeatedly. This behaviour had previously been shown to occur during processing of Al substrates, and demonstrates that the underlying mechanism of discharging is no different for Mg and Ti than it is for Al.

8.2 Incorporation of Small Particles Suspended in the Electrolyte

A series of PEO experiments have been carried out, with or without different levels of suspended particulate (covering a wide size range) in the electrolyte. The following conclusions can be drawn from this work.

a) Measurements of mass gain during the process have indicated that the presence of such particulate can give enhanced rates of mass gain (and correspondingly thicker coatings), provided the particulate is relatively small (around a few microns or below) and well-dispersed.

b) Microstructural examinations have confirmed that, for cases of enhanced rates of mass gain, the particulate has become incorporated into the coating. In some cases, they have undergone little or no phase change during the process, but in others there has been extensive chemical reaction, with new phases formed (as a consequence of being taken to high temperatures during the process).

c) These studies, in combination with estimates of the forces acting on individual particles and the nature of convective flow during the process, have indicated that the main mechanism of incorporation is the sweeping of suspended particulate into active discharge sites immediately after plasma collapse. They then become heated during the next discharge cycle, potentially leading to chemical reaction and phase changes. It is shown that electrophoretic forces are unlikely to influence particle motion during the key processes or to contribute significantly to the incorporation of particles into coatings. Particles may, however, decorate the free surface of a coating fairly uniformly at the end of the process, as a result of simple sedimentation, and possibly electrostatic forces could assist this adhesion.

d) It may be noted that it is already established that this variant of the PEO process has considerable potential for promoting beneficial effects, including improved coating microstructure (with lower porosity and defect levels) and reduced energy consumption (for a coating of given thickness). The results presented here may be helpful in providing some guidance about how such processing could be optimised.

8.3 Incorporation of Alumina Fibres Suspended in the Electrolyte

Experiments have been performed in the current work which present the possibility of incorporating relatively high aspect ratio alumina fibres into aluminium and titanium coatings. The main conclusions of this work are as follows:

a) Mass gain measurements have shown that fibre incorporation does occur on both Al and Ti, provided that the fibre is sufficiently well-dispersed in the electrolyte (conventional electrolyte re-circulation is sufficient for this). The absolute mass gain for the two substrates was similar when the fibre was added to the electrolyte, indicating a similar amount of fibre uptake for both.

b) On Ti substrates, fibre was shown to incorporate reactively to form aluminium titanium oxide (Al_2TiO_5), using evidence from XRD spectra. EDX maps indicated that Al atoms were concentrated in 'mound' structures visible on the surface of the coating. Using this information, a mechanism for the incorporation of high aspect ratio fibres was proposed, based on fibres becoming trapped in molten oxide at, or close to, active discharge sites.

c) Direct jetting of electrolyte across the face of the sample, in the absence of electrolyte addition, had the effect of distorting the resultant microstructure of the coatings. On Al samples, it was shown that nominally circular melt pools were now oblong in shape, with evidence of the molten oxide having been acted upon by viscous forces due to the electrolyte flow over the surface. On Ti samples, well-defined strata of oxide were shown to form, elongated in the direction of electrolyte flow.

d) The absolute mass gain when fibre-containing electrolyte was jetted across the face of the sample was unchanged for Ti substrate, but for Al was slightly increased. Microscopy showed that, on Al, there was an increase in the amount of in-tact (i.e. unmelted) fibres on the surface, which appeared to be bound together by molten oxide. When electrolyte was jetted through holes drilled into the samples, it was found that fibres were more easily trapped around the entrant edge of the drilled hole. When viewed in section, it was found that these fibres were trapped by an outcrop of coating material, likely forced into that position while molten by jetting forces.

e) The electrical response of the system was unchanged by either the addition of fibres to the electrolyte or the introduction of electrolyte jetting.

8.4 Future Work

There is considerable scope for future work to further elucidate the clear differences between the PEO processing of Ti and the other two substrates. For example, electrical data has shown that discharges on Ti substrates are of a similar form to those on Al or Mg in that they have the same general current-time profile, but are simply of lower intensity. This work has also shown that cascades occur on Ti coatings. Their surface morphology, however, is quite different to either Al or Mg. This could be due to a difference in how discharges form on Ti coatings and could be investigated further using methods outlined here, for example by studying the morphology of the small area sample after a discharge (of known current and position) occurs on it.

Further investigations of particle and fibre incorporation into PEO coatings would be very useful to determine why some particle types appear to incorporate inertly and others reactively (given that the local temperatures during processing are much higher than the

melting point of most additives). This study could be performed using relatively common techniques such as time-resolved optical emission spectroscopy.

A study to increase the amount of fibres incorporated into PEO coatings would be of considerable interest. Computational methods could be employed to better quantify and characterise electrolyte flow around the sample, in order to deliver fibres to the surface and incorporate them effectively. A range of fibre geometries and compositions could also be used to increase the absolute mass gain.

References

[1] J. Curran and T. Clyne, "Thermo-physical properties of plasma electrolytic oxide coatings on aluminium," *SURFACE & COATINGS TECHNOLOGY*, vol. 199, pp. 168–176, SEP 22 2005. EUROMAT 2003 Congress on Advanced Materials and Processes, Lausanne, SWITZERLAND, SEP 01-05, 2003.

[2] J. Curran and T. Clyne, "Porosity in plasma electrolytic oxide coatings," *Acta Materialia*, vol. 54, no. 7, pp. 1985 – 1993, 2006.

[3] J. Wheeler, C. Collier, J. Paillard, and J. Curran, "Evaluation of micromechanical behaviour of plasma electrolytic oxidation (peo) coatings on ti–6al–4v," *Surface and Coatings Technology*, vol. 204, no. 21, pp. 3399 – 3409, 2010.

[4] C. Martini, L. Ceschini, F. Tarterini, J. Paillard, and J. Curran, "Peo layers obtained from mixed aluminate–phosphate baths on ti–6al–4v: Dry sliding behaviour and influence of a ptfe topcoat," *Wear*, vol. 269, no. 11, pp. 747 – 756, 2010.

[5] M. Khorasanian, A. Dehghan, M. Shariat, M. Bahrololoom, and S. Javadpour, "Microstructure and wear resistance of oxide coatings on ti–6al–4v produced by plasma electrolytic oxidation in an inexpensive electrolyte," *Surface and coatings Technology*, vol. 206, no. 6, pp. 1495–1502, 2011.

[6] C. Blawert, W. Dietzel, E. Ghali, and G. Song, "Anodizing treatments for magnesium alloys and their effecton corrosion resistance in various environments," *ADVANCED ENGINEERING MATERIALS*, vol. 8, pp. 511–533, JUN 2006.

[7] T. Wei, F. Yan, and J. Tian, "Characterization and wear- and corrosion-resistance of microarc oxidation ceramic coatings on aluminum alloy," *JOURNAL OF ALLOYS AND COMPOUNDS*, vol. 389, pp. 169–176, MAR 8 2005.

[8] X. Nie, E. Meletis, J. Jiang, A. Leyland, A. Yerokhin, and A. Matthews, "Abrasive wear/corrosion properties and TEM analysis of Al2O3 coatings fabricated using plasma electrolysis," *SURFACE & COATINGS TECHNOLOGY*, vol. 149, pp. 245–251, JAN 15 2002.

[9] H. Robinson, A. Markaki, C. Collier, and T. Clyne, "Cell adhesion to plasma electrolytic oxidation (peo) titania coatings, assessed using a centrifuging technique," *Journal of the Mechanical Behavior of Biomedical Materials*, vol. 4, no. 8, pp. 2103 – 2112, 2011. Special Issue Soft Tissues.

[10] A. Kopp, R. Smeets, O. Jung, N. Kröger, and A. Klink, "Defined surface adjustment for medical magnesium implants by electrical discharge machining (edm) and plasma electrolytic oxidation (peo)," *CIRP Annals*, vol. 68, no. 1, pp. 583 – 586, 2019.

[11] X. Rao, J. Li, X. Feng, and C. Chu, "Bone-like apatite growth on controllable macroporous titanium scaffolds coated with microporous titania," *Journal of the Mechanical Behavior of Biomedical Materials*, vol. 77, pp. 225 – 233, 2018.

[12] S. Riaz and S.-J. Park, "An overview of tio2-based photocatalytic membrane reactors for water and wastewater treatments," *Journal of Industrial and Engineering Chemistry*, 2019.

[13] M. Coto, S. Troughton, J. Duan, R. Kumar, and T. Clyne, "Development and assessment of photo-catalytic membranes for water purification using solar radiation," *Applied Surface Science*, vol. 433, pp. 101 – 107, 2018.

[14] Y. Chen, X. Lu, C. Blawert, M. L. Zheludkevich, T. Zhang, and F. Wang, "Formation of self-lubricating peo coating via in-situ incorporation of ptfe particles," *Surface and Coatings Technology*, vol. 337, pp. 379–388, 2018.

[15] M.-A. Faghihi-Sani, A. Arbabi, and A. Mehdinezhad-Roshan, "Crystallization of hydroxyapatite during hydrothermal treatment on amorphous calcium phosphate layer coated by peo technique," *Ceramics International*, vol. 39, no. 2, pp. 1793–1798, 2013.

[16] Y. Gao, A. Yerokhin, and A. Matthews, "Mechanical behaviour of cp-magnesium with duplex hydroxyapatite and peo coatings," *Materials Science and Engineering: C*, vol. 49, pp. 190–200, 2015.

[17] S. Durdu, Ö. F. Deniz, I. Kutbay, and M. Usta, "Characterization and formation of hydroxyapatite on ti6al4v coated by plasma electrolytic oxidation," *Journal of Alloys and Compounds*, vol. 551, pp. 422–429, 2013.

[18] S. Durdu, S. Bayramoğlu, A. Demirtaş, M. Usta, and A. H. Üçışık, "Characterization of az31 mg alloy coated by plasma electrolytic oxidation," *Vacuum*, vol. 88, pp. 130–133, 2013.

[19] X. Jiang, Y. Wang, and C. Pan, "Micro-arc oxidation of tc4 substrates to fabricate tio2/yag: Ce3+ compound films with enhanced photocatalytic activity," *Journal of Alloys and Compounds*, vol. 509, no. 8, pp. L137–L141, 2011.

[20] M. Aliofkhazraei, R. S. Gharabagh, M. Teimouri, M. Ahmadzadeh, G. B. Darband, and H. Hasannejad, "Ceria embedded nanocomposite coating fabricated by plasma electrolytic oxidation on titanium," *Journal of Alloys and Compounds*, vol. 685, pp. 376 – 383, 2016.

[21] S. K. Lee, S. B. Lee, S. Y. Park, Y. S. Yi, and C. W. Ahn, "Structure of amorphous aluminum oxide," *Physical Review Letters*, vol. 103, no. 9, p. 095501, 2009.

[22] S. Xin, L. Song, R. Zhao, and X. Hu, "Influence of cathodic current on composition, structure and properties of al2o3 coatings on aluminum alloy prepared by micro-arc oxidation process," *Thin Solid Films*, vol. 515, no. 1, pp. 326 – 332, 2006. INTERNATIONAL CONFERENCE ON SURFACES, COATINGS AND NANOSTRUCTURED MATERIALS.

[23] P. Su, X. Wu, Y. Guo, and Z. Jiang, "Effects of cathode current density on structure and corrosion resistance of plasma electrolytic oxidation coatings formed on zk60 mg alloy," *Journal of Alloys and Compounds*, vol. 475, no. 1-2, pp. 773–777, 2009.

[24] Q. Li, J. Liang, B. Liu, Z. Peng, and Q. Wang, "Effects of cathodic voltages on structure and wear resistance of plasma electrolytic oxidation coatings formed on aluminium alloy," *Applied Surface Science*, vol. 297, pp. 176–181, 2014.

[25] A. B. Rogov, A. Yerokhin, and A. Matthews, "The role of cathodic current in plasma electrolytic oxidation of aluminum: Phenomenological concepts of the "soft sparking" mode," *Langmuir*, vol. 33, no. 41, pp. 11059–11069, 2017.

[26] J. Curran, *Thermal and Mechanical Properties of Plasma Electrolytic Oxide Coatings*. PhD thesis, University of Cambridge, 2005.

[27] J. Liang, P. B. Srinivasan, C. Blawert, and W. Dietzel, "Influence of ph on the deterioration of plasma electrolytic oxidation coated am50 magnesium alloy in nacl solutions," *Corrosion Science*, vol. 52, no. 2, pp. 540–547, 2010.

[28] P. B. Srinivasan, J. Liang, C. Blawert, and W. Dietzel, "Dry sliding wear behaviour of magnesium oxide and zirconium oxide plasma electrolytic oxidation coated magnesium alloy," *Applied Surface Science*, vol. 256, no. 10, pp. 3265–3273, 2010.

[29] J. Liang, P. B. Srinivasan, C. Blawert, and W. Dietzel, "Comparison of electrochemical corrosion behaviour of mgo and zro2 coatings on am50 magnesium alloy formed by plasma electrolytic oxidation," *Corrosion Science*, vol. 51, no. 10, pp. 2483–2492, 2009.

[30] Z. Yao, H. Gao, Z. Jiang, and F. Wang, "Structure and properties of zro2 ceramic coatings on az91d mg alloy by plasma electrolytic oxidation," *Journal of the American Ceramic Society*, vol. 91, no. 2, pp. 555–558, 2008.

[31] A. Yerokhin, X. Nie, A. Leyland, A. Matthews, and S. Dowey, "Plasma electrolysis for surface engineering," *Surface and coatings technology*, vol. 122, no. 2-3, pp. 73–93, 1999.

[32] M. Sieber, F. Simchen, R. Morgenstern, I. Scharf, and T. Lampke, "Plasma electrolytic oxidation of high-strength aluminium alloys—substrate effect on wear and corrosion performance," *Metals*, vol. 8, no. 5, 2018.

[33] S. Wang and P. Liu, "The technology of preparing green coating by conducting micro-arc oxidation on az91d magnesium alloy," *Polish Journal of Chemical Technology*, vol. 18, no. 4, pp. 36 – 40, 2016.

[34] Y. Jiang, J. Wang, B. Hu, Z. Yao, Q. Xia, and Z. Jiang, "Preparation of a novel yellow ceramic coating on ti alloys by plasma electrolytic oxidation," *Surface and Coatings Technology*, vol. 307, pp. 1297–1302, 2016.

[35] W. Yang, J. Wang, D. Xu, J. Li, and T. Chen, "Characterization and formation mechanism of grey micro-arc oxidation coatings on magnesium alloy," *Surface and Coatings Technology*, vol. 283, pp. 281–285, 2015.

[36] Z. Shao, Q. Zhang, L. Yang, M. Wang, and H. Gao, "Preparation of dark-red membrane by micro-arc oxidation on am50 alloys," *Materials and Manufacturing Processes*, vol. 30, no. 12, pp. 1505–1509, 2015.

[37] Z. Wang, X. Nie, H. Hu, and R. O. Hussein, "In situ fabrication of blue ceramic coatings on wrought al alloy 2024 by plasma electrolytic oxidation," *Journal of Vacuum Science & Technology A: Vacuum, Surfaces, and Films*, vol. 30, no. 2, p. 021302, 2012.

[38] Q. Dou, W. Li, G. Zhang, and X. Wan, "Preparation and characterisation of black ceramic coating on az91d magnesium alloy by plasma electrolytic oxidation with reduced energy consumption," *Materials Research Innovations*, vol. 19, no. sup2, pp. S2–23, 2015.

[39] J. Martin, P. Leone, A. Nominé, D. Veys-Renaux, G. Henrion, and T. Belmonte, "Influence of electrolyte ageing on the plasma electrolytic oxidation of aluminium," *Surface and Coatings Technology*, vol. 269, pp. 36 – 46, 2015. Special Issue on Plasma Electrolysis: Progress in Science, Technology and Applications of Electrolytic Plasma Surface Treatments and Coatings.

[40] X. Lu, M. Mohedano, C. Blawert, E. Matykina, R. Arrabal, K. U. Kainer, and M. L. Zheludkevich, "Plasma electrolytic oxidation coatings with particle additions–a review," *Surface and Coatings Technology*, vol. 307, pp. 1165–1182, 2016.

[41] C. Dunleavy, I. Golosnoy, J. Curran, and T. Clyne, "Characterisation of discharge events during plasma electrolytic oxidation," *Surface and Coatings Technology*, vol. 203, no. 22, pp. 3410–3419, 2009.

[42] H. Duan, C. Yan, and F. Wang, "Growth process of plasma electrolytic oxidation films formed on magnesium alloy az91d in silicate solution," *Electrochimica Acta*, vol. 52, no. 15, pp. 5002–5009, 2007.

[43] H. Duan, C. Yan, and F. Wang, "Effect of electrolyte additives on performance of plasma electrolytic oxidation films formed on magnesium alloy az91d," *Electrochimica Acta*, vol. 52, no. 11, pp. 3785–3793, 2007.

[44] J. Liang, P. B. Srinivasan, C. Blawert, M. Störmer, and W. Dietzel, "Electrochemical corrosion behaviour of plasma electrolytic oxidation coatings on am50 magnesium alloy formed in silicate and phosphate based electrolytes," *Electrochimica Acta*, vol. 54, no. 14, pp. 3842–3850, 2009.

[45] L. Wang, L. Chen, Z. Yan, H. Wang, and J. Peng, "Effect of potassium fluoride on structure and corrosion resistance of plasma electrolytic oxidation films formed on az31 magnesium alloy," *Journal of Alloys and Compounds*, vol. 480, no. 2, pp. 469–474, 2009.

[46] R. Arrabal, E. Matykina, F. Viejo, P. Skeldon, G. Thompson, and M. Merino, "Ac plasma electrolytic oxidation of magnesium with zirconia nanoparticles," *Applied Surface Science*, vol. 254, no. 21, pp. 6937–6942, 2008.

[47] A. Yerokhin, X. Nie, A. Leyland, and A. Matthews, "Characterisation of oxide films produced by plasma electrolytic oxidation of a Ti-6Al-4V alloy," *SURFACE & COATINGS TECHNOLOGY*, vol. 130, pp. 195–206, AUG 21 2000.

[48] E. Matykina, A. Berkani, P. Skeldon, and G. Thompson, "Real-time imaging of coating growth during plasma electrolytic oxidation of titanium," *Electrochimica Acta*, vol. 53, no. 4, pp. 1987–1994, 2007.

[49] E. Matykina, R. Arrabal, P. Skeldon, and G. Thompson, "Transmission electron microscopy of coatings formed by plasma electrolytic oxidation of titanium," *Acta biomaterialia*, vol. 5, no. 4, pp. 1356–1366, 2009.

[50] S. Stojadinović, R. Vasilić, M. Petković, B. Kasalica, I. Belča, A. Žekić, and L. Zeković, "Characterization of the plasma electrolytic oxidation of titanium in sodium metasilicate," *Applied surface science*, vol. 265, pp. 226–233, 2013.

[51] J. Martin, A. Melhem, I. Shchedrina, T. Duchanoy, A. Nomine, G. Henrion, T. Czerwiec, and T. Belmonte, "Effects of electrical parameters on plasma electrolytic oxidation of aluminium," *Surface and Coatings Technology*, vol. 221, pp. 70–76, 2013.

[52] G. Sundararajan and L. R. Krishna, "Mechanisms underlying the formation of thick alumina coatings through the mao coating technology," *Surface and Coatings Technology*, vol. 167, no. 2-3, pp. 269–277, 2003.

[53] E. Tillous, T. Toll-Duchanoy, and E. Bauer-Grosse, "Microstructure and 3d microtomographic characterization of porosity of mao surface layers formed on aluminium and 2214-t6 alloy," *Surface and Coatings Technology*, vol. 203, no. 13, pp. 1850–1855, 2009.

[54] R. Arrabal, E. Matykina, T. Hashimoto, P. Skeldon, and G. Thompson, "Characterization of ac peo coatings on magnesium alloys," *Surface and Coatings Technology*, vol. 203, no. 16, pp. 2207–2220, 2009.

[55] X. Nie, E. Meletis, J. Jiang, A. Leyland, A. Yerokhin, and A. Matthews, "Abrasive wear/corrosion properties and tem analysis of al2o3 coatings fabricated using plasma electrolysis," *Surface and Coatings Technology*, vol. 149, no. 2-3, pp. 245–251, 2002.

[56] X. Zhang, S. Aliasghari, A. Němcová, T. L. Burnett, I. Kuběna, M. Smid, G. E. Thompson, P. Skeldon, and P. J. Withers, "X-ray computed tomographic investigation of the porosity and morphology of plasma electrolytic oxidation coatings," *ACS applied materials & interfaces*, vol. 8, no. 13, pp. 8801–8810, 2016.

[57] J. Curran, H. Kalkancı, Y. Magurova, and T. Clyne, "Mullite-rich plasma electrolytic oxide coatings for thermal barrier applications," *Surface and Coatings Technology*, vol. 201, no. 21, pp. 8683–8687, 2007.

[58] A. Friedemann, T. M. Gesing, and P. Plagemann, "Electrochemical rutile and anatase formation on peo surfaces," *Surface and Coatings Technology*, vol. 315, pp. 139–149, 2017.

[59] M. Sowa and W. Simka, "Electrochemical impedance and polarization corrosion studies of tantalum surface modified by dc plasma electrolytic oxidation," *Materials*, vol. 11, no. 4, p. 545, 2018.

[60] S. Stojadinović, J. Jovović, M. Petković, R. Vasilić, and N. Konjević, "Spectroscopic and real-time imaging investigation of tantalum plasma electrolytic oxidation (peo)," *Surface and Coatings Technology*, vol. 205, no. 23-24, pp. 5406–5413, 2011.

[61] M. Petković, S. Stojadinović, R. Vasilić, and L. Zeković, "Characterization of oxide coatings formed on tantalum by plasma electrolytic oxidation in 12-tungstosilicic acid," *Applied Surface Science*, vol. 257, no. 24, pp. 10590–10594, 2011.

[62] K. Rokosz, T. Hryniewicz, P. Chapon, S. Raaen, and H. Ricardo Zschommler Sandim, "Xps and gdoes characterization of porous coating enriched with copper and calcium obtained on tantalum via plasma electrolytic oxidation," *Journal of Spectroscopy*, vol. 2016, 2016.

[63] M. Sowa, A. Kazek-Kęsik, R. P. Socha, G. Dercz, J. Michalska, and W. Simka, "Modification of tantalum surface via plasma electrolytic oxidation in silicate solutions," *Electrochimica Acta*, vol. 114, pp. 627–636, 2013.

[64] I. Lukiyanchuk, V. Rudnev, and L. Tyrina, "Plasma electrolytic oxide layers as promising systems for catalysis," *Surface and Coatings Technology*, vol. 307, pp. 1183–1193, 2016.

[65] B. L. Pereira, A. R. da Luz, C. M. Lepienski, I. Mazzaro, and N. K. Kuromoto, "Niobium treated by plasma electrolytic oxidation with calcium and phosphorus electrolytes," *Journal of the mechanical behavior of biomedical materials*, vol. 77, pp. 347–352, 2018.

[66] M. Sowa, A. Kazek-Kęsik, A. Krząkała, R. P. Socha, G. Dercz, J. Michalska, and W. Simka, "Modification of niobium surfaces using plasma electrolytic oxidation in silicate solutions," *Journal of Solid State Electrochemistry*, vol. 18, no. 11, pp. 3129–3142, 2014.

[67] E. Matykina, R. Arrabal, P. Skeldon, G. Thompson, P. Wang, and P. Wood, "Plasma electrolytic oxidation of a zirconium alloy under ac conditions," *Surface and Coatings Technology*, vol. 204, no. 14, pp. 2142–2151, 2010.

[68] W. Xue, Q. Zhu, Q. Jin, and M. Hua, "Characterization of ceramic coatings fabricated on zirconium alloy by plasma electrolytic oxidation in silicate electrolyte," *Materials Chemistry and Physics*, vol. 120, no. 2-3, pp. 656–660, 2010.

[69] S. He, Y. Ma, H. Ye, X. Liu, Z. Dou, Q. Xu, H. Wang, and P. Zhang, "Ceramic oxide coating formed on beryllium by micro-arc oxidation," *Corrosion Science*, vol. 122, pp. 108–117, 2017.

[70] Z. Li, Y. Cheng, S. hang Kang, W. Tu, and Y. Cheng, "A re-understanding of the breakdown theory from the study of the plasma electrolytic oxidation of a carbon steel — a non-valve metal," *Electrochimica Acta*, vol. 284, pp. 681 – 695, 2018.

[71] S. Stojadinović, R. Vasilić, and M. Perić, "Investigation of plasma electrolytic oxidation on valve metals by means of molecular spectroscopy–a review," *RSC Advances*, vol. 4, no. 49, pp. 25759–25789, 2014.

[72] A. Michaelis, *Valve Metal, Si and Ceramic Oxides as Dielectric Films for Passive and Active Electronic Devices*, ch. 1, pp. 1–106. John Wiley & Sons, Ltd, 2008.

[73] T. Hurlen and E. Gulbrandsen, "Growth of anodic films on valve metals," *Electrochimica Acta*, vol. 39, no. 14, pp. 2169 – 2172, 1994.

[74] T. W. Clyne and S. C. Troughton, "A review of recent work on discharge characteristics during plasma electrolytic oxidation of various metals," *International Materials Reviews*, vol. 64, no. 3, pp. 127–162, 2019.

[75] W. Strehlow and E. Cook, "Compilation of energy band gaps in elemental and binary compound semiconductors and insulators," *Journal of Physical and Chemical Reference Data*, vol. 2, no. 1, pp. 163–200, 1973.

[76] A. T. Fromhold Jr and E. L. Cook, "Kinetics of oxide film growth on metal crystals: electron tunneling and ionic diffusion," *Physical Review*, vol. 158, no. 3, p. 600, 1967.

[77] S. Troughton, A. Nominé, J. Dean, and T. W. Clyne, "Effect of individual discharge cascades on the microstructure of plasma electrolytic oxidation coatings," *Applied Surface Science*, vol. 389, pp. 260–269, 2016.

[78] Y. Aiura, Y. Nishihara, Y. Haruyama, T. Komeda, S. Kodaira, Y. Sakisaka, T. Maruyama, and H. Kato, "Effects of surface oxygen vacancies on electronic states of tio2 (110), tio2 (001) and srtio3 (001) surfaces," *Physica B: Condensed Matter*, vol. 194, pp. 1215–1216, 1994.

[79] R. Sanjines, H. Tang, H. Berger, F. Gozzo, G. Margaritondo, and F. Levy, "Electronic structure of anatase tio2 oxide," *Journal of Applied Physics*, vol. 75, no. 6, pp. 2945–2951, 1994.

[80] W. S. Epling, C. H. Peden, M. A. Henderson, and U. Diebold, "Evidence for oxygen adatoms on tio2 (110) resulting from o2 dissociation at vacancy sites," *Surface science*, vol. 412, pp. 333–343, 1998.

[81] M. Chase Jr, C. Davies, J. Downey Jr, D. Frurip, R. McDonald, and A. Syverud, "Janaf thermochemical tables, (1985)," *J. Phys. Chem. Ref. Data*, vol. 14, 1985.

[82] T. B. Reed, *Free energy of formation of binary compounds: an atlas of charts for high-temperature chemical calculations*. Mit Press Cambridge, MA, 1971.

[83] N. Klein, V. Moskovici, and V. Kadary, "Electrical breakdown: Ii. during the anodic growth of aluminum oxide," *Journal of the Electrochemical Society*, vol. 127, no. 1, p. 152, 1980.

[84] V. Kadary and N. Klein, "Electrical breakdown: I. during the anodic growth of tantalum pentoxide," *Journal of the Electrochemical Society*, vol. 127, no. 1, p. 139, 1980.

[85] C. Dunleavy, J. Curran, and T. Clyne, "Time dependent statistics of plasma discharge parameters during bulk ac plasma electrolytic oxidation of aluminium," *Applied Surface Science*, vol. 268, pp. 397–409, 2013.

[86] C. Dunleavy, J. Curran, and T. Clyne, "Self-similar scaling of discharge events through peo coatings on aluminium," *Surface and Coatings Technology*, vol. 206, no. 6, pp. 1051–1061, 2011.

[87] A. Nominé, S. Troughton, A. Nominé, G. Henrion, and T. W. Clyne, "High speed video evidence for localised discharge cascades during plasma electrolytic oxidation," *Surface and Coatings Technology*, vol. 269, pp. 125–130, 2015.

[88] A. Nominé, A. V. Nominé, N. S. J. Braithwaite, T. Belmonte, and G. Henrion, "High-frequency-induced cathodic breakdown during plasma electrolytic oxidation," *Physical Review Applied*, vol. 8, no. 3, p. 031001, 2017.

[89] S. Troughton and T. W. Clyne, "Cathodic discharges during high frequency plasma electrolytic oxidation," *Surface and Coatings Technology*, vol. 352, pp. 591–599, 2018.

[90] S. P. Sah, E. Tsuji, Y. Aoki, and H. Habazaki, "Cathodic pulse breakdown of anodic films on aluminium in alkaline silicate electrolyte–understanding the role of cathodic half-cycle in ac plasma electrolytic oxidation," *Corrosion Science*, vol. 55, pp. 90–96, 2012.

[91] A. Nomine, J. Martin, G. Henrion, and T. Belmonte, "Effect of cathodic micro-discharges on oxide growth during plasma electrolytic oxidation (peo)," *Surface and Coatings Technology*, vol. 269, pp. 131–137, 2015.

[92] A. Rakoch, A. Gladkova, Z. Linn, and D. Strekalina, "The evidence of cathodic micro-discharges during plasma electrolytic oxidation of light metallic alloys and micro-discharge intensity depending on ph of the electrolyte," *Surface and coatings technology*, vol. 269, pp. 138–144, 2015.

[93] A. Nomine, J. Martin, C. Noel, G. Henrion, T. Belmonte, I. Bardin, V. Kovalev, and A. Rakoch, "The evidence of cathodic micro-discharges during plasma electrolytic oxidation process," *Applied Physics Letters*, vol. 104, no. 8, p. 081603, 2014.

[94] Y. Toriyabe, S. Watanabe, S. Yatsu, T. Shibayama, and T. Mizuno, "Controlled formation of metallic nanoballs during plasma electrolysis," *Applied physics letters*, vol. 91, no. 4, p. 041501, 2007.

[95] A. R. Fatkullin, E. V. Parfenov, A. Yerokhin, D. M. Lazarev, and A. Matthews, "Effect of positive and negative pulse voltages on surface properties and equivalent circuit of the plasma electrolytic oxidation process," *Surface and Coatings Technology*, vol. 284, pp. 427–437, 2015.

[96] J.-H. Wang, M.-H. Du, F.-Z. Han, and J. Yang, "Effects of the ratio of anodic and cathodic currents on the characteristics of micro-arc oxidation ceramic coatings on al alloys," *Applied surface science*, vol. 292, pp. 658–664, 2014.

[97] D.-S. Tsai, G.-W. Chen, and C.-C. Chou, "Probe the micro arc softening phenomenon with pulse transient analysis in plasma electrolytic oxidation," *Surface and Coatings Technology*, vol. 357, pp. 235–243, 2019.

[98] A. Nominé, J. Martin, C. Noel, G. Henrion, T. Belmonte, I. V. Bardin, and P. Lukes, "Surface charge at the oxide/electrolyte interface: toward optimization of electrolyte composition for treatment of aluminum and magnesium by plasma electrolytic oxidation," *Langmuir*, vol. 32, no. 5, pp. 1405–1409, 2016.

[99] E. Matykina, R. Arrabal, P. Skeldon, and G. Thompson, "Optimisation of the plasma electrolytic oxidation process efficiency on aluminium," *Surface and Interface Analysis: An International Journal devoted to the development and application of techniques for the analysis of surfaces, interfaces and thin films*, vol. 42, no. 4, pp. 221–226, 2010.

[100] J. Martin, A. Nominé, V. Ntomprougkidis, S. Migot, S. Bruyère, F. Soldera, T. Belmonte, and G. Henrion, "Formation of a metastable nanostructured mullite during plasma electrolytic oxidation of aluminium in "soft" regime condition," *Materials & Design*, vol. 180, p. 107977, 2019.

[101] W. Gebarowski and S. Pietrzyk, "Influence of the cathodic pulse on the formation and morphology of oxide coatings on aluminium produced by plasma electrolytic oxidation/wpływ impulsu katodowego na tworzenie i morfologie warstw tlenkowych na aluminium otrzymywanych na drodze plazmowego utleniania elektrolitycznego," *Archives of metallurgy and materials*, vol. 58, no. 1, pp. 241–245, 2013.

[102] M. P. Kamil, M. Kaseem, and Y. G. Ko, "Soft plasma electrolysis with complex ions for optimizing electrochemical performance," *Scientific reports*, vol. 7, p. 44458, 2017.

[103] A. Hakimizad, K. Raeissi, M. Santamaria, and M. Asghari, "Effects of pulse current mode on plasma electrolytic oxidation of 7075 al in na2wo4 containing solution: From unipolar to soft-sparking regime," *Electrochimica Acta*, vol. 284, pp. 618–629, 2018.

[104] A. Melhem, G. Henrion, T. Czerwiec, J. Briançon, T. Duchanoy, F. Brochard, and T. Belmonte, "Changes induced by process parameters in oxide layers grown by the peo process on al alloys," *Surface and Coatings Technology*, vol. 205, pp. S133–S136, 2011.

[105] F. Jaspard-Mécuson, T. Czerwiec, G. Henrion, T. Belmonte, L. Dujardin, A. Viola, and J. Beauvir, "Tailored aluminium oxide layers by bipolar current adjustment in the plasma electrolytic oxidation (peo) process," *Surface and Coatings Technology*, vol. 201, no. 21, pp. 8677–8682, 2007.

[106] F. Tjiang, L.-W. Ye, Y.-J. Huang, C.-C. Chou, and D.-S. Tsai, "Effect of processing parameters on soft regime behavior of plasma electrolytic oxidation of magnesium," *Ceramics International*, vol. 43, pp. S567–S572, 2017.

[107] D.-S. Tsai and C.-C. Chou, "Review of the soft sparking issues in plasma electrolytic oxidation," *Metals*, vol. 8, no. 2, p. 105, 2018.

[108] E. Matykina, R. Arrabal, A. Mohamed, P. Skeldon, and G. Thompson, "Plasma electrolytic oxidation of pre-anodized aluminium," *Corrosion Science*, vol. 51, no. 12, pp. 2897–2905, 2009.

[109] E. Matykina, R. Arrabal, D. Scurr, A. Baron, P. Skeldon, and G. Thompson, "Investigation of the mechanism of plasma electrolytic oxidation of aluminium using 18o tracer," *Corrosion science*, vol. 52, no. 3, pp. 1070–1076, 2010.

[110] E. Matykina, R. Arrabal, A. Pardo, M. Mohedano, B. Mingo, I. Rodríguez, and J. González, "Energy-efficient peo process of aluminium alloys," *Materials Letters*, vol. 127, pp. 13–16, 2014.

[111] M. Mohedano, E. Matykina, R. Arrabal, B. Mingo, and M. L. Zheludkevich, "Peo of rheocast a356 al alloy: energy efficiency and corrosion properties," *Surface and Interface Analysis*, vol. 48, no. 8, pp. 953–959, 2016.

[112] E. Matykina, R. Arrabal, M. Mohedano, B. Mingo, J. Gonzalez, A. Pardo, and M. Merino, "Recent advances in energy efficient peo processing of aluminium alloys," *Transactions of Nonferrous Metals Society of China*, vol. 27, no. 7, pp. 1439–1454, 2017.

[113] X. M. Zhang, X. B. Tian, S. Q. Yang, C. Z. Gong, R. K. Y. Fu, and P. K. Chu, "Low energy-consumption plasma electrolytic oxidation based on grid cathode," *Review of Scientific Instruments*, vol. 81, no. 10, p. 103504, 2010.

[114] S. Troughton, A. Nominé, A. Nominé, G. Henrion, and T. Clyne, "Synchronised electrical monitoring and high speed video of bubble growth associated with individual discharges during plasma electrolytic oxidation," *Applied Surface Science*, vol. 359, pp. 405–411, 2015.

[115] M. Mohedano, R. Arrabal, B. Mingo, A. Pardo, and E. Matykina, "Role of particle type and concentration on characteristics of peo coatings on am50 magnesium alloy," *Surface and Coatings Technology*, vol. 334, pp. 328–335, 2018.

[116] S. Sarbishei, M. A. F. Sani, and M. R. Mohammadi, "Study plasma electrolytic oxidation process and characterization of coatings formed in an alumina nanoparticle suspension," *Vacuum*, vol. 108, pp. 12–19, 2014.

[117] M. Ghafaripoor, K. Raeissi, M. Santamaria, and A. Hakimizad, "The corrosion and tribocorrosion resistance of peo composite coatings containing α-al2o3 particles on 7075 al alloy," *Surface and Coatings Technology*, vol. 349, pp. 470–479, 2018.

[118] M. Mohedano, C. Blawert, and M. Zheludkevich, "Silicate-based plasma electrolytic oxidation (peo) coatings with incorporated ceo2 particles on am50 magnesium alloy," *Materials & Design*, vol. 86, pp. 735–744, 2015.

[119] H. Tang and F. Wang, "Effects of nano-fe2o3 powder on thermal emission property of microarc oxidation coating on titanium alloy," *Materials Science and Technology*, vol. 28, no. 12, pp. 1523–1526, 2012.

[120] V. Rudnev, M. Vasilyeva, P. Nedozorov, I. Korotenko, and A. Vaganov-Vil'kins, "Distribution of elements in the surface layer of plasma-electrolytic coatings formed on titanium in electrolytes with mno 2 particles," *Russian Journal of Physical Chemistry A*, vol. 85, no. 10, p. 1798, 2011.

[121] X. Lu, C. Blawert, Y. Huang, H. Ovri, M. L. Zheludkevich, and K. U. Kainer, "Plasma electrolytic oxidation coatings on mg alloy with addition of sio2 particles," *Electrochimica Acta*, vol. 187, pp. 20–33, 2016.

[122] S. Gnedenkov, S. Sinebryukhov, D. Mashtalyar, I. Imshinetskiy, A. Samokhin, and Y. V. Tsvetkov, "Fabrication of coatings on the surface of magnesium alloy by plasma electrolytic oxidation using zro2 and sio2 nanoparticles," *Journal of Nanomaterials*, vol. 2015, 2015.

[123] S. Stojadinović, N. Tadić, N. Radić, B. Grbić, and R. Vasilić, "Tio2/sno2 photocatalyst formed by plasma electrolytic oxidation," *Materials Letters*, vol. 196, pp. 292–295, 2017.

[124] X. Lu, M. Schieda, C. Blawert, K. U. Kainer, and M. L. Zheludkevich, "Formation of photocatalytic plasma electrolytic oxidation coatings on magnesium alloy by incorporation of tio2 particles," *Surface and Coatings Technology*, vol. 307, pp. 287–291, 2016.

[125] E. Matykina, R. Arrabal, F. Monfort, P. Skeldon, and G. Thompson, "Incorporation of zirconia into coatings formed by dc plasma electrolytic oxidation of aluminium in nanoparticle suspensions," *Applied Surface Science*, vol. 255, no. 5, pp. 2830–2839, 2008.

[126] J. J. Morgan and W. Stumm, "Colloid-chemical properties of manganese dioxide," *Journal of Colloid Science*, vol. 19, no. 4, pp. 347–359, 1964.

[127] P. Zhang, Z. Zhang, and W. Li, "Antibacterial coating incorporating silver nanoparticles by microarc oxidation and ion implantation," *Journal of Nanomaterials*, vol. 2013, 2013.

[128] L. Pezzato, P. Cerchier, K. Brunelli, A. Bartolozzi, R. Bertani, and M. Dabalà, "Plasma electrolytic oxidation coatings with fungicidal properties," *Surface Engineering*, vol. 35, no. 4, pp. 325–333, 2019.

[129] P. Cerchier, L. Pezzato, K. Brunelli, P. Dolcet, A. Bartolozzi, R. Bertani, and M. Dabalà, "Antibacterial effect of peo coating with silver on aa7075," *Materials Science and Engineering: C*, vol. 75, pp. 554–564, 2017.

[130] M. Rizwan, R. Alias, U. Z. Zaidi, R. Mahmoodian, and M. Hamdi, "Surface modification of valve metals using plasma electrolytic oxidation for antibacterial applications: A review," *Journal of Biomedical Materials Research Part A*, vol. 106, no. 2, pp. 590–605, 2018.

[131] A. Lugovskoy and S. Lugovskoy, "Production of hydroxyapatite layers on the plasma electrolytically oxidized surface of titanium alloys," *Materials Science and Engineering: C*, vol. 43, pp. 527–532, 2014.

[132] L.-H. Li, H.-W. Kim, S.-H. Lee, Y.-M. Kong, and H.-E. Kim, "Biocompatibility of titanium implants modified by microarc oxidation and hydroxyapatite coating," *Journal of Biomedical Materials Research Part A: An Official Journal of The Society for Biomaterials, The Japanese Society for Biomaterials, and The Australian Society for Biomaterials and the Korean Society for Biomaterials*, vol. 73, no. 1, pp. 48–54, 2005.

[133] W. K. Yeung, G. C. Reilly, A. Matthews, and A. Yerokhin, "In vitro biological response of plasma electrolytically oxidized and plasma-sprayed hydroxyapatite coatings on ti–6al–4v alloy," *Journal of Biomedical Materials Research Part B: Applied Biomaterials*, vol. 101, no. 6, pp. 939–949, 2013.

[134] D. Sreekanth, N. Rameshbabu, and K. Venkateswarlu, "Effect of various additives on morphology and corrosion behavior of ceramic coatings developed on az31 magnesium alloy by plasma electrolytic oxidation," *Ceramics International*, vol. 38, no. 6, pp. 4607–4615, 2012.

[135] M. Montazeri, C. Dehghanian, M. Shokouhfar, and A. Baradaran, "Investigation of the voltage and time effects on the formation of hydroxyapatite-containing titania prepared by plasma electrolytic oxidation on ti–6al–4v alloy and its corrosion behavior," *Applied Surface Science*, vol. 257, no. 16, pp. 7268–7275, 2011.

[136] J. Guo, L. Wang, S. Wang, J. Liang, Q. Xue, and F. Yan, "Preparation and performance of a novel multifunctional plasma electrolytic oxidation composite coating formed on magnesium alloy," *Journal of materials science*, vol. 44, no. 8, pp. 1998–2006, 2009.

[137] J. Zhao, X. Xie, and C. Zhang, "Effect of the graphene oxide additive on the corrosion resistance of the plasma electrolytic oxidation coating of the az31 magnesium alloy," *Corrosion Science*, vol. 114, pp. 146–155, 2017.

[138] L. Tonelli, L. Pezzato, P. Dolcet, M. Dabalà, and C. Martini, "Effects of graphite nanoparticle additions on dry sliding behaviour of plasma-electrolytic-oxidation-treated ev31a magnesium alloy against steel in air," *Wear*, vol. 404, pp. 122–132, 2018.

[139] B. Necula, L. Fratila-Apachitei, A. Berkani, I. Apachitei, and J. Duszczyk, "Enrichment of anodic mgo layers with ag nanoparticles for biomedical applications," *Journal of materials science. Materials in medicine*, vol. 20, pp. 339–45, 10 2008.

[140] D. Hanaor, M. Michelazzi, P. Veronesi, C. Leonelli, M. Romagnoli, and C. Sorrell, "Anodic aqueous electrophoretic deposition of titanium dioxide using carboxylic acids as dispersing agents," *Journal of the European Ceramic Society*, vol. 31, no. 6, pp. 1041–1047, 2011.

[141] D. Hanaor, M. Michelazzi, C. Leonelli, and C. C. Sorrell, "The effects of carboxylic acids on the aqueous dispersion and electrophoretic deposition of zro2," *Journal of the European Ceramic Society*, vol. 32, no. 1, pp. 235–244, 2012.

[142] K. Lee, B. Lee, S. Yoon, E. Lee, B. Yoo, and D. Shin, "Evaluation of plasma temperature during plasma oxidation processing of az91 mg alloy through analysis of the melting behavior of incorporated particles," *Electrochimica Acta*, vol. 67, p. 6–11, 04 2012.

[143] X. Li and B. L. Luan, "Discovery of al2o3 particles incorporation mechanism in plasma electrolytic oxidation of am60b magnesium alloy," *Materials Letters*, vol. 86, pp. 88–91, 2012.

[144] Y. Wang, D. Wei, J. Yu, and S. Di, "Effects of al2o3 nano-additive on performance of micro-arc oxidation coatings formed on az91d mg alloy," *Journal of Materials Science & Technology*, vol. 30, no. 10, pp. 984–990, 2014.

[145] T. S. Lim, H. S. Ryu, and S.-H. Hong, "Electrochemical corrosion properties of ceo2-containing coatings on az31 magnesium alloys prepared by plasma electrolytic oxidation," *Corrosion Science*, vol. 62, pp. 104–111, 2012.

[146] M. Shokouhfar and S. Allahkaram, "Formation mechanism and surface characterization of ceramic composite coatings on pure titanium prepared by micro-arc oxidation in electrolytes containing nanoparticles," *Surface and Coatings Technology*, vol. 291, pp. 396–405, 2016.

[147] L. Weiping, Z. Liqun, and L. Yihong, "Electrochemical oxidation characteristic of az91d magnesium alloy under the action of silica sol," *Surface and Coatings Technology*, vol. 201, no. 3-4, pp. 1085–1092, 2006.

[148] M. Aliofkhazraei, A. S. Rouhaghdam, and T. Shahrabi, "Abrasive wear behaviour of si3n4/tio2 nanocomposite coatings fabricated by plasma electrolytic oxidation," *Surface and Coatings Technology*, vol. 205, pp. S41–S46, 2010.

[149] K. R. Shin, Y. S. Kim, G. W. Kim, H. W. Yang, Y. G. Ko, and D. H. Shin, "Effects of concentration of ag nanoparticles on surface structure and in vitro biological responses of oxide layer on pure titanium via plasma electrolytic oxidation," *Applied Surface Science*, vol. 347, pp. 574–582, 2015.

[150] H.-x. Li, R.-g. Song, and Z.-g. Ji, "Effects of nano-additive tio2 on performance of micro-arc oxidation coatings formed on 6063 aluminum alloy," *Transactions of Nonferrous Metals Society of China*, vol. 23, no. 2, pp. 406–411, 2013.

[151] M. Mu, J. Liang, X. Zhou, and Q. Xiao, "One-step preparation of tio2/mos2 composite coating on ti6al4v alloy by plasma electrolytic oxidation and its tribological properties," *Surface and Coatings Technology*, vol. 214, pp. 124–130, 2013.

[152] X. Lu, C. Blawert, M. L. Zheludkevich, and K. U. Kainer, "Insights into plasma electrolytic oxidation treatment with particle addition," *Corrosion Science*, vol. 101, pp. 201–207, 2015.

[153] K. R. Shin, Y. G. Ko, and D. H. Shin, "Surface characteristics of zro2-containing oxide layer in titanium by plasma electrolytic oxidation in k4p2o7 electrolyte," *Journal of alloys and compounds*, vol. 536, pp. S226–S230, 2012.

[154] C.-Y. Liu, D.-S. Tsai, J.-M. Wang, J. T. Tsai, and C.-C. Chou, "Particle size influences on the coating microstructure through green chromia inclusion in plasma electrolytic oxidation," *ACS applied materials & interfaces*, vol. 9, no. 26, pp. 21864–21871, 2017.

[155] E. Erfanifar, M. Aliofkhazraei, H. F. Nabavi, and A. S. Rouhaghdam, "Growth kinetics and morphology of microarc oxidation coating on titanium," *Surface and Coatings Technology*, vol. 315, pp. 567–576, 2017.

[156] S. Gowtham, S. Hariprasad, T. Arunnellaiappan, and N. Rameshbabu, "An investigation on zro2 nano-particle incorporation, surface properties and electrochemical corrosion behaviour of peo coating formed on cp-ti," *Surface and Coatings Technology*, vol. 313, pp. 263–273, 2017.

[157] D. Sreekanth and N. Rameshbabu, "Development and characterization of mgo/hydroxyapatite composite coating on az31 magnesium alloy by plasma electrolytic oxidation coupled with electrophoretic deposition," *Materials Letters*, vol. 68, pp. 439–442, 2012.

[158] Y. Xiong, C. Lu, C. Wang, and R. Song, "The n-mao/epd bio-ceramic composite coating fabricated on zk60 magnesium alloy using combined micro-arc oxidation with electrophoretic deposition," *Applied surface science*, vol. 322, pp. 230–235, 2014.

[159] A. Kazek-Kęsik, M. Krok-Borkowicz, G. Dercz, A. Donesz-Sikorska, E. Pamuła, and W. Simka, "Multilayer coatings formed on titanium alloy surfaces by plasma electrolytic oxidation-electrophoretic deposition methods," *Electrochimica Acta*, vol. 204, pp. 294–306, 2016.

[160] S. Arun, S. Hariprasad, A. Saikiran, B. Ravisankar, E. Parfenov, V. Mukaeva, and N. Rameshbabu, "The effect of graphite particle size on the corrosion and wear behaviour of the peo-epd coating fabricated on commercially pure zirconium," *Surface and Coatings Technology*, vol. 363, pp. 301–313, 2019.

[161] G. B. Darband, M. Aliofkhazraei, P. Hamghalam, and N. Valizade, "Plasma electrolytic oxidation of magnesium and its alloys: Mechanism, properties and applications," *Journal of Magnesium and Alloys*, vol. 5, no. 1, pp. 74 – 132, 2017.

[162] B. Guan, R. Zhan, H. Lin, and Z. Huang, "Review of the state-of-the-art of exhaust particulate filter technology in internal combustion engines," *Journal of environmental management*, vol. 154, pp. 225–258, 2015.

[163] E. B. Watson and J. D. Price, "Kinetics of the reaction mgo+ al2o3→mgal2o4 and al-mg interdiffusion in spinel at 1200 to 2000° c and 1.0 to 4.0 gpa," *Geochimica et Cosmochimica Acta*, vol. 66, no. 12, pp. 2123–2138, 2002.

[164] J. C. Baygents and D. Saville, "Electrophoresis of small particles and fluid globules in weak electrolytes," *Journal of colloid and interface science*, vol. 146, no. 1, pp. 9–37, 1991.

[165] S. L. Petersen and N. E. Ballou, "Separation of micrometer-size oxide particles by capillary zone electrophoresis," *Journal of Chromatography A*, vol. 834, no. 1-2, pp. 445–452, 1999.

[166] K. M. Lee, B. U. Lee, S. I. Yoon, E. S. Lee, B. Yoo, and D. H. Shin, "Evaluation of plasma temperature during plasma oxidation processing of az91 mg alloy through analysis of the melting behavior of incorporated particles," *Electrochimica Acta*, vol. 67, pp. 6–11, 2012.

[167] M. Shokouhfar and S. Allahkaram, "Effect of incorporation of nanoparticles with different composition on wear and corrosion behavior of ceramic coatings developed on pure titanium by micro arc oxidation," *Surface and Coatings Technology*, vol. 309, pp. 767–778, 2017.

[168] J. Yahalom and J. Zahavi, "Experimental evaluation of some electrolytic breakdown hypotheses," *Electrochimica Acta*, vol. 16, no. 5, pp. 603–607, 1971.

[169] S. Ikonopisov, A. Girginov, and M. Machkova, "Electrical breaking down of barrier anodic films during their formation," *Electrochimica Acta*, vol. 24, no. 4, pp. 451–456, 1979.

[170] K. Venkateswarlu, N. Rameshbabu, D. Sreekanth, M. Sandhyarani, A. Bose, V. Muthupandi, and S. Subramanian, "Role of electrolyte chemistry on electronic and in vitro electrochemical properties of micro-arc oxidized titania films on cp ti," *Electrochimica Acta*, vol. 105, pp. 468–480, 2013.

[171] F. Simchen, M. Sieber, and T. Lampke, "Electrolyte influence on ignition of plasma electrolytic oxidation processes on light metals," *Surface and Coatings Technology*, vol. 315, pp. 205–213, 2017.

[172] M. O'Hara, S. Troughton, R. Francis, and T. Clyne, "The incorporation of particles suspended in the electrolyte into plasma electrolytic oxidation coatings on ti and al substrates," *Surface and Coatings Technology*, p. 125354, 2020.